DIAGNOSTIC BIOSENSORS FOR DETECTION OF BLOOD-DERIVED BIOMARKERS

by

Tiffany-Heather Ulep

A Dissertation Submitted to the Faculty of the

DEPARTMENT OF BIOMEDICAL ENGINEERING

In Partial Fulfillment of the Requirements

For the Degree of

DOCTOR OF PHILOSOPHY

In the Graduate College

THE UNIVERSITY OF ARIZONA

2019

As members of the Dissertation Committee, we certify that we have read the dissertation prepared by Tiffany-Heather Ulep, titled **Diagnostic Biosensors for Detection of Blood-Derived Biomarkers** and recommend that it be accepted as fulfilling the dissertation requirement for the Degree of Doctor of Philosophy.

Jeong-Yeol Yoon — Date: 12/5/19

David W. Galbraith — Date: 12/5/19

Frederic Zenhausern — Date: 12/5/19

Minkyu Kim — Date: 12-5-19

Final approval and acceptance of this dissertation is contingent upon the candidate's submission of the final copies of the dissertation to the Graduate College.

I hereby certify that I have read this dissertation prepared under my direction and recommend that it be accepted as fulfilling the dissertation requirement.

Jeong-Yeol Yoon — Date: 12/19/19
Dissertation Committee Chair
Department of Biomedical Engineering

ACKNOWLEDGEMENTS

I would like to give a special thanks to Dr. Jeong-Yeol Yoon, my graduate mentor and principal investigator, for the support and guidance throughout my graduate career. Every advice that Dr. Yoon has given me has brought me to where I am today and I am not not loving the view.

I would also like to express my deep gratitude to my remaining dissertation committee for their time and contribution: Dr. David Galbraith, Dr. Frederic Zenhausern, and Dr. Minkyu Kim.

I am appreciative to previous graduate students that have been my colleagues, mentors, and all-around life time friends Dr. Robin Sweeney, Dr. Soohee Cho, Dr. Katie Klug, Dr. Soo Chung, and Dr. Ariana Nicolini. I would also like to thank current and past Biosensor Lab members: Kattika Kaarj, Matthew Bills, Alexander S. Day, Kenny Schackart III, Lane Breshears, Dr. Sangsik Kim, Eliza Budiman, Ryan Zenhausern, Katie Sosnowski, Alana Gonzales, Lexie Shumaker, Samuel Kim, and Babak Safavinia — without whom the laboratory and office would not have become my chaotic, fun, and productive second home in Tucson.

I express my gratitude to fellow graduate students that have faithfully alongside me, experienced the wins and losses of collegial intramural sports and life's obstacles as a graduate student — David S. Knoff, Loi Do, Marissa Lopez-Pier, Vic Keschrumrus, Chris Camp, Chet Preston, Jokubas Ausra, Fred Schroeder, and Peter Dawson.

I am deeply appreciative to the people that have given me a place to unwind and let loose throughout my time here in Tucson — roommates and friends, Jessica Ditmore and Jeri Goodin.

I would like to specifically thank Christopher Mead and family for taking me in and providing me a home away from away.

I would like to acknowledge the National Institute of Health (NIH grant T32HL007955) and the National Science Foundation East Asia Pacific Summer Institute Korea (NSF EAPSI fellowship No. 1714046) as my funding sources that have supported me throughout my graduate career.

I am forever appreciative for the consistent love, support, and inspiration from my parents and siblings who have encouraged me to pursue everything and anything that I desire every step of the way. I am deeply thankful for my best friends — Crystal Wang, Kadi Lee, Alyssa Garcia, and Quirena Natividad for always being there to cheer me on, be my outlet, and to experience with me life's ups and downs in its most raw form. Lastly, I am grateful to have Newton the Labradoodle for being my one constant that has made my world brighter and filled with unconditional love.

DEDICATION

For my dad, Jesus P. Ulep — the man who reminds and inspires me to always do better.

TABLE OF CONTENTS

LIST OF TABLES

LIST OF FIGURES

ABSTRACT

Standard diagnostic tools used from patient samples, specifically from blood draws, require specialized equipment, personnel, and facilities. Conventional techniques can often be very laborious and time consuming due to required sample preparation. The evident delay from sample collection to a patient's result immensely impacts their outcome. The aims of this research are to design diagnostic biosensors that decrease time-to-results, minimize reagent and sample handling, and incorporate automated simple optical transduction and user interfaces for the detection of blood-derived biomarkers. Specifically, four biosensing detection mechanisms performed on 3 different point-of-care platforms will be discussed.

First is a static loop-mediated isothermal amplification (LAMP) of nucleic acid aqueous droplet on a silicone chip platform immersed in mineral oil. The target-of-interest is a nucleic acid sequence as a biomarker for antibiotic resistant bacteria. The biosensing technique used related changes in interfacial tension (IFT) at the water-oil interface by measuring the change in contact angle (geometrical-effects) over time. Initially the system was characterized as a linear response in relation to concentration of bacteria in a buffer system down to the limit of detection (LOD) of 100 CFU per μL. Subsequently, with the addition of bacterial infected blood sample models, the system became a binary assay (i.e. yes or no) as low as 10 CFU per μL within 10 min of reaction.

Secondly, a two-layered, paper microfluidic chip was utilized to quantify cancer cells from a buffy coat sample matrix by two detection mechanisms: 1) on-chip particle enumeration via smartphone microscope and 2) capillary flow dynamics via smartphone video processing. The assay resulted in a LOD as low as 1 cell per μL for the on-chip imaging aspect of platform and 0.1 cell per μL for the capillary flow analysis within 13 to 22s post application of blood sample.

Lastly, the same concepts previously described in the first platform utilizes changes in IFT due to amplicon presence in an aqueous solution immersed in mineral oil. An emulsion LAMP platform was investigated to determine the relation between angle-dependent light scatter intensity (based off Mie scatter theory) and nucleic acid amplification progression. The phenomenon attributing to changes in light scatter intensities is due to the interfacial changes occurring in the emulsion droplets, where amplicon amount increases the IFT decreases, resulting in smaller diameter emulsions. Changes in light scatter intensity within 3 min of the reaction shows statistical difference in comparison to no target control (NTC) for 10^3 CFU per μL of bacteria dosed into aqueous sample. These four detection mechanisms and three platforms offer but a few alternatives as biosensing methods for blood-derived diagnostic biosensors.

INTRODUCTION[1]

Challenges in developing rapid diagnostic tools for blood-derived biomarkers

Molecular analytics of patient samples such as tissue biopsies, blood, urine, and saliva is a routine process throughout the healthcare field, in which valuable information, whether it be for preventative monitoring purposes, diagnostic reasons, or prognostic decisions, is revealed. The assays which are performed on these samples require costly equipment, expensive reagents, and trained personnel, that are usually conducted off-site in a specialized facility. Therefore, patient results, or time-to-results, are inevitably delayed due to the need to transport samples to controlled environments[1].

Specifically, for bloodstream infection identification with antibiotic resistance/susceptibility characteristics, hematology analysis, and immune-based assays, there have been numerous efforts in the scientific community to tackle the problem of prolonged time-to-results. Such efforts have been addressed by the implementation of large systems that automate the process from sample preparation to specific-agent testing to reporting[2,3]. These systems have increased laboratory productivity, reproducibility, and diversity of tests, with reduced specimen turnaround time. However, these systems are large scale and high throughput, making them impractical for clinical settings, resource-limited areas, and field-use.

Point-of-care and lab-on-a-chip

Point-of-care (POC) diagnostics are rapid, low-cost, mobile tests that can be conducted in resource-limited environments by minimally trained personnel. Conducting tests on site allows for faster time-to-results, which in turn improves opportunities for proper and adequate patient treatment [4,5]. The incorporation of microfluidics with POC tests add complexity and versatility

[1] Adapted from Ulep and Yoon. Challenges in paper-based fluorogenic optical sensing with smartphones. Nano Convergence. (2018) 5:14. – Published by SpringerOpen

to the assays due to controlled flow in discrete spaces, reduction in sample volume, minimized handling of reagents, and ability to run parallel comparison analyses[6].

Lab-on-a-chip (LOC), is a subsection of POC that was inherently developed as a byproduct of biomedical engineers creating innovative and novel methods and technologies in which complex assays that require multiple reagents and steps throughout the process are miniaturized and precisely controlled in an all-in-once "chip" format[7]. Polydimethylsiloxane (PDMS) polymers are commonly used in fabrication of microfluidic LOC POC platforms. PDMS provides an optically transparent (230 – 1100 nm), flexible, nontoxic, and low-cost material. However, when untreated, the PDMS surface is relatively hydrophobic, which can be problematic in controlling flow especially under low pressure conditions. Also, irreversible protein adsorption to PDMS surfaces can eventually lead to a nonfunctional device. Although there have been many surface modification techniques developed, induced hydrophilic states are only temporary. PDMS inherent hydrophobicity will return after a period of time[8,9]. Furthermore, when developing unique infrastructures such as on-chip pumps and valves, PDMS lithography fabrication techniques require a clean room access, which in turn can become complex and expensive for prototyping.

Paper microfluidics

Alternatively, paper can be used as a microfluidic platform. It is inexpensive, easy to chemically modify (i.e. nitrogen functionalized cellulose is commonly used for biological samples), and easy to fabricate, store, and transport[10]. Additionally, due to the fibrous structure of paper, which results in capillary flow and wicking effects of reagents, obviates the need for external pumping, unlike silicone-based LOC. A widely known and highly used paper-based lateral flow assay (LFA) example is the colorimetric pregnancy test strip. The basic mechanism

utilizes a sandwich immunoassay. Immobilized antibodies on a paper substrate bind with target antigens if present in the applied sample. Subsequently, secondary antibodies conjugated to gold nanoparticles act as the reporter through binding to the antibodies immobilized on the paper with the captured antigens. The resulting positive diagnostic detection is the appearance of an aggregation-induced pink color [11]. The colorimetric indicator is due to a spatially dependent optical property of gold nanoparticles, known as the surface plasmon resonance band [12]. However, colorimetric LFAs are binary, i.e. yes-or-no assays, thus difficult to quantify in a reproducible manner. In addition, they show little potential for multiplexing capabilities since they can detect only one assay per strip. Also, commercially available LFAs require a high concentration of targets of interest in order to obtain a reliable signal that may not be within the normal or hyperactive physiologically relevant levels [11]. As an example, commercially available LFAs for detection of thyroid stimulating hormone (TSH) have a limit of detection of >5 mIU/ L, which fails to detect the normal and low concentrations of TSH (i.e. hyperthyroidism) in human blood serum [13]. Similarly, commercially available nitrite LFAs for recognizing *Escherichia coli* from urine (for detecting urinary tract infection), as well as *Neisseria gonorrhoeae*, the most common cause of sexually transmitted disease (STD) infection of the urogenital tract, havea limit of detection of 10^6 CFU/mL [14]. Urinary tract infections can have bacteria concentrations as low as 10^2-10^3 CFU/mL in adult patients [15] and even less in children [16]. In a thorough analysis of commercial assays for detection of *Cryptosporidium* in fecal samples, the ImmunoCard STAT! LFA platform failed to detect all 12 samples with <175 organisms per 10 μL sample and had problems with interpretation due to low band intensity [17].

Biosensing techniques used in blood diagnostics

Fluorescence

Blood is a complex mixture of cells, proteins, and fluids; therefore detecting a target-of-interest with a differential signal from background noise can become a challenge when developing diagnostic assays. Fluorescence can be a powerful tool in producing distinguishable signals due to its intrinsic mechanism which absorbs the excitation light at characteristic wavelengths unique to each fluorescent compound and then emits fluorescence having a complementary emission wavelength profile (see Figure 1). The use of fluorophores to label targets-of-interest for diagnostic purposes are commonly used to identify nucleic acids, cells, and analytes.

Fluorophores can be a dye that fluoresces only when bound to the target-of-interest. An example of a fluorescent dye that is commonly used to identify whole cell DNA is 4'-6-diamidino-2-phenylindole (DAPI). Its excitation wavelength maximum is 358 nm, and corresponding emission maximum of 461 nm. DAPI when bound to the AT (adenosine-tyrosine) regions of double-stranded DNA (dsDNA) increases its fluorescent intensity by 20-fold. Fluorescent labeling of a cell nuclei can give information about apoptosis, morphology, size, cell count, and cell cycle status, and can also be used for sorting of single cells and nuclei[18]. Another example of a well-known DNA fluorescent stain is SYBR® Green, a dsDNA probe that intercalates between DNA base pairs. SYBR® Green is widely used to monitor the nucleic acid amplification of a target-gene-of interest in a real-time manner[19].

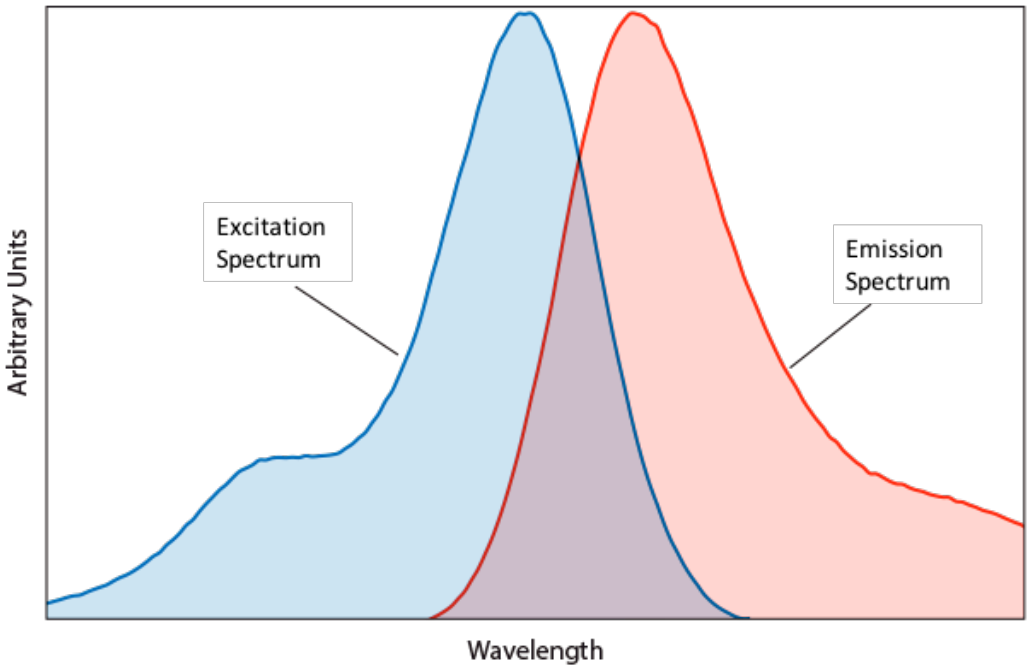

Figure 1. Example of excitation and emission spectrum of a generic fluorescent dye overlaid and showing two distinctive and unique peaks[20]

For more specific fluorescent labeling, fluorophores can be conjugated to a bio-recognition element such as an antibody or oligonucleotide that has a high affinity to the target-of-interest. Fluorescent *in situ* hybridization (FISH) is a label and detection mechanism that is routinely used in diagnostics using patient blood samples. The biorecognition element in the FISH biosensing technique is a fluorescently labeled oligonucleotide whose sequence is complementary to the target single-stranded DNA sequence[21]. Specifically, in blood borne pathogen detection, FISH technologies are used to rapidly detect and identify positive bacteria blood cultures. In real-time the fluorescent intensity is monitored as a direct result of an increasing amount of target gene in the growing bacteria blood culture[22]. Antibody-conjugated fluorophores are widely used labeling tools for diagnostics. Specifically, cell labeling to specific proteins such as phalloidin or vinculin allows users to visualize the F-actin filaments and

cytoskeleton to determine cell type (normal versus cancerous) and induced response morphology [23] (see Figure 2).

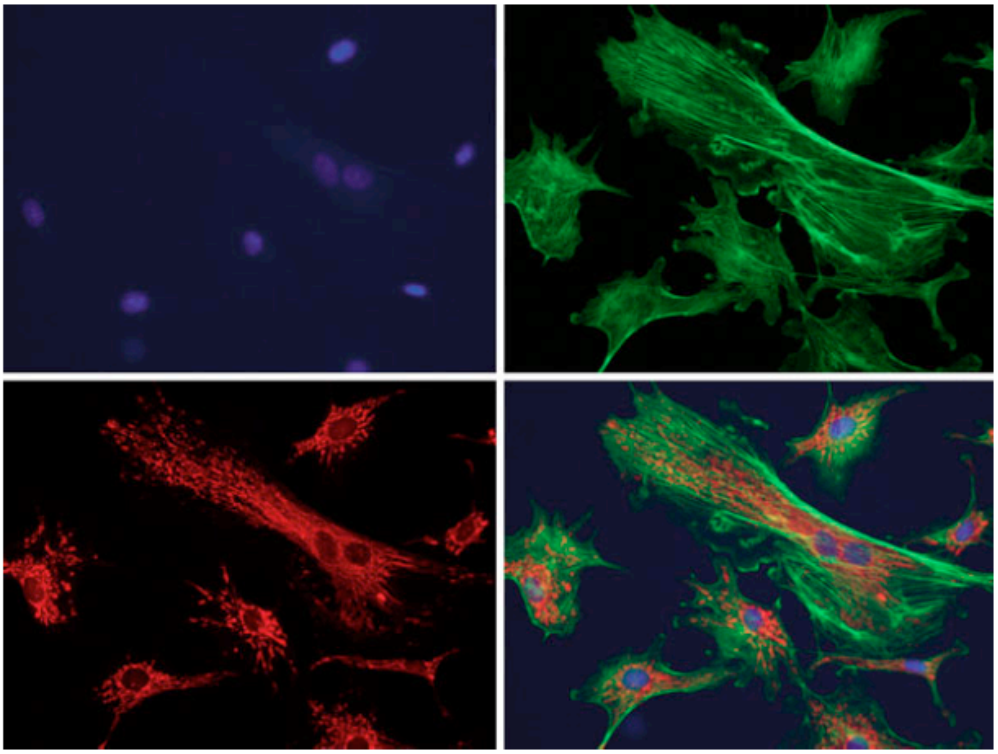

Figure 2. Fluorescence microscope images of cells stained with top left: DAPI intercalating dye, top right: Fluorescein isothiocyanate (FITC) conjugated to anti-vinculin, bottom left: Tetramethylrhodamine isothiocyanate (TRITC) conjugated to anti-phalloidin, bottom right: overlaid red, green, blue channel images into a single combined cell image[12].

Advantages of fluorophores are that they are widely used synthetic molecules rendering them easily accessible and relatively inexpensive. Fluorophores are very commonly used in POC and LOC platforms to reduce the limit of detection (LOD) of the target-of-interest. However, traditional fluorophores are known to photobleach when exposed to excessive amounts of light, therefore storage, stability, and long-term use are limited in POC applications.

Nanotechnologies combined with fluorescence detection has demonstrated the lowering of limit of detection for devices down to the single cell or picogram protein molecule resolution [24–27]. Implementation of fluorescent nanotechnologies such as quantum dots [28–30]and nanoclusters[31,32] have several advantages over more traditional colorimetric sensors. Nanoscale sensor sizes and shapes can easily be tuned to respond to specific excitation wavelengths, by varying shape, size, and length. Nanostructures possess large surface areas for accommodating increased amount of bioreceptor immobilization, and this in turn results in increased sensitivity and much lower limit of detection. Nanoparticles are also highly stable and do not photobleach as easily in comparison to traditional fluorescent dyes [33,34]. The resulting fluorescence emission spectrum provides increased sensitivity, which in turn results in increased signal-to-noise ratios. Lastly, the materials used in these nanotechnologies, such as carbon [35,36] and gold [37,38] show superior biocompatibility in complex biological matrices. Fluorogenics in combination with paper-based microfluidic devices, reduces cost, simplifies manufacturability, and improves ease of disposability[39]. Therefore, fluorescent nanotechnologies on paper-based platforms have become an extremely attractive option in biological and chemical sensing [40].

Nucleic acid amplification

Nucleic acid amplification is another conventional detection modality commonly used for blood diagnostics. The Polymerase Chain Reaction (PCR) is a gold standard methodology that utilizes cyclic temperature shifts: 1) denaturation of dsDNA at 94-96°C, 2) annealing of primers at 50-65°C, and 3) extension of complementary sequence via a polymerase enzyme at 70-76°C (see Figure 3) to amplify targets. In turn, an exponential amount of colinear copies of the target dsDNA of interest are produced[41]. PCR usually requires the extraction of DNA from the

pathogen-of-interest, such as a virus, bacteria, or cell (i.e. cancerous, normal) via a lysing process. An important component required in a PCR reaction are two primers: a forward and a reverse primer, which are complementary short sequences that oppositely tag on both sets of dsDNA. Four types of deoxy ribonucleotide triphosphates (dNTPs): adenine (A), thymine (T), guanine (G), and cytosine (C), which are the monomers of nucleic acids are then added in a complementary manner via a polymerase[12].

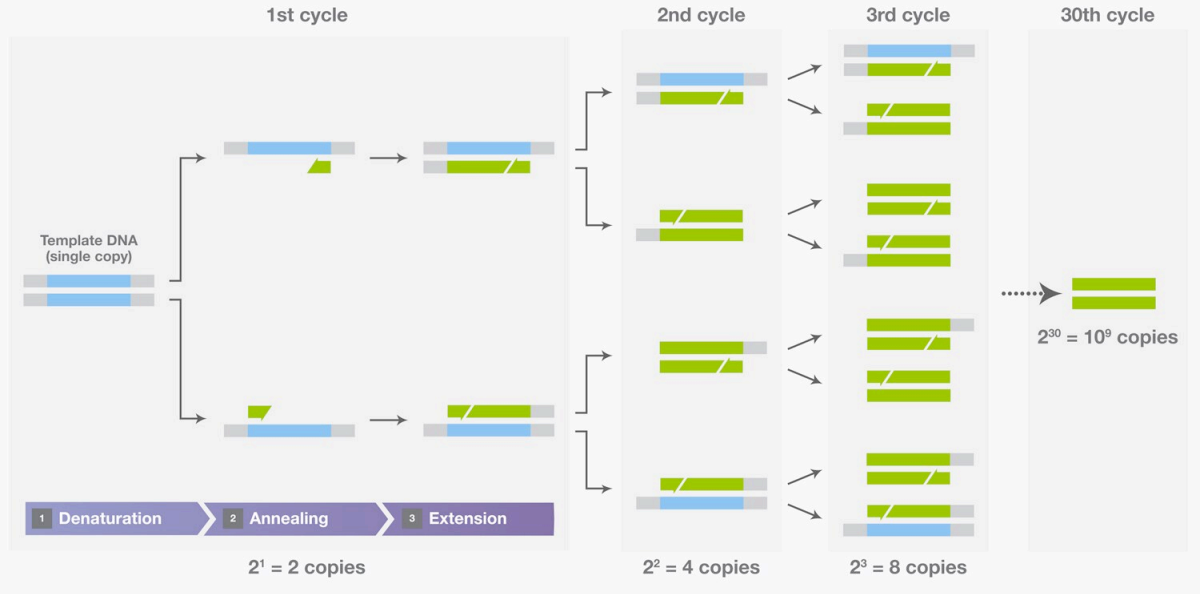

Figure 3. The three-step process of the polymerase chain reaction (PCR) — denaturing, annealing, and extension, which results in an exponential growth of linear target DNA as cycles are repeated.

End-point analysis of a nucleic acid amplification reaction to verify production of amplicons has traditionally been done using gel electrophoresis. Gel electrophoresis exploits the intrinsic negative charge of DNA and its molecular weight dependent diffusion through an agarose gel matrix. When a current is applied across a gel, DNA moves through the gel at rates

dependent to its fragment size due to its attraction to the positive pole. This process can be very time consuming and laborious, therefore real-time methodologies were developed to monitor the progression of nucleic acid amplification as the reaction occurs.

Quantitative PCR (qPCR) utilizes intercalating dyes such as ethidium bromide and SYBR® Green which have high affinity to nucleic acids by embedding between base pairs. As a result, fluorescence intensities can be monitored over time for various initial target concentration, resulting in standard curves that could be used to quantify unknown amounts of target sequence in samples. However, such intercalating dyes are non-specific in the sense that they will bind to any dsDNA. As a result, to address this problem complementary oligonucleotides to target sequences can be conjugated with a fluorophore to act as reporter. These hybridization probes allow for a cleaner fluorescent signals that are more specific and directly quantitative to the amount of target gene being amplified in real time[22].

Overall, PCR has been shown to be a powerful diagnostic tool that provides a gold standard technology for clinicians and researchers alike. However, in blood diagnostics the use of PCR has its limitations due to the presence of inhibitors such as proteins (proteins, immunoglobulins[42], small molecules[43], and excess non-targeted DNA/RNA. Pre-processing of patient drawn samples, via purification and extraction of the target genomes, increases the assay time and delays time-to-results. Therefore, there is a need to develop techniques in which blood samples can be directly placed into nucleic acid reactions without signals being compromised. LOC and POC technologies have incorporated PCR into their platforms as a means to address the complex reagent handling, cyclic heating temperatures, and the bulky equipment required to run the reaction that reduce the complications of traditional PCR methodologies. Complex microfluidic chips have been designed and developed to intricately control flow, filter, and amplify whole blood samples to detect genes of interest[44–46].

Isothermal nucleic acid amplification technologies have gained popular interest amongst POC and LOC scientist/engineers. Amplicons are exponentially produced at a constant temperature and fast reaction times (~20 min), therefore rendering them an attractive technology to field and clinical settings since specialized heating and cooling equipment is no longer required[47]. Specifically, loop-mediated isothermal amplification (LAMP) is one of many isothermal techniques that have been utilized and even translated into commercially available kits. LAMP reactions are comprised components similar to those of PCR reactions, but differ significantly due to the use of 4 to 6 primers. Such primers include a forward, reverse, FIP, BIP, LoopB, and LoopF that essentially induces the annealing and extension via cyclic displacement of a target gene without denaturation. As a result, LAMP amplicons are high molecular weight and are dumbbell or cauliflower shaped [48,49].

Real-time progression of LAMP platforms have been extensively demonstrated, utilizing several detection methods, such as electrochemical[50,51], fluorescent[52,53], colorimetric[54–56], and turbidimetric (due to magnesium pyrophosphate precipitation)[57,58] detection. However such sensing modalities can be susceptible to and therefore limited by changes in environmental conditions, such as inconsistent ambient lighting, and the need for external hardware (i.e. light sources, optical filters, and transducers). Alternative methods of measuring nucleic acid amplification can be conducted by measuring the interfacial tension changes of the aqueous nucleic acid amplification reaction. Harshman et al. (2015), utilized a moving droplet-on-a-thermocouple PCR (DOTS qPCR) device that monitored the geometrical difference of a PCR droplet that traveled through a temperature gradient mineral oil bath providing the cyclic temperatures required. Due to the increased production of PCR amplicons, the droplet size decreased due to decreased interfacial tension. The DOTS qPCR platform was able to reduce time-to-results immensely in comparison to conventional nucleic acid amplification techniques

and showed significant amplification in complex sample matrices due to passive adsorption of protein molecules at the water-oil interface, thus separating inhibitors from compromising the efficiency of the reaction (see Figure 4) [59].

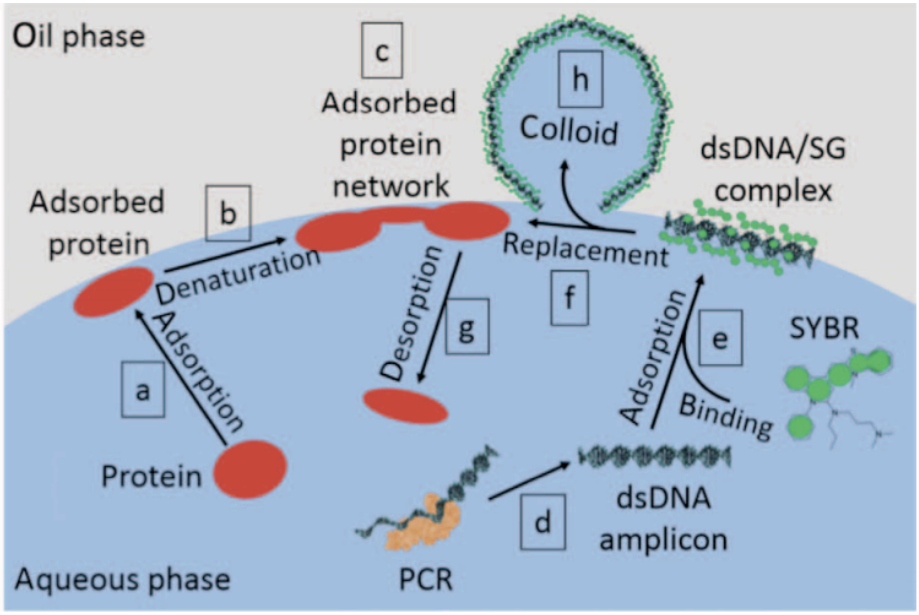

Figure 4. Schematic illustration of competitive adsorption a the water-oil interface followed in the order of 1) protein adsorption (competitive inhibitors to PCR reaction), 2) protein conformational change at the interface, 3) replacement of denatured proteins with newly produced amplicons at the water-oil interface, 4) intercalation of SYBR® Green to amplicons at interface, 5) destabilization of interface due to decreased interfacial tension, and lastly 5) colloidal breakaway from the main PCR droplet.

Smartphone sensing and interfacing for POC applications

Smartphone optical sensing, utilizing its flash as a light source, its cameras as an optical detector, and potentially its software application for data processing is a potentially advantageous approach for POC applications. As a result, an easy-to-use, point-of-care, yet extremely sensitive handheld platform can be imagined. Smartphone integration has already demonstrated numerous

advantages and opportunities in its use as a detector and a user interface platform for POC assays. Smartphones also allow for network connection and access, on-board processing, and applications in resource-limited settings [39,40,60–62].

As such, the number of publications in smartphone sensors have significantly increased over the past 5 years, as shown in Figure 5 (orange line). Expected next steps for smartphone sensing include its integration with paper-based platforms, its use in conjunction with fluorescent nanotechnologies, and combination of both, towards improving ease-of-use and sensitivity. However in 2017, for the first time, the total number of publications on the topic of smartphone sensing has started to decrease, potentially suggesting challenges in advanced smartphone sensing.

The number of publications demonstrating fluorescent nanotechnology with smartphone sensing also showed the similar trend – a slow increase followed by a decrease in 2017 (Figure 5; yellow line), suggesting complications and challenges in demonstrating fluorescent nanotechnology with smartphone sensing. The number of publications demonstrating all of the above – smartphone sensing of fluorescent nanotechnology on paper-based platform is significantly smaller than overall smartphone sensing (Figure 5; light green line), again demonstrating its complications, although this number has continued to increase over time.

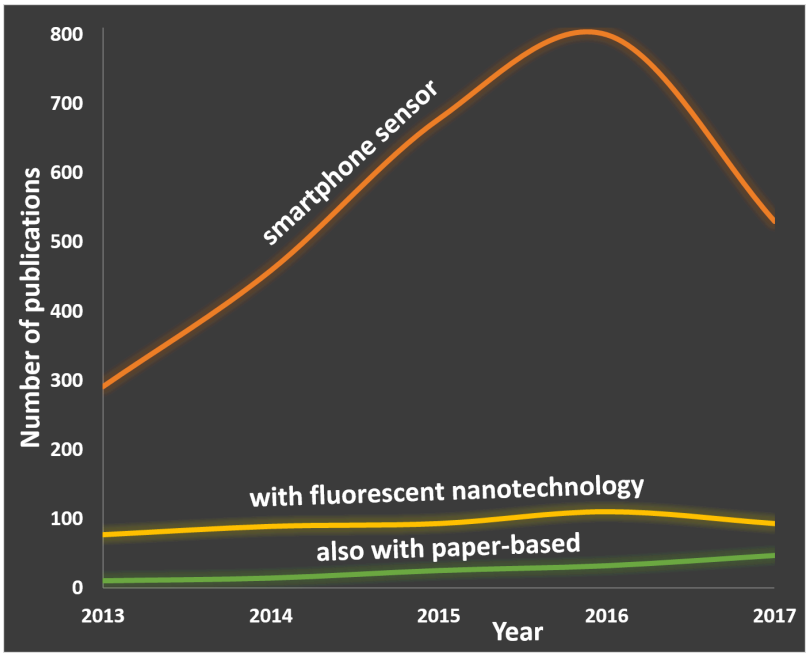

Figure 5. The number of research article publications on smartphone sensor (orange), those with fluorescent nanotechnology (yellow), and above two with paper-based fluorescent (light green) in the past 5 years. Clarivate Web of Science was used as the data source.

Although there have been many publications and reviews attesting to these outlined advantages for paper-based fluorescent platforms, there has been a dearth of discussion on the challenges, technical limitations, and alternative methods of its fluorescent optical detection, especially in conjunction with smartphone sensing.

Smartphone digital processing

Digital enhancement

These days, the complementary metal oxide semiconductor (CMOS) array is the most widespread image sensor for smartphones. It utilizes Bayer color filter arrays (CFAs) that collect red, green, and blue (RGB) values from a grid-like structure. The raw data pixel values are

processed through a demosaicing algorithm, which fills in missing RGB values through interpolation, resulting in an RGB image. Following the demosaic algorithm, a denoising algorithm is then applied [63,64]. Data image processing varies widely across smartphone models and brands, as do the physical properties of CMOS image sensors. Recently, Fontaine [65] released a well-organized and detailed publication outlining the different CMOS schematics between smartphone models and brands as well as the evolution of the technology over the years. Specific variations include the spatial resolution between metal aperture walls, the color filters used, and the optical stacking thickness.

In most paper-based point-of-care assays that utilize fluorescence, pixel intensities are extracted and converted into a concentration of a target of interest, i.e., molecules [66–68], proteins [69,70], whole organisms [71], or nucleic acids [72,73]. When trying to control and maintain constant lighting, white balance, focus, or exposure while running multiple assays, on-board default camera settings on smartphones can be problematic, as they are constantly trying to "optimize" white balance, focus, and exposures. Of particular concern is the ability of the camera to resolve very small points of interest, such as the test line on a LFA, or fluorophore-loaded areas on paper microfluidic devices [39].

To further refine the captured fluorescent images, it is also common to apply digital filters. Use of digital filters does not require physical adjustments to the overall optical setup. This in turn offers a low cost and simple method for correcting undesirable image flaws. In fluorescence imaging, excessive crosstalk, which is the inconsistent recognition from left to right views resulting in a blurry effect, is a typical correction to address [74,75].

There have also been numerous publications investigating better extraction and interpretation of measured RGB pixel values from the smartphone captured images on paper-based platforms. Different color spaces have been investigated to enhance paper-based pixel

intensities [62]. Shen *et al.* [76] describe color conversion analysis and quantification of colorimetric pH test strips, and developed a more sensitive and accurate method utilizing a 12 region reference chart to account for variability in lighting conditions. The group also alluded to its use in fluorescence paper microfluidic data, although it has not yet been demonstrated. Yetisen *et al.* [40] have devised an image processing algorithm that transforms RGB values into non-linear, linear, tristimulus, then into 2D CIE 1921 chromaticity space, which showed improvements in mitigating variability due to focus, angle, lighting, and sensor type. The applied algorithm was also demonstrated using two different cell phones, an iPhone 5 (8 MP camera) and a Samsung I5500 Galaxy 5 (2 MP camera), thereby demonstrating interphone adaptability. McCracken *et al.* [77] demonstrated the use of a triple-reference point normalization as well as fast-Fourier transform pre-processing using two different smartphone models (the iPhone 5S and the Nexus 5X). The image processing reduced spatial variability due to inconsistent paper surface, shadows, and uneven background reflectance for paper-based microfluidic assays using absorbance, quenching, and scattering measurements.

Ratiometric FRET

Fluorescence Resonance Energy Transfer (FRET) is the mechanism in which a fluorescent signal is produced due to a transfer of electrons from a donor fluorophore to an acceptor fluorophore that is within Angstrom proximal distances. As a result, two distinctive wavelength peaks are generated and can be measured in a ratiometric manner. In order for this to be efficiently monitored, peak excitation and emission wavelengths must be sufficiently separated, while having an overlap in donor emission and acceptor excitation spectra [78–80].

Ratiometric measurements are attractive due to their inherent ability to correct for environmental factors (such as varied lighting conditions and/or optical transparency of medium,

especially useful on paper-based platforms) and to self-calibrate [81,82]. Fluorescent dyes, although having been popularly used to demonstrate FRET-based ratiometric assays, are susceptible to photobleaching [83]. More recently, the use of quantum dots [82,84,85] and gold nanoclusters [31] have been better choices for FRET-based sensors due to their inherent photostability and superior signal-to-noise performance [86].

With regards to its applications in smartphone-based paper platforms, ratiometric fluorescent intensities can be easily monitored by simple splitting of red, green, and blue channels in a captured image. Wang et al. [68] measured 803 nm fluorescent intensity in relation to blue emission of upconversion nanoparticles ($NaYF_4$:Yb and Tm@$NaYF_4$) on paper to detect organophosphate nerve agents. As depicted in Figure 2, Noor and Krull [81] demonstrated the use of a smartphone where associated green and red pixel values were measured to monitor a nucleic acid hybridization assay. An inverse relationship was shown with correlated FRET-based transduction of donor green-emitting quantum dots and acceptor Cy3 fluorescent dye acceptor through a R/G (red over green) ratio. Yu et al. [87] prepared a ratiometric fluorescent test paper for visualization and quantification of fluoride ions in environmental waters with the use of CdTe quantum dots. As shown in Figure 6, red and blue fluorescence intensities were inversely related with the addition of fluoride ions.

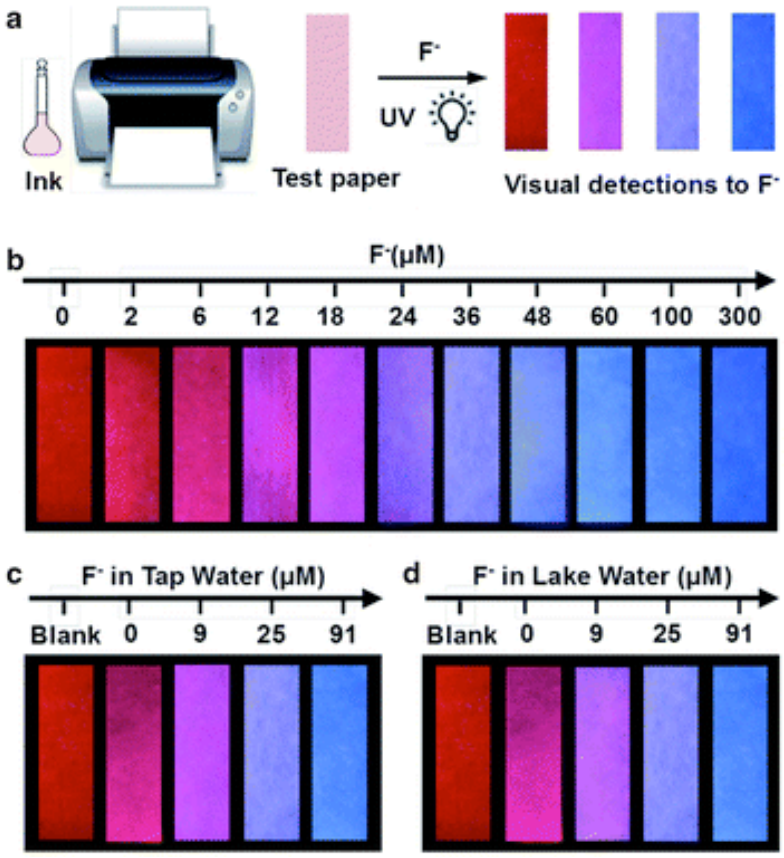

Figure 6. Ratiometric FRET to detect fluoride concentration of water samples on paper-based substrates: **a** test paper preparation; **b** F^- detection in DI water; **c** in tap water; **d** in lake water

Smartphone hardware

Light sources

Paper-based microfluidics has proven the ability to provide flow without the use of external pumps or high voltage power sources (necessary for most silicone or PDMS-based microfluidic devices), but rather by spontaneous capillary action amongst paper fibers (also known as wicking). With the addition of a fluorescence detection method for an analyte (protein, cell, or nucleic acid), a light source is required. When using fluorophores, specific excitation wavelengths are important in order to obtain the desired emission spectra. This being the case, most smartphone-based fluorescent assays incorporate external light sources, the most popular

being a handheld UV lamp or separate LED [81,88,89]. Taking this into account, various platforms have been designed to accessorize and power an external light source having thespecific wavelength needed for fluorescent sensing on paper platforms.

3D-printed plastic attachments that are custom-fitted to a smartphone is most often used, where a built-in LED can be housed along with additional reflectors, collimators, and filters to improve signals [90–92]. Such attached enclosures provide a controlled environment in terms of lighting and spatial distances to improve reproducibility between assays. However, smartphone dimensions and availability vary greatly across manufacturers and models (also by the use of protective cases and covers), making custom attachments undesirable due to its poor adaptability. Along with using an external light source, an external power source is also required.

An innovative method of powering an external LED with the required excitation wavelength is the integration of a galvanic cell, also known as a fluidic battery. Fluidic batteries are foldable and stackable hydrophilic paper layers with printed hydrophobic wax barriers as shown in Figure 7. With the application of a water droplet, the fluidic battery powers an LED until it is run dried. The main requirements of a fluidic battery are 1) electrolytes (i.e. $AgNO_3$, $AgCl_3$, $AgNO_2$, or $MgCl_2$), 2) electrodes (i.e. silver metals, aluminum metals, or magnesium foil), 3) salt bridges (i.e. containing $NaNO_3$), and 4) conductive connections (i.e. copper tape) [93–95].

Instead of using external light source, the white on-board LED flash on a smartphone can be also used as an excitation source to create a fully smartphone-integrated platform [96–99]. However, band-pass or low-pass fitted filters are often used to separate out exclusive wavelengths for excitation, as smartphone flashes generate “white” light [98,100].

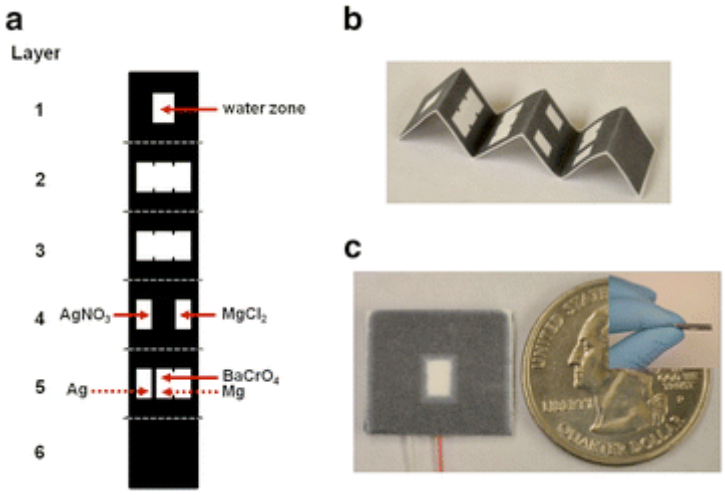

Figure 7. Self-powered paper microfluidic device, utilizing origami paper and galvanic cell, for enzymatic (alkaline phosphatase) fluorescent assay with smartphone detection: **a** device layout; **b** paper folding; **c** top and side view of final assembly

Optical filters

Typical means of isolating fluorescence emission include the use of optical filters. Low-, high-, band-pass, or other filters inserted prior to the receiving detector (i.e., the CMOS array sensor, the most common camera used for smartphones) increases the selectivity of emitted fluorescent light. Not only can these filters differentiate wavelengths, but can also serve as a means for controlling unwanted scattered and diffracted light. Two types of optical filters are commonly used for fluorescence detection. The first type is an absorption filter, in which absorption at the excitation wavelength is desirable and absorption at the emission wavelength is undesirable. In contrast, interference filter have low absorption at the excitation wavelength and high absorption at the emission wavelength.

Interference filters are comprised of multiple thin layers of dielectric material with different refractive indices. Selectivity for the wavelength of interest is dictated by the mechanistic pathways that light travels at the fabricated boundary layers. UV excitation is a very

commonly seen in fluorescence nanotechnology (most notably quantum dots). This can be very problematic since the optimum excitation wavelength for cellulose paper is within the UV spectrum. Therefore, numerous UV filters have been developed to optimize the use of UV excitation in these devices. Other filters developed include a filter developed by Dattner and Yadid-Pecht [101], which is a transparent, poly-acrylic acid (PAA) emission filter, mounted on a low-light CMOS array sensor for selecting red fluorescence. Similarly, Richard et al. [102] fabricated a 9 layer interference filter to select 650 nm red emission from quantum dots with 532 nm excitation wavelength. The final filter was integrated into a silicone-based (thus optically transparent) microfluidic device equipped with a CMOS array sensor (Figure 8).

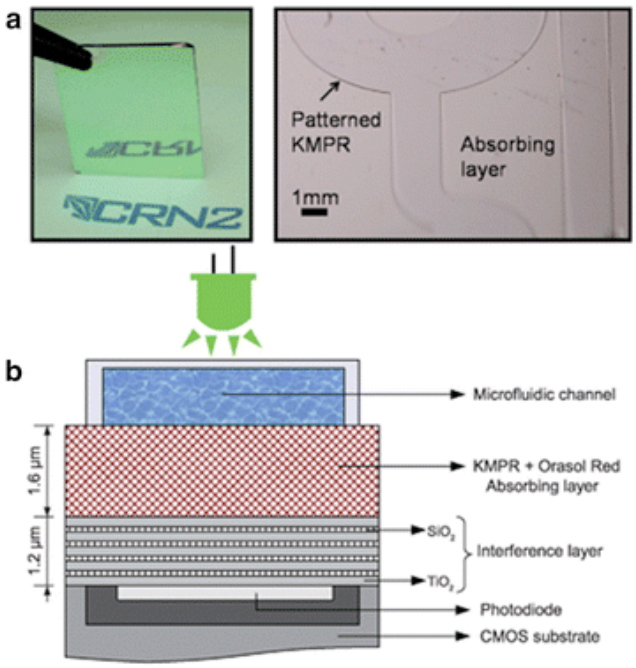

Figure 8. Interference filter added on a microfluidic device: **a** interference filter deposited on glass substrate (left) and patterned microfluidic channels on absorbing layer (right); **b** overall schematics

In comparison, absorption filters are comprised of one single layer. Absorptivity can be adjusted by the overall thickness of the filter and can be modeled using the Beer-Lambert Law, $A = \varepsilon \times l \times c$, where ε is the characteristic molar absorptivity of the filter, l is the path length or thickness of the filter, and c is the concentration of the absorbing material [101,103]. Absorption properties can also be controlled by the addition of dyes such as Sudan II [104,105], Orasol Red BL, KMPR® 1005 epoxy-based photoresist [102], Aptina green1, and Aptina red1 [106]. Other unique filters can also be used to further enhance the fluorescent images that are collected. Lee et al. [107] demonstrated the use of a silo-filter comprised of metal lattices, which were used as dividends for individual pixels and light guides for fluorescent light to penetrate an absorptive, thick filter layer. The metal surfaces of the silo-filter contribute an enhanced scattering and reflectance effect, improving transmittance and overall background rejection. Photonic structures are also another widely used filtering component for controlling fluorescence emission by means of specifically patterned surfaces on gold [108] and plastic [109]. In an optofluidic chip developed by Ricciardi et al. [110], a fluorescence immunoassay was demonstrated for the detection of actin-actin antibody complexes with superior repeatability and a lower limit of detection. They utilized unique photonic structures for controlled light diversion into a fluorescence microscope apparatus. Similarly, Schudel et al. [111] developed a silicone-based microfluidic chip array that utilized Actuate-to-Open valve mixing and photonic crystal nanostructures to detect the binding of IgG to various proteins in an immunofluorescent assay using a charge-coupled device (CCD) array sensor.

Addressing autofluorescence of paper

It is widely known that cellulose-based paper substrates exhibit autofluorescence due to their treatment with optical-brighteners such as Calcofluor. Cellulose paper treated in this manner is strongly excited in the UV, generating blue/green emissions [112]. Therefore the unwanted background autofluorescence, along with back scattering from the paper surface, must be addressed. Also with the use of biological samples, autofluorescence and back-scattering light from paper surfaces can be even more problematic [113,114].

Pulse excitation and time-resolved detection

Traditional photo-detection instrumentations are designed to receive photons continuously during the excitation period. As a result, mitigation of unwanted background noise (especially autofluorescence) can be difficult. Pulse excitation and time-resolved detection are methods in which fluorophores are acutely exposed to an excitation light. From the collected fluorescent decay, a lifetime value can be determined that is unique to a fluorophore of interest. The measured lifetime can be crucial in resolving between background autofluorescence and detection-related fluorescence. Therefore, designation and separation of timed windows, short lifetime decays of autofluorescence (delay time) and long lifetime decays of fluorophores of interest (gate time), can be easily distinguished and collected as seen in Figure 9 [83,113,115].

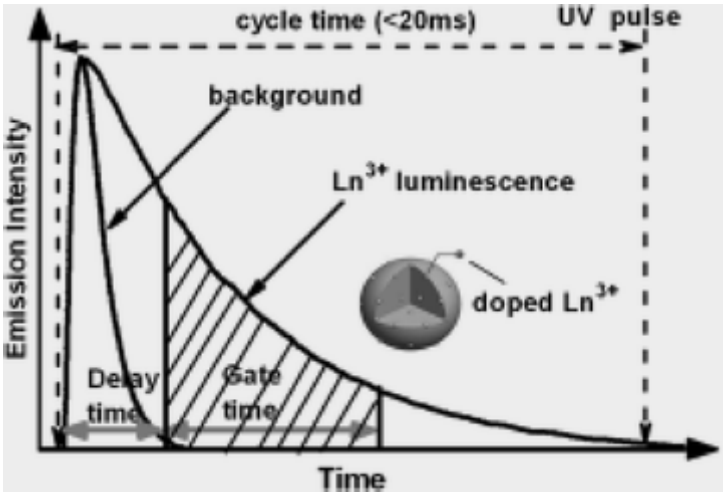

Figure 9. Mechanism of time-resolved fluorescence as a means of eliminating short lifetime background and autofluorescence

Ju et al. [115] developed lanthanide (Ln^{3+}) doped GdF_3 nanocrystals that successfully detected avidin protein under time-resolved fluorometric measurements with promising applications in immunoassays, multiplexing, and DNA hybridization. Wang et al. [83] demonstrated the use of time-resolved fluorescence in conjunction with ratiometric measurements using a smartphone on a paper-based platform to detect dipicolinic acid (DPA), a biomarker for anthrax presence. Lanthanide-terbium (Ln-Tb) and -europium (Ln-Eu) doped fluorescent crystals (Tb/DPA@SiO_2-Eu/GMP) when exposed to a 254 nm UV lamp and DPA, resulted in an indicating red fluorescence, as opposed to a control green fluorescence signal. The spectra was further refined by using a delay time of 50 μs and gate time of 2 ms to avoid autofluorescence. Similarly, Kim et al. [116] demonstrated the use of time-resolved fluorescence measurements to study the enhanced fluorescence resonance energy transfer (FRET) efficiency and increased fluorescent lifetime of immobilized quantum dots on a paper platform in comparison to a solution assay. The four-fold enhancement in FRET rate was concluded and attributed to the decreased average distance between quantum dot donor and acceptor dye for the

paper-based platform. Overall, colored digital images were captured and analyzed under a 405 nm UV LED to analyze trypsin proteolytic activity and inactivity in the presence of aprotinin inhibition. Paterson et al. [117] utilized a smartphone time-gated imaging application to capture images at set intervals after pulse excitation to detect human chorionic gonadotropin (hCG) with strontium aluminate nanoparticles on a LFA (Figure 10).

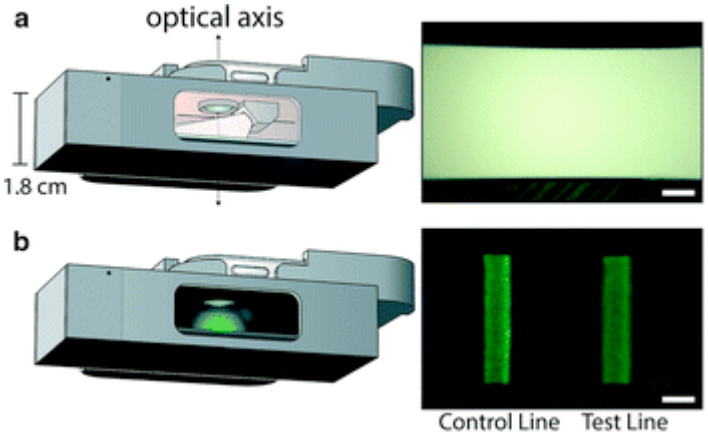

Figure 10. Smartphone attachment utilizing the onboard "white" LED flash as a light source, using pulse excitation to address the paper's autofluorescence, for detecting human chorionic gonadotropin (hCG) on LFA strip: **a** smartphone's flash is turned on for short excitation; **b** flash is turned off showing luminescence imaging

Autofluorescence indexing

Up until now, what has been discussed are methods to avoid, normalize, or subtract the inherent autofluorescence of paper matrices. In a recent publication from Shah and Yager [118], a systematic "autofluorescence index" was proposed using excitation-emission matrices for screening and selecting paper substrates for low autofluorescence when developing assays.

Conventionally, primarily and solely spectral overlap is considered between target-induced fluorescence and paper overfluorescence. In Shah and Yager's study, 12 common-used paper matrices, including nitrocellulose, glass fiber, and cellulose, were evaluated using the developed autofluorescence index equations. The proposed quantification of autofluorescence was further investigated and demonstrated using a quantum dot lateral flow immunoassay for detection of influenza A nucleoprotein. It was concluded that paper matrices with lower calculated autofluorescence indices had lower limits of detections.

Use of NIR

Autofluorescence of paper can also be avoided by using longer excitation wavelengths, e.g. near infrared (NIR) or infrared (IR) [119–122]. Yu and White [123] observed that background autofluorescence of paper was reduced using 785 nm excitation in assaying Rhodamine6G, organophosphate malathion, heroin, and cocaine from a surface-enhanced Raman spectroscopy dipstick swab. Similarly, Ju et al. [124] found using longer IR or NIR wavelengths as the excitation source reduced autofluorescence as well as undesired back scattering. Their paper-based platform utilizing lanthanide-doped $LiYF_4$ upconversion nanoparticles demonstrated a limit of detection of 3.6 fmol of DNA. Doughan et al. [125] used a 980 nm NIR excitation to reduce background noise that usually corresponds with UV or visible wavelength excitation.

Smartphone-based optical sensing of fluorescence emission is of recent development and has shown numerous technical and physical limitations, especially on paper platforms. However, recent implementation of filters, advanced image processing, and unique platform development show improved results to better address such challenges. Hopefully in the near future, the benefits of contact CMOS imagers could be incorporated into smartphone-based fluorescence sensing on paper-based platforms.

OVERVIEW OF DISSERTATION

Standard diagnostic tools used from patient samples, specifically from blood draws, require specialized equipment, personnel, and facilities. Conventional techniques can often be very laborious and time consuming due to required sample preparation. The evident delay from sample collection to a patient's result immensely impacts their outcome. The aims of this research are to design diagnostic biosensors that decrease time-to-results, minimize reagent and sample handling, and incorporate automated simple optical transduction and user interfaces for the detection of blood-derived biomarkers. Specifically, four biosensing detection mechanisms performed on 3 different point-of-care platforms will be discussed.

First is a static loop-mediated isothermal amplification (LAMP) of nucleic acid aqueous droplet on a silicone chip platform immersed in mineral oil. The target-of-interest is a nucleic acid sequence as a biomarker for antibiotic resistant bacteria, *rfbE* gene in *Escherichia coli* O157:H7. The biosensing technique used related changes in interfacial tension (IFT) at the water-oil interface by measuring the change in contact angle (geometrical-effects) over time. Contact angle, the angle between the plane and the curvature of the droplet, can be directly correlated to the energy vector adjacent to the liquid-vapor phase via Young's Equation. Contact angle is a conventional method to determine surface characteristics such as hydrophobicity and hydrophilicity. Initially the system was characterized as a linear response in relation to concentration of bacteria in a buffer system down to the limit of detection (LOD) of 100 CFU per μL. Subsequently, with the addition of bacterial infected blood sample models, the system became a binary assay (i.e. yes or no) as low as 10 CFU per μL within 10 min of reaction. The major difference between the two systems is the utilization of blood. Blood is complex matrix, which means numerous proteins are present that compete with the available surface area at the water-oil interface due to preferential adsorption. Overall, time-to-results were as fast as 5 min,

being within the window of time for physicians to prescribe adequate treatment for blood stream infection diagnosis.

Secondly, a two-layered, paper microfluidic chip was utilized to quantify cancer cells from a buffy coat sample matrix by two detection mechanisms: 1st layer (capture layer) on-chip particle enumeration via smartphone microscope and 2nd layer (flow layer) capillary flow dynamics via smartphone video processing. On-chip whole cancer cell enumerations were validated via benchtop fluorescence microscopy and smartphone florescence microscopy. On both benchtop and smartphone fluorescence microscope methods, number of particles in field of view (FOV) for 1, 10, and 100 cells per μL were statistically different in comparison to no-target-control (NTC) samples. Flow rate analysis to quantify antigen/cell fragment concentration detected significant signals for 0.1 to 100 cells per μL within the first 6 s of assay. To validate flow detection mechanism, a modified Lucas-Washburn (L-W) model was investigated and applied utilizing measured viscosity and interfacial tension. Empirical data and L-W model showed great alignment with flow velocities between 13 and 22s after sample loading. Proposed device and assay platform is able to capture and on-chip image cancer cells within a complex sample matrix (buffy coat) while simultaneously quantifying cell concentration in a point-of-care manner.

Lastly, the same concepts previously described in the first platform utilizes changes in IFT due to amplicon presence in an aqueous solution immersed in mineral oil. An emulsion LAMP platform was investigated to determine the relation between angle-dependent light scatter intensity (based off Mie scatter theory) and nucleic acid amplification progression. Again, the target gene-of-interst is a biomarker for antibiotic resistnace, specifically *rfbE* gene in *Escherichia coli* O157:H7. The phenomenon attributing to changes in light scatter intensities is due to the interfacial changes occurring in the emulsion droplets, where amplicon amount

increases the IFT decreases, resulting in smaller diameter emulsions. Via spectrophotometers and fiber optic cables placed at 30° and 60° light scatter intensity was monitored. Light scatter intensities collected at 3 min, 30° was able to statistically differentiate 10^3 and 10^6 copies per μL initial concentrations in comparison to NTC (0 copies per μL). Similarly, 3 min light scatter intensities collected at 60° were able to statistically differentiate 10^6 per μL initial concentrations in comparison to NTC. Furthermore, control experiments were conducted to validate nucleic acid detection versus protein adsorption and found 30° light scatter intensity can be used to quantify protein adsorption (bacteria concentration), while 60° light scatter intensity can be used to quantify nucleic acid presence. A smartphone, blinking LED set up was designed and fabricated to mirror previous spectrophotometer set up to demonstrate a user-friendly and field-deployable platform. Light scatter trends via time lapsed images in correspondence to angle-specific LED blinking were comparable to spectrophotometer set up. These four detection mechanisms and three platforms offer but a few alternatives as biosensing methods for blood-derived diagnostic biosensors.

REFERENCES

1. G. Vernet, Molecular Diagnostics in Virology. Journal of Clinical Virology **31**, 239 (2004).

2. O. Dauwalder, L. Landrieve, F. Laurent, M. de Montclos, F. Vandenesch, and G. Lina, Does Bacteriology Laboratory Automation Reduce Time to Results and Increase Quality Management? Clinical Microbiology and Infection **22**, 236 (2016).

3. R. Dadoun, Case study: automation's impact on productivity and turnaround time. Medical Laboratory Observer (2002).

4. G. A. Posthuma-Trumpie, J. Korf, and A. van Amerongen, Lateral Flow (Immuno)Assay: Its Strengths, Weaknesses, Opportunities and Threats. A Literature Survey. Anal Bioanal Chem **393**, 569 (2009).

5. P. Yager, T. Edwards, E. Fu, K. Helton, K. Nelson, M. R. Tam, and B. H. Weigl, Microfluidic Diagnostic Technologies for Global Public Health. Nature **442**, 412 (2006).

6. S. K. Sia and L. J. Kricka, Microfluidics and Point-of-Care Testing. Lab Chip **8**, 1982 (2008).

7. Á. Ríos, M. Zougagh, and M. Avila, Miniaturization through Lab-on-a-Chip: Utopia or Reality for Routine Laboratories? A Review. Analytica Chimica Acta **740**, 1 (2012).

8. S. Kumar, S. Kumar, M. A. Ali, P. Anand, V. V. Agrawal, R. John, S. Maji, and B. D. Malhotra, Microfluidic-Integrated Biosensors: Prospects for Point-of-Care Diagnostics. Biotechnol J **8**, 1267 (2013).

9. Zhou Jinwen, Khodakov Dmitriy A., Ellis Amanda V., and Voelcker Nicolas H., Surface Modification for PDMS-based Microfluidic Devices. ELECTROPHORESIS **33**, 89 (2011).

10. K. Scida, B. Li, A. D. Ellington, and R. M. Crooks, DNA Detection Using Origami Paper Analytical Devices. Anal. Chem. **85**, 9713 (2013).

11. W. Zhao, A. van den Berg, Lab on paper, Lab Chip **8**, 1988 (2008).

12. J.-Y. Yoon, *Introduction to Biosensors: From Electric Circuits to Immunosensors* (Springer, 2016).

13. D. J. You, T. S. Park, and J.-Y. Yoon, Cell-Phone-Based Measurement of TSH Using Mie Scatter Optimized Lateral Flow Assays. Biosensors and Bioelectronics **40**, 180 (2013).

14. S. Cho, T. S. Park, T. G. Nahapetian, and J.-Y. Yoon, Smartphone-Based, Sensitive MPAD Detection of Urinary Tract Infection and Gonorrhea. Biosensors and Bioelectronics **74**, 601 (2015).

15. M. L. Wilson and L. Gaido, Laboratory Diagnosis of Urinary Tract Infections in Adult Patients. Clinical Infectious Diseases **38**, 1150 (2004).

16. Jodal U., Lindberg U., and Lincoln K., Level Diagnosis of Symptomatic Urinary Tract Infections in Childhood. Acta Paediatrica **64**, 201 (2008).

17. S. P. Johnston, M. M. Ballard, M. J. Beach, L. Causer, and P. P. Wilkins, Evaluation of Three Commercial Assays for Detection of Giardia and Cryptosporidium Organisms in Fecal Specimens. J. Clin. Microbiol. **41**, 623 (2003).

18. ThermoFisher Scientific, DAPI (4-,6-diamidino-2-phenylindole (n.d.).

19. Sigma-Aldrich, SYBR ® Green Based Quantitative PCR (n.d.).

20. Chorma (R), Fluorochrome Spectra (2014).

21. C. O'Connor, Fluorescence In Situ Hybridization (FISH) Nature Education **1**, (2008).

22. V. A. J. Kempf, K. Trebesius, and I. B. Autenrieth, Fluorescent In Situ Hybridization Allows Rapid Identification of Microorganisms in Blood Cultures, J. CLIN. MICROBIOL. **38**, 9 (2000).

23. M. Schliwa, A tumor promoter induces rapid and coordinated reorganization of actin and vinculin in cultured cells, The Journal of Cell Biology **99**, 1045 (1984).

24. A. Kinkhabwala, Z. Yu, S. Fan, Y. Avlasevich, K. Müllen, and W. E. Moerner, Large single-molecule fluorescence enhancements produced by a bowtie nanoantenna, Nature Photonics **3**, 654 (2009).

25. H. Jin, D. A. Heller, M. Kalbacova, J.-H. Kim, J. Zhang, A. A. Boghossian, N. Maheshri, and M. S. Strano, Detection of single-molecule H_2O_2 signalling from epidermal growth factor receptor using fluorescent single-walled carbon nanotubes. Nat. Nanotechnol. **5**, 302–309 (2010).

26. L. P. McGuinness, Y. Yan, A. Stacey, D. A. Simpson, L. T. Hall, D. Maclaurin, S. Prawer, P. Mulvaney, J. Wrachtrup, F. Caruso, R. E. Scholten, and L. C. L. Hollenberg, Quantum measurement and orientation tracking of fluorescent nanodiamonds inside living cells. Nat. Nanotechnol. **6**(6), 358–363 (2011).

27. S. Tabassum, W. M. Al-Asbahy, M. Afzal, F. Arjmand, and R. H. Khan, Interaction and photo-induced cleavage studies of a copper based chemotherapeutic drug with human serum albumin: spectroscopic and molecular docking study. Mol. BioSyst. **8**(9), 2424–2433 (2012).

28. Z. Li, Y. Wang, J. Wang, Z. Tang, J. G. Pounds, and Y. Lin, Rapid and sensitive detection of protein biomarker using a portable fluorescence biosensor based on quantum dots and a lateral flow test strip. Anal. Chem. **82**(16), 7008–7014 (2010).

29. J. A. Hansen, J. Wang, A.-N. Kawde, Y. Xiang, K. V. Gothelf, and G. Collins, Quantum-dot/aptamer-based ultrasensitive multi-analyte electrochemical biosensor. J. Am. Chem. Soc. **128**(7), 2228–2229 (2006).

30. A. Zajac, D. Song, W. Qian, and T. Zhukov, Protein microarrays and quantum dot probes for early cancer detection. Colloids Surf. B **58**(2), 309–314 (2007).

31. M. Zhuang, C. Ding, A. Zhu, and Y. Tian, Ratiometric fluorescence probe for monitoring hydroxyl radical in live cells based on gold nanoclusters. Anal. Chem. **86**(3), 1829–1836 (2014).

32. Y. Wang, L. Ge, P. Wang, M. Yan, S. Ge, N. Li, J. Yu, and J. Huang, Photoelectrochemical lab-on-paper device equipped with a porous Au-paper electrode and fluidic delay-switch for sensitive detection of DNA hybridization. Lab Chip **13**(19), 3945–3955 (2013).

33. M. Ferrari, Cancer nanotechnology: opportunities and challenges. Nat. Rev. Cancer **5**(3), 161–171 (2005).

34. M. Wu, Q. Lai, Q. Ju, L. Li, H.-D. Yu, and W. Huang, Paper-based fluorogenic devices for in vitro diagnostics. Biosens. Bioelectron. **102**, 256–266 (2018).

35. S. Fiorito, A. Serafino, F. Andreola, A. Togna, and G. Togna, Toxicity and biocompatibility of carbon nanoparticles. J. Nanosci. Nanotechnol. **6**(3), 591–599 (2006).

36. S. Murugesan, T.-J. Park, H. Yang, S. Mousa, and R. J. Linhardt, Blood compatible carbon nanotubes—nano-based neoproteoglycans. Langmuir **22**(8), 3461–3463 (2006).

37. R. Shukla, V. Bansal, M. Chaudhary, A. Basu, R. R. Bhonde, and M. Sastry, Biocompatibility of gold nanoparticles and their endocytotic fate inside the cellular compartment: a microscopic overview. Langmuir **21**(3), 10644–10654 (2005).

38. X. Hu and X. Gao, Multilayer coating of gold nanorods for combined stability and biocompatibility. Phys. Chem. Chem. Phys. **13**(21), 10028–10035 (2011).

39. A. W. Martinez, S. T. Phillips, E. Carrilho, S. W. Thomas, H. Sindi, and G. M. Whitesides, Simple telemedicine for developing regions: camera phones and paper-based microfluidic devices for real-time, off-site diagnosis. Anal. Chem. **80**(10), 3699–3707 (2008).

40. A. K. Yetisen, J. L. Martinez-Hurtado, A. Garcia-Melendrez, F. da Cruz Vasconcellos, and C. R. Lowe, A smartphone algorithm with inter-phone repeatability for the analysis of colorimetric tests. Sens. Actuators B-Chem. **196**, 156–160 (2014).

41. ThermoFisher, PCR Basics (n.d.).

42. W. A. Al-Soud and P. Rådström, Purification and characterization of PCR-inhibitory components in blood cells. Journal of Clinical Microbiology **39**, 345 (2001).

43. D. N. Fredricks and D. A. Relman, Improved Amplification of Microbial DNA from Blood Cultures by Removal of the PCR Inhibitor Sodium Polyanetholesulfonate. Journal of Clinical Microbiology **36**, 2810 (1998).

44. W. A. Schell, J. L. Benton, P. B. Smith, M. Poore, J. L. Rouse, D. J. Boles, M. D. Johnson, B. D. Alexander, V. K. Pamula, A. E. Eckhardt, M. G. Pollack, D. K. Benjamin, J. R. Perfect, and T. G. Mitchell, Evaluation of a digital microfluidic real-time PCR platform to detect DNA of Candida albicans in blood. Eur J Clin Microbiol Infect Dis **31**, 2237 (2012).

45. C. Chen, J. Skog, C.-H. Hsu, R. T. Lessard, L. Balaj, T. Wurdinger, B. S. Carter, X. O. Breakefield, M. Toner, and D. Irimia, Microfluidic isolation and transcriptome analysis of serum microvesicles. Lab Chip **10**, 505 (2010).

46. S. Park, Y. Zhang, S. Lin, T.-H. Wang, and S. Yang, Advances in microfluidic PCR for point-of-care infectious disease diagnostics. Biotechnology Advances **29**, 830 (2011).

47. A. Niemz, T. M. Ferguson, and D. S. Boyle, Point-of-care nucleic acid testing for infectious diseases. Trends Biotechnol. **29**, 240 (2011).

48. Y. Mori and T. Notomi, Loop-mediated isothermal amplification (LAMP): a rapid, accurate, and cost-effective diagnostic method for infectious diseases. J. Infect. Chemother. **15**, 62 (2009).

49. T. Notomi, H. Okayama, H. Masubuchi, T. Yonekawa, K. Watanabe, N. Amino, and T. Hase, Loop-mediated isothermal amplification of DNA. Nucleic Acids Res. **28**, e63 (2000).

50. K. Hsieh, A. S. Patterson, B. S. Ferguson, K. W. Plaxco, and H. T. Soh, Rapid, sensitive, and quantitative detection of pathogenic DNA at the point of care through microfluidic electrochemical quantitative loop-mediated isothermal amplification. Angew. Chem.-Int. Edit. **51**, 4896 (2012).

51. M. Safavieh, M. U. Ahmed, M. Tolba, and M. Zourob, Microfluidic electrochemical assay for rapid detection and quantification of Escherichia coli. Biosens. Bioelectron. **31**, 523 (2012).

52. R. D. Stedtfeld, D. M. Tourlousse, G. Seyrig, T. M. Stedtfeld, M. Kronlein, S. Price, F. Ahmad, E. Gulari, J. M. Tiedje, and S. A. Hashsham, Gene-Z: a device for point of care genetic testing using a smartphone. Lab Chip **12**, 1454 (2012).

53. C. Liu, E. Geva, M. Mauk, X. Qiu, W. R. Abrams, D. Malamud, K. Curtis, S. M. Owen, and H. H. Bau, An isothermal amplification reactor with an integrated isolation membrane for point-of-care detection of infectious diseases. Analyst **136**, 2069 (2011).

54. A. Priye, S. W. Bird, Y. K. Light, C. S. Ball, O. A. Negrete, and R. J. Meagher, A smartphone-based diagnostic platform for rapid detection of Zika, Chikungunya, and Dengue viruses. Sci. Rep. **7**, 44778 (2017).

55. S. J. Oh, B. H. Park, G. Choi, J. H. Seo, J. H. Jung, J. S. Choi, D. H. Kim, and T. S. Seo, Fully automated and colorimetric foodborne pathogen detection on an integrated centrifugal microfluidic device. Lab Chip **16**, 1917 (2016).

56. A. Sayad, F. Ibrahim, S. M. Uddin, J. Cho, M. Madou, and K. L. Thong, A microdevice for rapid, monoplex and colorimetric detection of foodborne pathogens using a centrifugal microfluidic platform. Biosens. Bioelectron. **100**, 96 (2018).

57. C.-H. Wang, K.-Y. Lien, J.-J. Wu, and G.-B. Lee, A magnetic bead-based assay for the rapid detection of methicillin-resistant Staphylococcus aureus by using a microfluidic system with integrated loop-mediated isothermal amplification. Lab Chip **11**, 1521 (2011).

58. S. D. Polley, Y. Mori, J. Watson, M. D. Perkins, I. J. Gonzalez, T. Notomi, P. L. Chiodini, and C. J. Sutherland, Mitochondrial DNA targets increase sensitivity of malaria detection using loop-mediated isothermal amplification. J. Clin. Microbiol. **48**, 2866 (2010).

59. D. K. Harshman, B. M. Rao, J. E. McLain, G. S. Watts, and J.-Y. Yoon, Innovative qPCR using interfacial effects to enable low threshold cycle detection and inhibition relief. Sci Adv. **1**, e1400061 (2015).

60. X. Xu, A. Akay, H. Wei, S. Wang, B. Pingguan-Murphy, B. E. Erlandsson, X. Li, W. Lee, J. Hu, L. Wang, and F. Xu, Advances in smartphone-based point-of-care diagnostics. Proc. IEEE **103**(2), 236–247 (2015).

61. K. E. McCracken and J.-Y. Yoon, Recent approaches for optical smartphone sensing in resource-limited settings: a brief review. Anal. Meth. **8**(36), 6591–6601 (2016).

62. S. K. Vashist, O. Mudanyali, E. M. Schneider, R. Zengerle, and A. Ozcan, Cellphone-based devices for bioanalytical sciences. Anal. Bioanal. Chem. **406**(14), 3263–3277 (2014).

63. D. Paliy, A. Foi, R. Bilcu, and V. Katkovnik, Denoising and interpolation of noisy Bayer data with adaptive cross-color filters. Proc. SPIE **6822**, 68221K (2008).

64. X. Jin, Z. Liu, and J. Chen, CMOS vision sensor with fully digital image process integrated into low power 1/8-inch chip. Chin. Opt. Lett. **8**(3), 282–285 (2010).

65. R. Fontaine, A survey of enabling technologies in successful consumer digital imaging products. In: Proceedings of the international image sensors workshop, Hiroshima, Japan, 30 May—2 June 2017 (2017).

66.. S.-J. Qin and B. Yan, The point-of-care colorimetric detection of the biomarker of phenylamine in the human urine based on Tb^{3+} functionalized metal-organic framework. Anal. Chim. Acta **1012**, 82–89 (2018).

67. H. Xu, K. Zhang, Q. Liu, Y. Liu, and M. Xie, Visual and fluorescent detection of mercury ions by using a dually emissive ratiometric nanohybrid containing carbon dots and CdTe quantum dots. Microchim. Acta **184**(4), 1199–1206 (2017).

68. X. Wang, S. Wang, K. Huang, Z. Liu, Y. Gao, and W. Zeng, A ratiometric upconversion nanosensor for visualized point-of-care assay of organophosphonate nerve agent. Sens. Actuators B-Chem. **241**, 1188–1193 (2017).

69. R. R. Anjana, J. S. A. Devi, M. Jayasree, R. S. Aparna, B. Aswathy, G. L. Praveen, G. M. Lekha, and G. Sony, S,N-doped carbon dots as a fluorescent probe for bilirubin. Microchim. Acta **185**, UNSP 11 (2018).

70. P. Das and U. J. Krull, Detection of a cancer biomarker protein on modified cellulose paper by fluorescence using aptamer-linked quantum dots. Analyst **142**(17), 3132–3135 (2017).

71. X. Weng and S. Neethirajan, Aptamer-based fluorometric determination of norovirus using a paper-based microfluidic device. Microchim. Acta **184**(11), 4545–4552 (2017).

72. B. Li, X. Zhou, H. Liu, H. Deng, R. Huang, and D. Xing, Simultaneous detection of antibiotic resistance genes on paper-based chip using [Ru(phen)2d ppz]2+ turn-on fluorescence probe. ACS Appl. Mater. Interfaces. **10**(5), 4494–4501 (2018).

73. Y. Seok, H.-A. Joung, J.-Y. Byun, H.-S. Jeon, S. J. Shin, S. Kim, Y.-B. Shin, H. S. Han, and M.-G. Kim, A paper-based device for performing loop-mediated isothermal amplification with real-time simultaneous detection of multiple DNA targets. Theranostics **7**(8), 2220–2230 (2017).

74. K. Salama, H. Eltoukhy, A. Hassibi, and A. E. Gamal, Modeling and simulation of luminescence detection platforms. Biosens. Bioelectron. **19**(11), 1377–1386 (2004).

75. X. F. Li, Q. H. Wang, D. H. Li, and A. H. Wang, Image processing to eliminate crosstalk between neighboring view images in three-dimensional lenticular display. J. Disp. Technol. **7**(8), 443–447 (2011).

76. L. Shen, J. A. Hagen, and I. Papautsky, Point-of-care colorimetric detection with a smartphone. Lab Chip **12**(21), 4240–4243 (2012).

77. K. E. McCracken, S. V. Angus, K. A. Reynolds, and J.-Y. Yoon, Multimodal imaging and lighting bias correction for improved μPAD-based water quality monitoring via smartphones. Sci. Rep. **6**, 27529 (2016).

78. R. B. Sekar and A. Periasamy, Fluorescence resonance energy transfer (FRET) microscopy imaging of live cell protein localizations. J. Cell Biol. **160**(5), 629–633 (2003).

79. B. A. Pollok and R. Heim, Using GFP in FRET-based applications. Trends Cell Biol. **9**(2), 57–60 (1999).

80. E. A. Jares-Erijman and T. M. Jovin, FRET imaging. Nat. Biotechnol. **21**(11), 1387–1395 (2003).

81. M. O. Noor and U. J. Krull, Camera-based ratiometric fluorescence transduction of nucleic acid hybridization with reagentless signal amplification on a paper-based platform using immobilized quantum dots as donors. Anal. Chem. **86**(20), 10331–10339 (2014).

82. S. A. Díaz, L. Giordano, T. M. Jovin, and E. A. Jares-Erijman, Modulation of a photoswitchable dual-color quantum dot containing a photochromic FRET acceptor and an internal standard. Nano Lett. **12**(7), 3537–3544 (2012).

83. Q.-X. Wang, S.-F. Xue, Z.-H. Chen, S.-H. Ma, S. Zhang, G. Shi, and M. Zhang, Dual lanthanide-doped complexes: the development of a time-resolved ratiometric fluorescent probe for anthrax biomarker and a paper-based visual sensor. Biosens. Bioelectron. **94**, 388–393 (2017).

84. C. M. Tyrakowski and P. T. Snee, Ratiometric CdSe/ZnS quantum dot protein sensor. Anal. Chem. **86**(5), 2380–2386 (2014).

85. K. Wang, J. Qian, D. Jiang, Z. Yang, X. Du, and K. Wang, Onsite naked eye determination of cysteine and homocysteine using quencher displacement-induced fluorescence recovery of the dual-emission hybrid probes with desired intensity ratio. Biosens. Bioelectron. **65**, 83–90 (2015).

86. W. Russ Algar, M. Massey, and U. J. Krull, The application of quantum dots, gold nanoparticles and molecular switches to optical nucleic-acid diagnostics. Trends Anal. Chem. **28**(3), 292–306 (2009).

87. X. Yu, L. Yang, T. Zhao, R. Zhang, L. Yang, C. Jiang, J. Zhao, B. Liu, and Z. Zhang, Multicolorful ratiometric-fluorescent test paper for determination of fluoride ions in environmental water. RSC Adv. **7**(84), 53379–53384 (2017).

88. M. Dou, D. C. Dominguez, X. Li, J. Sanchez, and G. Scott, A versatile PDMS/paper hybrid microfluidic platform for sensitive infectious disease diagnosis. Anal. Chem. **86**(15), 7978–7986 (2014).

89. M. G. Caglayan, S. Sheykhi, L. Mosca, and P. Anzenbacher, Fluorescent zinc and copper complexes for detection of adrafinil in paper-based microfluidic devices. Chem. Commun. **52**(53), 8279–8282 (2016).

90. S.-J. Yeo, K. Choi, B. T. Cuc, N. N. Hong, D. T. Bao, N. M. Ngoc, M. Q. Le, N. L. K. Hang, N. C. Thach, S. K. Mallik, H. S. Kim, C.-K. Chong, H. S. Choi, H. W. Sung, K. Yu, and H. Park, Smartphone-based fluorescent diagnostic system for highly pathogenic H5N1 viruses. Theranostics **6**(2), 231–242 (2016).

91. H. C. Koydemir, Z. Gorocs, D. Tseng, B. Cortazar, S. Feng, R. Y. Lok Chan, J. Burbano, E. McLeod, and A. Ozcan, Rapid imaging, detection and quantification of Giardia lamblia cysts using mobile-phone based fluorescent microscopy and machine learning. Lab Chip **15**(5), 1284–1293 (2015).

92. A. Hossain, J. Canning, S. Ast, P. J. Rutledge, T. L. Yen, and A. Jamalipour, Lab-in-a-phone: smartphone-based portable fluorometer for pH measurements of environmental water. IEEE Sens. J. **15**(9), 5095–5102 (2015).

93. N. K. Thom, K. Yeung, M. B. Pillion, and S. T. Phillips, “Fluidic batteries” as low-cost sources of power in paper-based microfluidic devices. Lab Chip **12**(10), 1768–1770 (2012).

94. Y. Koo, J. Sankar, and Y. Yun, High performance magnesium anode in paper-based microfluidic battery, powering on-chip fluorescence assay. Biomicrofluidics **8**(5), 054104 (2014).

95. N. K. Thom, G. G. Lewis, K. Yeung, and S. T. Phillips, Quantitative fluorescence assays using a self-powered paper-based microfluidic device and a camera-equipped cellular phone. RSC Adv. **4**(3), 1334–1340 (2014).

96. K. E. McCracken, T. Tat, V. Paz, and J.-Y. Yoon, Smartphone-based fluorescence detection of bisphenol A from water samples. RSC Adv. **7**(15), 9237–9243 (2017).

97. K. D. Long, E. V. Woodburn, H. M. Le, U. K. Shah, S. S. Lumetta, and B. T. Cunningham, Multimode smartphone biosensing: the transmission, reflection, and intensity spectral (TRI)-analyzer. Lab Chip **17**(19), 3246–3257 (2017).

98. E. Petryayeva and W. R. Algar, A job for quantum dots: use of a smartphone and 3D-printed accessory for all-in-one excitation and imaging of photoluminescence. Anal. Bioanal. Chem. **408**(11), 2913–2925 (2016).

99. M. A. Hossain, J. Canning, S. Ast, K. Cook, P. J. Rutledge, and A. Jamalipour, Combined “dual” absorption and fluorescence smartphone spectrometers. Opt. Lett. **40**(8), 1737–1740 (2015).

100. J. Canning, A. Lau, M. Naqshbandi, I. Petermann, and M. J. Crossley, Measurement of fluorescence in a rhodamine-123 doped self-assembled “giant” mesostructured silica sphere using a smartphone as optical hardware. Sensors **11**(7), 7055–7062 (2011).

101. Y. Dattner and O. Yadid-Pecht, Low light CMOS contact imager with an integrated poly-acrylic emission filter for fluorescence detection. Sensors **10**(5), 5014–5027 (2010).

102. C. Richard, A. Renaudin, V. Aimez, and P. G. Charette, An integrated hybrid interference and absorption filter for fluorescence detection in lab-on-a-chip devices. Lab Chip **9**(10), 1371–1376 (2009).

103. M. L. Adams, M. Enzelberger, S. Quake, and A. Scherer, Microfluidic integration on detector arrays for absorption and fluorescence micro-spectrometers. Sens. Actuators A-Phys. **104**, 25–31 (2003).

104. O. Hofmann, X. Wang, A. Cornwell, S. Beecher, A. Raja, D. D. C. Bradley, A. J. deMello, and J. C. deMello, Monolithically integrated dye-doped PDMS long-pass filters for disposable on-chip fluorescence detection. Lab Chip **6**(8), 981–987 (2006).

105. M. Beiderman, T. Tam, A. Fish, G. A. Jullien, and O. Yadid-Pecht, A low-light CMOS contact imager with an emission filter for biosensing applications. IEEE Trans. Biomed. Circuits Syst. **2**(3), 193–203 (2008).

106. S. Pang, C. Han, L. Man Lee, and C. Yang, Fluorescence microscopy imaging with a Fresnel zone plate array based optofluidic microscope. Lab Chip **11**(21), 3698–3702 (2011).

107. S. A. Lee, X. Ou, J. E. Lee, and C. Yang, Chip-scale fluorescence microscope based on a silo-filter complementary metal-oxide semiconductor image sensor. Opt. Lett. **38**(11), 1817–1819 (2013).

108. Y.-J. Hung II, Smolyaninov, C. C. Davis, and H.-C. Wu, Fluorescence enhancement by surface gratings. Opt. Express **14**(22), 10825–10830 (2006).

109. D. Gallegos, K. D. Long, H. Yu, P. P. Clark, Y. Lin, S. George, P. Nath, and B. T. Cunningham, Label-free biodetection using a smartphone. Lab Chip **13**(11), 2124–2132 (2013).

110. S. Ricciardi, F. Frascella, A. Angelini, A. Lamberti, P. Munzert, L. Boarino, R. Rizzo, A. Tommasi, and E. Descrovi, Optofluidic chip for surface wave-based fluorescence sensing. Sens. Actuators B Chem. **215**, 225–230 (2015).

111. B. R. Schudel, C. J. Choi, B. T. Cunningham, and P. J. A. Kenis, Microfluidic chip for combinatorial mixing and screening of assays. Lab Chip **9**(12), 1676–1680 (2009).

112. T. L. Danielson, G. D. Rayson, D. M. Anderson, R. Estell, E. L. Fredrickson, and B. S. Green, Impact of filter paper on fluorescence measurements of buffered saline filtrates. Talanta **59**(3), 601–604 (2003).

113. N. Guo, K. W. Cheung, H. T. Wong, and D. Ho, CMOS time-resolved, contact, and multispectral fluorescence imaging for DNA molecular diagnostics. Sensors **14**(11), 20602–20619 (2014).

114. S. Bouccara, A. Fragola, E. Giovanelli, G. Sitbon, N. Lequeux, T. Pons, and V. Loriette, Time-gated cell imaging using long lifetime near-infrared-emitting quantum dots for autofluorescence rejection. J. Biomed. Opt. **19**(5), 051208 (2014).

115. Ju Qiang, Liu Yongsheng, Tu Datao, Zhu Haomiao, Li Renfu, and Chen Xueyuan, Lanthanide-doped multicolor GdF3 nanocrystals for time-resolved photoluminescent biodetection. Chem. Eur. J. **17**(31), 8549–8554 (2011).

116. H. Kim, E. Petryayeva, and W. R. Algar, Enhancement of quantum dot Forster resonance energy transfer within paper matrices and application to proteolytic assays. IEEE J. Sel. Top. Quantum Electron. **20**(3), 141–151 (2014).

117. A. S. Paterson, B. Raja, V. Mandadi, B. Townsend, M. Lee, A. Buell, B. Vu, J. Brgoch, and R. C. Willson, A low-cost smartphone-based platform for highly sensitive point-of-care testing with persistent luminescent phosphors. Lab Chip **17**(6), 1051–1059 (2017).

118. K. G. Shah and P. Yager, Wavelengths and lifetimes of paper autofluorescence: a simple substrate screening process to enhance the sensitivity of fluorescence-based assays in paper. Anal. Chem. **89**(22), 12023–12029 (2017).

119. F. Zhou, M. O. Noor, and U. J. Krull, Luminescence resonance energy transfer-based nucleic acid hybridization assay on cellulose paper with upconverting phosphor as donors. Anal. Chem. **86**(5), 2719–2726 (2014).

120. C. R. Ispas, G. Crivat, and S. Andreescu, Review: recent developments in enzyme-based biosensors for biomedical analysis. Anal. Lett. **45**(2), 168–186 (2012).

121. M. He and Z. Liu, Paper-based microfluidic device with upconversion fluorescence assay. Anal. Chem. **85**(24), 11691–11694 (2013).

122. L. Wang, R. Yan, Z. Huo, L. Wang, J. Zeng, J. Bao, X. Wang, Q. Peng, and Y. Li, Fluorescence resonant energy transfer biosensor based on upconversion-luminescent nanoparticles. Angew. Chem. Int. Ed. **44**(37), 6054–6057 (2005).

123. W. W. Yu and I. M. White, Inkjet-printed paper-based SERS dipsticks and swabs for trace chemical detection. Analyst **138**(4), 1020–1025 (2013).

124. Ju Qiang, Uddayasankar Uvaraj, and Krull Ulrich, Paper-based DNA detection using lanthanide-doped LiYF4 upconversion nanocrystals as bioprobe. Small **10**(19), 3912–3917 (2014).

125. S. Doughan, U. Uddayasankar, and U. J. Krull, A paper-based resonance energy transfer nucleic acid hybridization assay using upconversion nanoparticles as donors and quantum dots as acceptors. Anal. Chim. Acta **878**, 1–8 (2015).

APPENDIX A

INTERFACIAL EFFECT-BASED QUANTIFICATION OF DROPLET ISOTHERMAL NUCLEIC ACID AMPLIFICATION FOR BACTERIAL INFECTION

Tiffany-Heather Ulep, Alexander S. Day, Katelyn Sosnowski, Alexa Shumaker and Jeong-Yeol Yoon

Department of Biomedical Engineering, The University of Arizona, Tucson, Arizona 85721, United States

Correspondence and requests for materials should be addressed to J.-Y.Y. (email: jyyoon@email.arizona.edu)

Received: 5 April 2019; Accepted: 17 June 2019; Published online: 03 July 2019;

doi:10.1038/s41598-019-46028-8

Published in Scientific Reports (2019) 9:9629

Abstract

Background. Bacterial infection is a widespread problem in humans that can potentially lead to hospitalization and morbidity. The largest obstacle for physicians/clinicians is the time delay in accurately identifying infectious bacteria, especially their sub-species, in order to adequately treat and diagnose such infected patients. Loop-mediated amplification (LAMP) is a nucleic acid amplification method that has been widely used in diagnostic applications due to its simplicity of constant temperature, use of up to 4 to 6 primers (rendering it highly specific), and capability of amplifying low copies of target sequences. Use of interfacial effect-based monitoring is expected to dramatically shorten the time-to-results of nucleic acid amplification techniques. In this work, we developed a LAMP-based point-of-care platform for detection of bacterial infection, utilizing smartphone measurement of contact angle from oil-immersed droplet LAMP reactions. Whole bacteria (*Escherichia coli* O157:H7) were assayed in buffer as well as 5% diluted human whole blood.

Results. Monitoring of droplet LAMP reactions was demonstrated in a three-compartment, isothermal proportional-integrated-derived (PID)-controlled chip. Smartphone-captured images of droplet LAMP reactions, and their contact angles, were evaluated. Contact angle decreased substantially upon target amplification in both buffer and whole blood samples. In comparison, no-target control (NTC) droplets remained stable throughout the 30 min isothermal reactions. These results were explained by the pre-adsorption of plasma proteins to an oil-water interface (lowering contact angle), followed by time-dependent amplicon formation and their preferential adsorption to the plasma protein-occupied oil-water interface.

Conclusion. Time-to-results was as fast as 5 min, allowing physicians to quickly make their decision for infected patients. The developed assay demonstrated quantification of bacteria concentration, with a limit-of-detection at 10^2 CFU/μL for buffer samples, and binary target or no-target identification with a limit-of-detection at 10 CFU/μL for 5% diluted whole blood samples.

Introduction

Bacterial infection is a widespread and common problem that can lead to various complications in humans. Specifically, the existence of antibiotic resistant bacteria[1] can lead to additional complications, including hospitalization and mortality. These bacteria include *Staphylococcus aureus* and *Escherichia coli* (specifically Shiga-toxin producing type such as O157:H7).[2] Diagnosis of such bacterial infection have traditionally been made based on the patient's symptoms, followed by broad-spectrum antibiotic treatments[3], which have shown positive results in decreasing mortality rates. However, efforts to conduct such diagnoses in a specific and sensitive manner are in high demand. Most importantly, there exist a strong need for identifying antibiotic and drug resistant microbes, monitoring the spread of epidemic to pandemic infectious diseases, and addressing sociopolitical infrastructure disparities[4].

The largest obstacle for physician/clinicians is the time delay in accurately identifying infectious pathogenic bacteria (especially their sub-species) in order to adequately treat the infected patients. Early detection and subsequent adequate treatment are highly correlated to decreased mortality and hospitalization[5-7]. The current gold standard is bacterial identification through culture-enrichment processes from patient's specimens (urine, nasal swab, throat swab, blood, serum, tissue biopsy, etc.). Typically, laboratories are equipped with automated culturing

systems, where growth curves in enriched media are monitored via carbon dioxide levels, fluorescence, or colorimetric photometry. The greatest disadvantage to such conventional methods of bacterial identification is their inherently long processing time of about 12 to 72 h. Such delays to pathogen identification have been a key obstacle in the early diagnosis and administration of treatment for infected patients. Other pitfalls to bacterial cultures for pathogen identification are the requirement of specialized equipment, personnel, and facilities[5,8].

Recent attempts to decrease time-to-results for bacterial identification include the integration of molecular diagnostic techniques such as hybridization [i.e. fluorescent *in situ* hybridization (FISH)], nucleic acid amplification [i.e. broad range and multiplexed polymerase chain reaction (PCR)], mass spectroscopy [i.e. matrix-assisted laser desorption/ionization time-of-flight mass spectrometry (MALDI-TOF MS)], and protein analysis[9]. By using such molecular techniques, the time-to-results is expedited since blood samples can be directly analyzed, bypassing the culture-enrichment process. PCR techniques have been more broadly applied in blood borne pathogen detection. However, PCR has been notoriously known for its susceptibility to false negatives due to the overwhelming background human DNA present in whole blood samples. Other components in the specimen such as ions and proteins can also inhibit the amplification mechanism[8,10]. More importantly, PCR requires three set temperatures (denaturation, annealing, and extension) that are alternated for ~30 cycles. This necessitates a thermal cycler, which is not appropriate for point-of-care (POC) diagnostics.

Isothermal nucleic acid amplification technologies have emerged as an alternative to PCR techniques, where the amplicons are exponentially produced at a constant temperature[11]. Isothermal techniques have been popularly applied in POC systems due to the requirement of only one temperature and the rapid amplification results (as fast as 20 min), making them attractive for use in field and clinical settings. A specific isothermal method that has gained

much reprise, and is even available in commercial kits for identification of pathogens, is loop-mediated isothermal amplification (LAMP). The reaction utilizes 4 to 6 primers, rendering it highly specific and capable of amplifying low initial copies of target sequence in a sample. LAMP amplicons are produced by cycling strand displacements and are dumbbell or cauliflower shaped[12,13].

In the past decade, 146 total publications have been identified using LAMP as a molecular diagnostic technique in POC platforms (Web of Science, using the keywords "loop-mediated amplification," "diagnosis," and "point-of-care"). Various detection methods were used with these POC LAMP platforms for confirmation and monitoring of target amplification, including electrochemical[14,15], fluorescent[16,17], colorimetric[18-20], and turbidimetric (due to magnesium pyrophosphate precipitation)[21,22] detection. While these detection methods have been used for demonstrating LAMP in POC platforms, they are susceptible to many different experimental and/or environmental conditions, such as ambient lighting, contaminants in samples, etc. They also require rather complicated equipment, such as spectrophotometers, optical filter(s), diffraction gratings, and/or noise filtration circuits.

An alternative detection method is interfacial tension measurement, where droplet height or shape is measured as an indicator of amplification. In fact, interfacial tension has been measured occasionally for droplet or digital PCR (dPCR), to assure droplets (microreactors) are reproducibly formed and maintained with consistent shape and surface energy, especially for high-throughput screening procedures[23-25]. Similarly, due to increased interest in POC applications, digital LAMP (dLAMP) platforms have been developed[26-28]. However, none of these studies have actively utilized interfacial tension as a sensing mechanism for the amplification of target genes[29,30]. It is possible to relate this interfacial tension to molecular self-

assembly at the interface (e.g. water-oil) and protein adsorption/kinetics towards the interface[31-35], and eventually to the quantification of amplified products.

In this work, a LAMP-based POC platform is proposed for identifying bacterial infection. It monitors the changes in interfacial tension, as represented by change in contact angle, of an oil-immersed droplet that contains LAMP reaction mixture, utilizing smartphone-based image processing. Whole bacteria (*Escherichia coli* O157:H7 with *Staphylococcus aureus* as cross-reference) are assayed. Experiments were repeated with diluted human whole blood as a model for human specimen. Specifically, target genes associated with antibiotic resistance are amplified: *rfbE* gene in *E. coli* and *spA* gene in *S. aureus*. Contact angle measurements are conducted for the LAMP droplets with and without target presence sitting on a proportional-integral-derivative (PID)-controlled heater within a disposable polydimethylsiloxane (PDMS)-based platform. An assay time of < 15 min or as fast as 5-10 min is desired, in order to not delay the physician's decision time in infected patients. Low limit of detection (LOD) is also preferred, e.g., as low as 10 CFU/μL sample.

Methods

Bacterial samples. *Escherichia coli* O157:H7 (part #0801622; ZeptoMetrix) and methicillin-sensitive *Staphylococcus aureus* (MSSA; part #0801675; ZeptoMetrix Corp., Buffalo, NY, USA) samples were cultured in lysogeny broth (LB) Miller's formula (Molecular Biological International Inc., Irvine, CA, USA) at 37°C for 8 hours. 1 mL of final concentrated bacterial stocks (10^5 CFU/μL) were centrifuged at 5.6 *g* for 10 min and resuspended in 1 mL of nuclease-free water. Stock bacterial samples were then serially diluted from 10^8 CFU/mL (= 10^5 CFU/μL) stock to 10^2 CFU/mL (= 0.1 CFU/μL) in nuclease-free water.

LAMP reaction mixture. LAMP primers were purchased from Sigma-Aldrich (St. Louis, MO, USA) following literature[36,37]. 10X target-specific primer sets as shown in Table 1 were formulated to contain 16 μM each of FIP and BIP primers, 8 μM each of Loop-F and Loop-B primers, and 2 μM of F3 and B3 primers. OmniAmp™ RNA and DNA LAMP Kit (Lucigen Corp., Middleton, WI, USA) was used. Final mixtures were comprised of 1X reaction buffer, 8 mM $MgSO_4$, 150 mM betaine, 0.5X primers, 3X OmniAmp polymerase, 8 mM dNTPs (25 mM each), 1 μL of target bacteria solution, and 0.01% w/v Span® 80 (S6760; Sigma). LAMP reactions were prepared on ice. Samples were amplified conventionally in a PCR tube with mineral oil (M5904; Sigma) to avoid evaporation from heat produced. Thermocycler (MJ Research, Waltham, MA, USA) was programmed at 69°C for 30 min, followed by refrigeration at 4°C. For reactions containing whole blood, 50% v/v of nuclease free water in 1 μL target bacteria solution was replaced with 5% v/v whole blood diluted in Plasma-Lyte A (pH 7.4; Baxter, Deerfield, IL, USA). Whole blood was stored refrigerated in a VACUETTE® Blood Collection Tube with 9NC coagulation sodium citrate 3.2% w/v (454334; Greiner Bio-One International, Monroe, NC, USA).

Gel electrophoresis. LAMP products were analyzed using gel electrophoresis. 1% w/v agarose gel (A0169; Sigma) in 1X tris-acetate-EDTA (TAE) buffer (35100131; Quality Biological Inc., Gaithersburg, MD, USA) was prepared and placed at 120 V for 50 min with an electrophoresis power supply (FB200; Fischer Scientific, Inc., Pittsburgh, PA, USA). TrackIt™ 100 bp DNA ladder (10488058; Invitrogen, Waltham, MA, USA) was used as a standard for fragment sizing. Gels were stained with ethidium bromide (E1510; Sigma) and imaged under UV light. Gel images were analyzed using ImageJ software (U.S. National Institutes of Health).

PDMS chip fabrication. Custom acrylonitrile butadiene styrene (ABS) resin mold was 3D-printed using MakerBot Replicator Z18 (MakerBot Industries, Brooklyn, NY, USA) resulting in a box shape of 0.5 mm x 0.5 mm x 1 mm, to create a chamber for conducting droplet-based LAMP reaction. This mold was then adhered to a two-compartment polystyrene Petri dish (99 mm x 15 mm; AB1471; Flinn Scientific, Batavia, IL, USA), resulting in the chip template (one-chamber version depicted in Figure 2 and two-chamber version depicted in Figure 5). Molds were carefully aligned to be parallel to partition for transparent optical window. Sylgard® 184 Silicone Elastomer Clear (4019862; Dow Corning, Midland, MI, USA) polydimethylsiloxane (PDMS) base and curing agent were combined at a 10:1 ratio and poured into chip template salinized by tridecafluoro-1,1,2,2-tetrahydroocyl trichlorosilane (78560-45-9; Gelest Inc., Morrisville, PA, USA). Cured PDMS replica was separated from the chip template and bonded to a microscope glass slide.

Contact angle monitoring with smartphone. Prior to loading LAMP droplet reactions, mineral oil and PDMS chip was pre-heated for 10 min in order to assure a constant 69°C temperature. Temperature ramping profile is shown in Supplementary Figure S1. Through the transparent optical window of the PDMS platform, real-time detection of LAMP amplification was achieved by monitoring the angle tangential to the droplet with respect to the glass surface, during constant applied heat. Images were captured every 30 s for 30 min using the Lapse It application (Interactive Universe, USA) and a smartphone camera (Samsung Galaxy S8, Suwon, South Korea). All images were loaded to ImageJ software and the contact angle was measured by ellipse-fit using the Contact Angle plugin. The absolute change in contact angle was determined with respect to contact angles measured at 30 min, 15 min, 10 min, and 5 min. This procedure was done in triplicates for *E. coli* O157:H7 target amplification varying concentrations of 10^5,

10^3, 10^2, 10, and 0 (NTC) CFU/μL. An unpaired two-tailed t-test compared the changes in droplet height with vs. without target presence (NTC) and cross-reactive samples. Error bars represent standard error ($n > 3$).

Design and fabrication of the portable device. The smartphone holder, heated chip stage, and temperature controller housing were designed using SolidWorks software (Dassault Systèmes, SolidWorks Corporation, Waltham, MA, USA) and 3D-printed using a Makerbot Replicator Z18 from acrylonitrile butadiene styrene (ABS) material. The heated chip stage consists of a thermoelectric heat pump (TEC1-12706, Hebei Int. Trading Co., Ltd., Shanghai, China) and the PDMS platform bound to the microscope glass slide. The heated chip stage is adjustable to the length of a microscope slide to allow optimum positioning of the droplet to the smartphone camera. The temperature controller housing consists of a proportional-integral-derivative (PID) controller (JLD612DC, LightObject, Sacramento, CA, USA) and a 36-guage type K thermocouple (5TC-TT-K-36-36, Omega Engineering, Norwalk, CT, USA) supported by a thermocouple holder that is adjustable perpendicular to the length of a microscope slide. This allowed positioning of a thermocouple into a reference water droplet. The PID controller is powered by a 3 V DC power supply, and continuously monitors the temperature within the reference water droplet. The reference temperature is used to regulate electrical output to a temperature control circuit[38] which includes a relay (G5SB, Omron Electronic Components, Kyoto, Japan). When the relay is switched to the "on" position, it allows the thermoelectric heat pump to be powered by a 9 V DC power supply. The PID controller was calibrated and programmed to sustain a constant temperature of 69°C. All compartments of the PDMS chip were filled with mineral oil and heated to steady state temperature before loading the 10 μL LAMP reaction mixture and reference NTC droplet.

Results

Conventional LAMP and gel electrophoresis detection. Six 10 µL LAMP reaction mixtures with 1 µL, 10^5 CFU/µL *E. coli* O157:H7 and six 10 µL no target controls (NTC) were prepared as a single experiment set. Identical experiments were also performed with 1 µL, 10^5 CFU/µL *S. aureus (*MSSA) and NTCs. For each experiment set, the LAMP reaction mixtures were conventionally amplified for 5, 10, 15, 20, 25, and 30 min (Figure A-1A). Once incubated for a set period of time, reaction mixtures were placed on ice, then put through gel electrophoresis. Verified gel of each reaction (0 to 30 min) for target (Figure A-1B) was then completed to determine successful or non-successful amplification. Amplification was detected at 30 min for both targets.

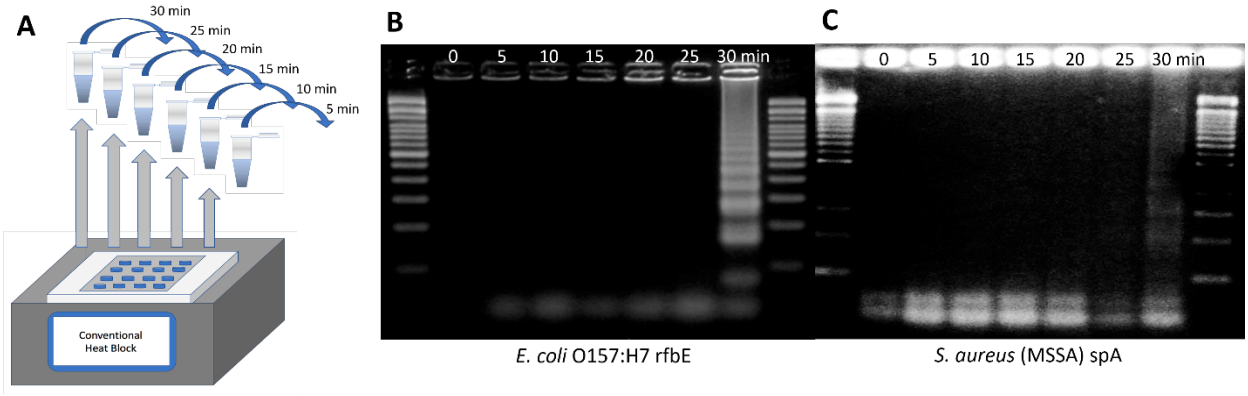

Figure A-1. (A) Schematic illustration of sequential incubation of 10 µL LAMP reaction mixtures with target *E. coli* O157:H7 (10^5 CFU/µL) or *S. aureus* (MSSA; 10^5 CFU/µL) and NTC reactions on conventional heat block for 5, 10, 15, 20, 25, and 30 min. (B-C) Sensitivity of conventional heat block and gel electrophoresis of LAMP reaction for the detection of *E. coli* O157:H7 rfbE gene and *S. aureus* (MSSA) spA gene. Amplifications were identified at 30 min for both targets.

Table 1. Sequences of oligonucleotide primers used

Target	Primer	Sequence (5'-3')	Size (bp)
E. coli O157:H7 *rfbE* gene	F3	AACAGTCTTGTACAAGTCCA	20
	B3	GGTGCTTTTGATATTTTTCCG	21
	FIP	CTCTCTTTCCTCTGCGGTCCGATGTTTTCACACTTATTGGAT	43
	BIP	TAAGGAATCACCTTGCAGATAAACTAGTACATTGGCATCGTGT	43
	LoopF	CCAGAGTTAAGATTGAT	17
	LoopB	CGAAACAAGGCCAGTTTTTTACC	23
S. aureus MSSA *spA* gene (Protein A)	F3	AATGACTCTCAAGCTCCAA	19
	B3	CTTTGTTGAAATTGTTGTCAGC	22
	FIP	GCTCTTCGTTTAAGTTAGGCATGTT-TGCGCAACAAAATAAGTTCA	45
	BIP	AAGTCTTAAAGACGATCCAAGCC-TTCGGTGCTTGAGATTCG	41
	LoopB	AGCACTAACGTTTTAGGTGAAGC	23

Contact angle changes during LAMP. To indirectly measure the interfacial effects of the LAMP reaction, droplets were placed in a PDMS chip filled with mineral oil where contact angle changes were measured, as depicted in Figure 2. 10 μL LAMP reaction mixtures were prepared with 1 μL of 10^5 or 0 (NTC) CFU/μL *E. coli* O157:H7 bacteria target or 1 μL of *S. aureus* (MSSA) cross-reactive sample where designated *E. coli* O157:H7 primer set was used. As shown in Supplementary Figure S2, target bacteria *E. coli* had greater change in contact angle in

comparison to the cross-reactive target *S. aureus* (the primers were designed to target *E. coli* O157:H7 but not *S. aureus*) and NTC sample throughout the 30 min reaction.

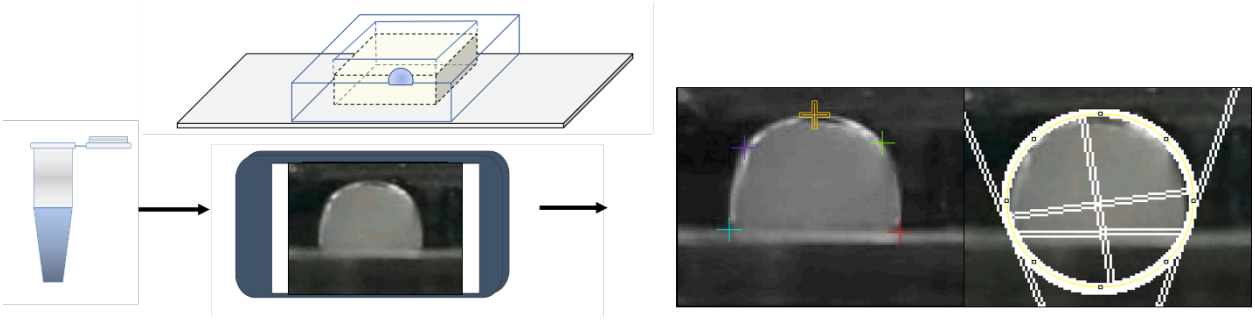

Figure A-2. Schematic of real-time monitoring of contact angle during droplet LAMP reaction in a PDMS well (single chamber version), followed by contact angle measurement via ImageJ and Contact Angle plugin. Ellipse-fit was used.

Sensitivity analysis in a buffer sample. *E. coli* bacteria solutions were serially diluted from 10^5 to 10 CFU/µL (excluding 10^4 CFU/µL), which were used as target samples utilizing previously stated LAMP droplet mixtures in a PDMS chamber filled with mineral oil. Images of droplets were captured every 30 s to monitor change in contact angle throughout the 30 min reaction. In Figure 3 the calculated change in contact angle ($\Delta\theta = \theta_{initial} - \theta$) at 30, 15, 10, and 5 min is shown in relation to the concentration of bacteria. Starting at 5 min (Figure 3C), change in contact angle shows a fairly moderate R^2 value of 0.826 when fitted to a logarithmic regression. This included bacteria concentrations of 0 (NTC), 10, 10^2, and 10^3 CFU/µL ranging from contact angle change of –0.74° to 5.1°. After 10 and 15 min (Figure 3B and 3C) excluding 10^5 CFU/µL concentration, R^2 values were 0.593 and 0.751 respectively when fitted to a logarithmic regression, displaying inferior proportionality between Δθ and log bacteria concentration. Δθ ranged from 1.07° to 7.75° at 10 min, and from 1.91° to 8.88° at 15 min. At 30 min (Figure 3A) a fairly good R^2 value of 0.882 was reported in correspondence to a logarithmic regression, which included all bacteria

concentrations from 0 to 10^5 CFU/µL. Overall, the shortest time-to-result for significant detection was observed for 10^3 CFU/µL bacteria concentration, with a detection time as soon as the first 5 min of the reaction. At 30 min, statistical difference between target and NTC was seen for all concentrations higher than or equal to 10^2 CFU/µL, which is the limit of detection (LOD) of this assay.

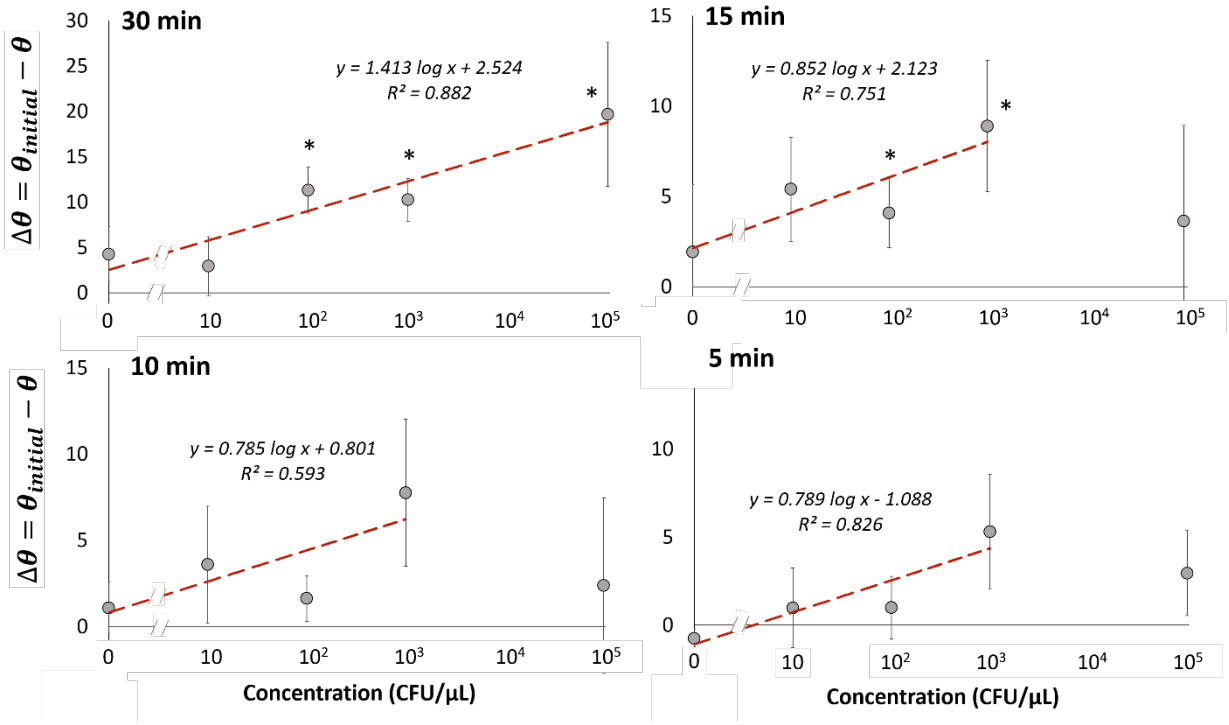

Figure A-3. Change in contact angle ($\Delta\theta = \theta_{initial} - \theta$) for varying *E. coli* concentrations from 0 to 10^5 CFU/µL measured at 30 min, 15 min, 10 min, and 5 min. Averages of three different experiments. Error bars represent standard errors. * indicates substantial changes from the initial contact angles with 95% confidence.

Sensitivity analysis in a blood sample. In this model, *E. coli* bacteria was serially diluted in 5% whole blood from 10^3 to 10 CFU/µL and used as the 1 µL target volume for the LAMP reaction. As each blood sample was different from each other, the resulting contact angle also varied from

sample-to-sample. Therefore, it became necessary to monitor the contact angles of target and NTC simultaneously and normalize the target's contact angle with that of NTC. To this end, a PID-controlled prototype was designed and assembled to run a contact angle change analysis in a custom-made, two chamber version PDMS chip as shown in Figure 4. Again, images were taken every 30 s throughout the 30 min LAMP reaction and used to measure contact angle. Prior to calculating change in contact angle, all angles were normalized to those of NTC droplets: $\Delta\theta/\theta_{NTC} = \theta_{initial}/\theta_{NTC,initial} - \theta/\theta_{NTC}$, where positive $\Delta\theta/\theta_{NTC}$ correlates to decrease in θ/θ_{NTC}. This was done to take into account the interfacial effects caused by the fast oil-water diffusion and adsorption of blood proteins to the oil-water interface. As shown in Supplementary Figure S3, all bacteria concentration showed a change in θ/θ_{NTC} at each time interval between 5 and 30 min. At 5 min, 10 and 10^3 CFU/μL show statistical difference compared to NTC with $\Delta\theta/\theta_{NTC}$ of 0.085 and 0.023 respectively (Figure 5D). At 10 min, all bacteria concentrations from 10 to 10^3 CFU/μL showed statistical difference to NTC with $\Delta\theta/\theta_{NTC}$ of 0.10, 0.11, and 0.088 respectively (Figure 5C). Similar to 10 min, 15 min showed statistical difference compared to NTC for all bacteria concentrations with $\Delta\theta/\theta_{NTC}$ ranging from 0.058 to 0.049 (Figure 5B). At 30 min, $\Delta\theta/\theta_{NTC}$ ranged from 0.10 to 0.049 for all bacteria concentrations (Figure 5A). The overall trends observed showed a binary logistic, where when target bacteria was present, $\Delta\theta/\theta_{NTC}$ was observed with significant detection as soon as 5 min for 10 CFU/μL and for all bacteria concentrations at 10 min.

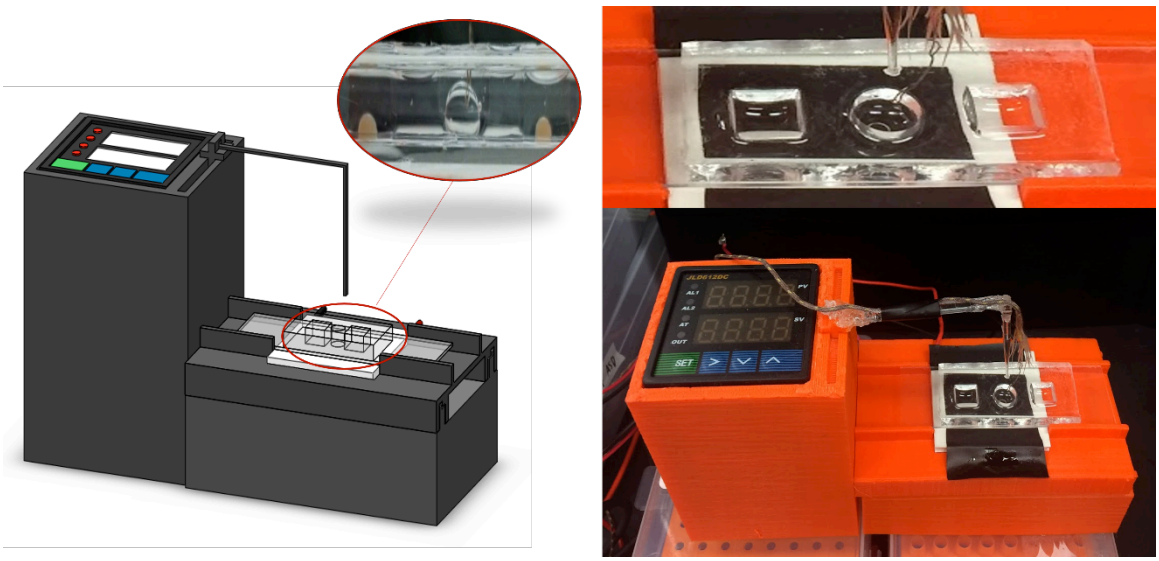

Figure A-4. Fully-integrated, all-in-one PID-controlled device for real-time monitoring of contact angle during droplet LAMP reaction in a PDMS-based, two-chamber version chip, for side-by-side comparison of target and NTC droplets.

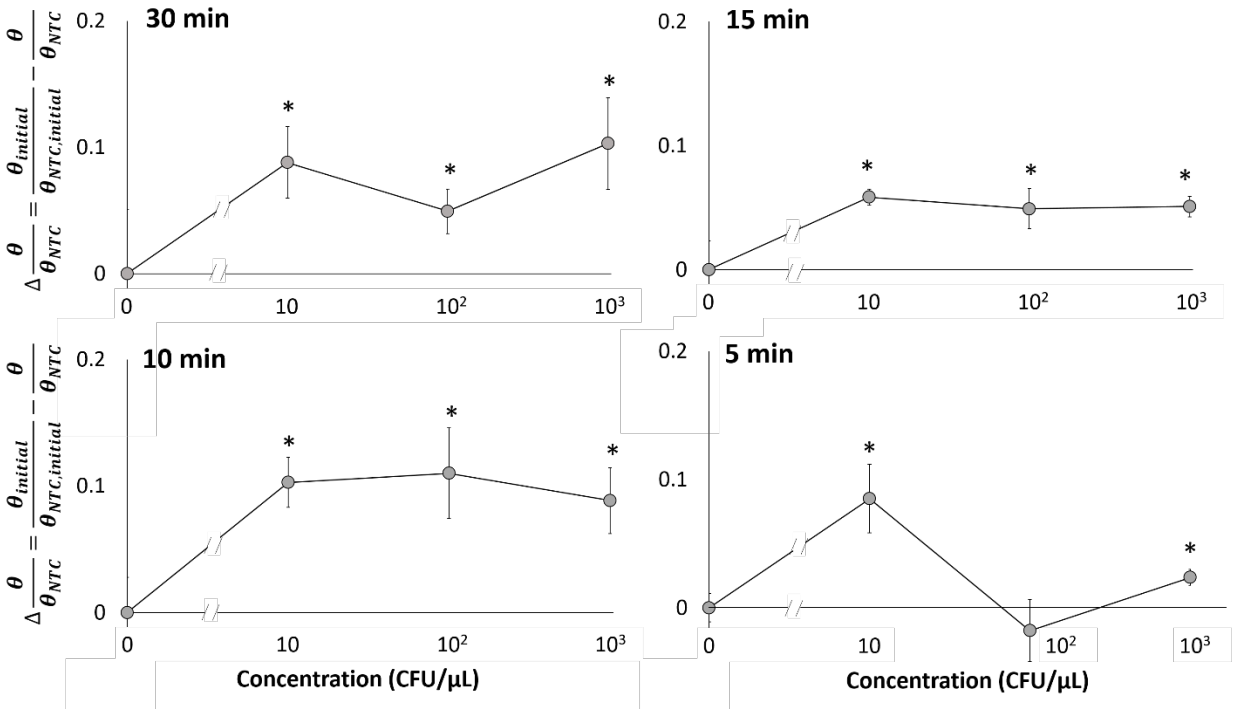

Figure A-5. Normalized change in contact angle ($\Delta\theta/\theta_{NTC} = \theta_{initial}/\theta_{NTC,initial} - \theta/\theta_{NTC}$) with varying concentrations from 0 to 10^3 CFU/µL in 5% whole blood at 30 min, 15 min, 10 min, and

5 min. Averages of three different experiments. Error bars represent standard errors. * indicates substantial changes from the initial contact angles with 95% confidence.

Discussion

Advantages of droplet LAMP. The proposed method and device are well-suited for portable and low-cost nucleic acid-based identification of bacterial infection, which is also demonstrated in complex sample matrices. In comparison to other nucleic acid amplification devices[39-41], the developed platform requires neither moving parts nor liquid flow. Within the droplet LAMP device, samples and thermocouple components are stationary within their respective reservoirs, which reduces the risk for contamination and other factors that can contribute to false assay results. Additionally, the contact angle measurement of a droplet is less susceptible to external forces and vibrations. Interfacial tension has most commonly been measured via pendant droplet analysis, which is quite vulnerable to external vibration and gas entrapments within the needle tip; furthermore, it is difficult to deliver uniform heat to the droplet itself due to the presence of a needle.

The proposed method occurs at an isothermal temperature. Comparatively, PCR-based point-of-care devices require large temperature gradients: 94°C for denaturation, 72°C for extension, and 50-65°C for annealing. Such broad temperature ranges must also be timed precisely to prevent undesirable, non-specific annealing and extension[42,43], requiring close supervision. As mentioned previously, the droplet LAMP device has an integrated PID controller, automatic image capturing, and analysis system. Such integration allows for minimal supervision during reaction period and fast contact angle analysis, allowing successful identification of target bacterial presence.

Challenges in reproducibility. Challenges in droplet LAMP with regards to reproducibility lie greatly within the variations between assays. An example of a condition that is varied each run is the methodology in which the sample is applied into the chip wells. Aqueous droplet LAMP reagent is manually extruded from a blunt end needle tip and placed into the well till gravity drops the solution onto the bottom surface. The speed, height, and forces controlled by the user is varied between each assay and should be mitigated in the next version of the platform. An automated droplet mechanism such as a microfluidic chip or automated pipette could be added to control droplet formation and application into chip wells. Incorporation of such techniques will help to reduce errors in the device.

Another variation introduced throughout these experiments is the sample composition itself. Blood samples are pooled healthy donor blood that have been diluted to 5 v/v%. In clinical settings, this sample matrix is not synonymous. The pooled blood was used to showcase an "average" representative sample with numerous variable introduced. With these parameters considered, statistical significance was still achieved in comparison to no-target-control samples, thus demonstrating promising robustness. However, the assay will still need to be demonstrated with extensive trials performed with non-pooled single donor blood to demonstrate statistical power and clinical relevance as future work. It is important to increase the number of assays done with different sample types to characterize repeatability. Up until now, reproducibility was characterized as indicated by standard error bars in graphs.

Assay performance. The change in contact angle of LAMP droplets without blood (buffer system) had a logarithmic regression fitted to the bacteria concentration at 30, 15, 10, and 5 min. Relatively good R^2 values were found at 5 min from 1 to 10^3 CFU/μL and at 30 min from 1 to

10^5 CFU/μL. A significant difference was determined in as soon as 5 min for the buffer system with 10^3 CFU/μL bacteria concentration, which was the limit of detection (LOD) at 5 min. LOD was reduced to 10^2 CFU/μL at 15 min and at 30 min. The contact angle analysis of LAMP reactions in a blood sample was determined to be a binary assay, i.e., target or no target presence. This was demonstrated in as fast as the first 5 min of reaction for 10 CFU/μL (LOD). A significant difference was identified for all concentrations tested, from 10 to 10^3 CFU/μL as early as 10 min. Given the small sample volume of 1 μL, the LOD of 10 CFU/μL is close to the lowest possible level of detection, despite the presence of whole blood components. The LODs of many commercial rapid kits for bacterial infection are typically in the range of 10^5 – 10^6 CFU/mL (= 10^2 – 10^3 CFU/μL), which have frequently been used to identify urinary tract infection (UTI) from urine[44], gonorrhea from urine[44], and Streptococcus from throat swab[45]. Typical concentrations of commensal bacteria on human skin can be as high as 10^5 CFU/cm^2, and they increase to 10^7 – 10^8 CFU/cm^2 with symptomatic skin and would infections[46]. Overall, the prototype device demonstrated that the presence of bacteria could easily be identified by monitoring the change in contact angle for target and NTC droplets side-by-side, i.e., paired comparison. Compared to other conventional quantitative LAMP assays, our method showed much shorter assay times. Only a relatively small number of amplified molecules are necessary to diffuse towards the oil-water interface to alter the interfacial tension, and subsequently contact angle, thus making it a fast time-to-result assay.

Molecular diffusion and adsorption of LAMP amplicons to oil-water interface. As illustrated in Figure 6A, nucleic acid amplification occurs inside of the droplet, followed by the sequential adsorption of produced amplicons to the oil-water interface due to their (loop-shaped)

complex geometry, which compromises solvation in water. The movement of the amplicons, especially ones with higher molecular weights, is driven by molecular diffusion. Diffusion constants of nucleic acids have been well studied in relation to their size, due to the wide use of electrophoresis techniques for size separation. Models such as the Nernst/Stokes-Einstein equation, Zimm's theory, and Kratky-Porod equation have been widely applied[47,48] to simulate both translational and rotational diffusion of both small rod-like and polymeric chain nucleic acid structures ranging from 30 to 5000 base pairs (bp). Generally, such investigations concluded that the diffusion coefficient and overall velocity are inversely related to bp length. Products of isothermal loop-mediated amplification are large dumbbell-like structures with a wide range of bp lengths. Diffusion of such high molecular weight molecules is difficult and slow, especially when their concentration is very high (molecular crowding).

Both PCR and LAMP amplicons consist of double stranded DNA, which is partially hydrophilic due to its sugar-phosphate backbone[49]. Its interior is more hydrophobic allowing the backbone to be held together by van der Waals forces, leading to overall stability of the structure[50,51]. Therefore, amplicons' surfaces are less hydrophilic (or become relatively hydrophobic). Such amphiphilic character is more pronounced with LAMP amplicons due to their complex geometry, making them to be excluded in polar solvents and concentrated at the oil-water interface due to the hydrophobic effect. This is also similarly observed for another type of amphiphilic molecule: proteins[52].

To model amplicon diffusion within a LAMP droplet, a combined exponential growth and Fick's diffusion-based model was used varying initial *E. coli* bacteria concentration. The model takes into account the exponential production of amplicons and the corresponding diffusivity constant based on the amplicon's molecular weight. The model assumes a hemi-spherical droplet shape (as the initial contact angle is close to 90° in most cases) to determine the

maximum number of available spaces for amplicons at the oil-water interface (calculated by hydrodynamic radii[53,54]). The model varies the initial bacteria target concentration (C_0, CFU/μL) to determine the interface concentration of amplicons (n, amplicons per cm^2) at the given time t. An amplicon length of 965 bp was used in the simulation in Figure 6A, where 965 bp is 5 times the length of target gene, 193 bp (rfbE gene from *E. coli*). Amplicon length of 1930 bp (10 times the target gene length) was also modeled (Supplementary Figure S4). Exponential growth constant (k, s^{-1}) and diffusivity constant (D, $cm^2\ s^{-1}$) of produced amplicons were chosen based on literature[55,56] (specific values used can be found in Supplementary Tables S1 and S2). Cumulatively, the model determines n with respect to time, t:

$$n(t) = 2C_0 e^{kt}\sqrt{\frac{Dt}{\pi}} \qquad (1)$$

Similarly, to explain and simulate the diffusion and adsorption of blood proteins (albumin, IgG, and fibrinogen[57]) in a blood sample, a Fick's diffusion equation was utilized.

$$n(t) = 2C_0\sqrt{\frac{Dt}{\pi}} \qquad (2)$$

Using the equations (1) and (2), the % fractions of surface area occupied by amplicons and blood proteins were determined using the amplicons' or blood proteins' hydrodynamic radii.

As illustrated in Figure 6A, LAMP droplets (buffer system) with target presence internally produce amplicons, which then diffuse and adsorb to the oil-water interface reducing interfacial tension, thus changing the droplet contact angle (Figure 3). It was also shown that greater contact angle change was observed with increasing initial bacteria concentration. In comparison, change in droplet contact angle remained relatively constant in the LAMP droplets with no target presence and with cross-reactive target. As shown in Figure 6B and Supplementary Figure S4, the slopes of all curves are quite steep, indicating rapid diffusion and adsorption of amplicons to the oil-water interface. The time for amplicon saturation is, therefore,

dictated primarily by the production rate of amplicons, which is a function of initial bacteria concentration. This allows the proposed method to quantify the initial bacteria concentration.

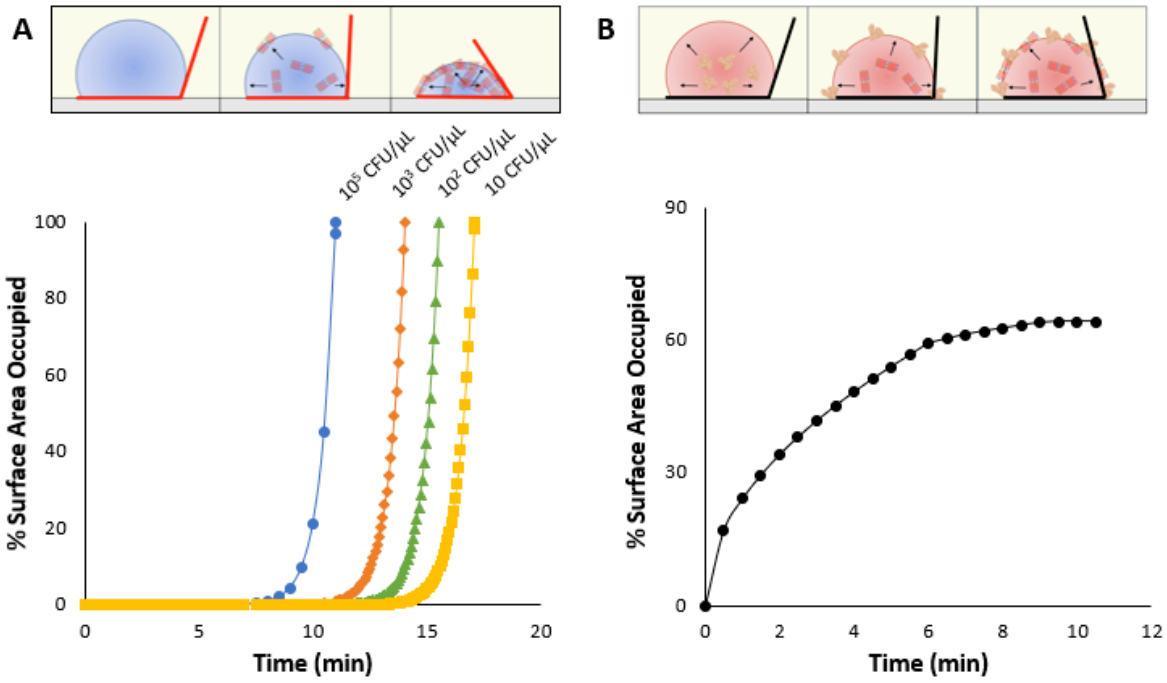

Figure A-6. (A) Illustration and simulation of % surface area occupied by the diffusion of 965-bp amplicon to the oil-water interface with doubling time of 28.1 s and growth constant k of 0.022 for initial bacteria concentrations from 10^5 to 10 CFU/µL in buffer system (without blood). (B) Illustration and simulation of % surface area occupied by the diffusion of blood protein species (albumin, IgG, and fibrinogen) to the oil-water interface, depicting slower interface occupation by blood proteins than those by amplicons while leaving substantial unoccupied area that can accommodate amplicons.

With blood present for the blood sample, the trend in contact angle change was binary, i.e., target or no target presence. In this model, both amplicons and blood proteins are competing for the available spaces at the oil-water interface. With NTC (= 0 CFU/µL, i.e. no amplicon

presence), the surface is occupied only by blood proteins, which is a relatively slow process that is unable to saturate the entire surface – it takes 7 min to reach maximum surface coverage of approximately 60% (Figure 6B). Proteins are unable to saturate the whole surface due to 1) spreading and flattening at the interface, 2) lateral repulsion between proteins with net positive or net negative charge, especially albumin[55], and 3) solvation of proteins that may interfere with additional protein adsorption. The remaining 40% of the interface is left for amplicons to arrive. However, there are not enough amplicons produced by this time (7 min) for the range of concentrations tested ($10 – 10^5$ CFU/μL) as shown in Figure 6A and Supplementary Figure S4. Therefore, amplicon adsorption is occurring after the surface is occupied with blood proteins. This delayed adsorption of the amplicons and competition with the blood proteins is illustrated in Figure 6B. While the additional amplicon adsorption did result in further contact angle change as shown in Figure 5, its competition with blood proteins rendered this method unable to quantify initial bacteria concentration in a blood sample. Despite this, the model successfully identified the presence of bacteria in as little as 5 min with as low as 10 CFU/μL initial concentration, which is a significant improvement compared to that in a buffer sample. In addition, the error bars are generally much smaller than those in a buffer sample, presumably due to the presence of blood proteins at the interface, most notably albumin, which can "passivate" the interface.

Conclusions

A droplet LAMP-based POC platform was designed and tested for detecting bacteria (*E. coli* O157:H7) from diluted (5%) whole blood samples, utilizing smartphone-based contact angle measurements. Monitoring of droplet contact angle was demonstrated in a disposable, two-chamber PDMS chip, incorporating a compact, PID temperature controller and a smartphone.

Analysis of droplet contact angle in a buffer sample showed decrease in contact angle with target presence, with log-linear quantifiable capabilities from 10 to 10^3 CFU/μL *E. coli* in as little as 5 min and from 10 to 10^5 CFU/μL by the end of the 30 min reaction. In comparison, NTC droplets (zero bacteria concentration) did not show significant change in contact angle throughout the 30 min isothermal reaction. Analysis of droplet contact angle in a blood sample (bacteria spiked into 5% diluted whole blood) showed, again, decrease in contact angle with target presence. However, no bacteria concentration-dependent relationships were distinguishable, rendering this method binary (i.e. target or no target) in a blood sample. Binary results were determined in as little as 5 min for 10 and 10^3 CFU/μL *E. coli* and in 10 min for all concentration tested (10 to 10^3 CFU/μL). Thus, we have demonstrated an assay time of 5-10 min, sufficiently fast for physicians to make clinical decisions, with low limit of detection as low as 10 CFU/μL sample.

Molecular diffusion and interfacial adsorption models were developed for blood proteins as well as exponentially produced amplicons. Due to the higher concentrations of blood proteins and smaller number of amplicons early in the assay, interfacial adsorption is initially dominated by blood proteins, which are later replaced by exponentially producing amplicons that compete with the blood proteins. While the assays with blood samples show only binary assay results, they are much more reproducible with smaller error bars, which is a unique advantage of this method. In other biosensing methods, whole blood generally compromises the assay reproducibility or sensitivity. This proposed method can be further investigated and applied in other complex biological matrices such as urine, saliva, other bodily fluids, feces, and soft tissues for fast (< 10 min) nucleic acid amplification.

Acknowledgements

The authors would like to thank Dr. Ariana M. Nicolini for her LAMP expertise and knowledge. Katelyn Sosnowski acknowledges W. L. Gore & Associates, Inc. for the undergraduate research fellowship. This work was supported by the Cardiovascular Biomedical Engineering Training Grant from U.S. National Institutes of Health (grant number T32HL007955).

References

1. Mayo Clinic. Symptoms and causes. Available at: https://www.mayoclinic.org/diseases-conditions/sepsis/symptoms-causes/syc-20351214?p=1. (Accessed: 12th May 2018)

2. U.S. Centers for Disease Control and Prevention (CDC). Basic Information - Sepsis. (2018). Available at: https://www.cdc.gov/sepsis/basic/index.html. (Accessed: 12th May 2018)

3. Calandra, T., Glauser, M. P., Schellekens, J. & Verhoef, J. Treatment of gram-negative septic shock with human IgG antibody to Escherichia coli J5: A prospective, double-blind, randomized trial. *J. Infect. Dis.* **158**, 312–319 (1988).

4. Yager, P., Domingo, G. J. & Gerdes, J. Point-of-care diagnostics for global health. *Annu. Rev. Biomed. Eng.* **10**, 107–144 (2008).

5. Liesenfeld, O., Lehman, L., Hunfeld, K.-P. & Kost, G. Molecular diagnosis of sepsis: New aspects and recent developments. *Eur. J. Microbiol. Immunol.* **4**, 1–25 (2014).

6. Josefson, P. *et al.* Evaluation of a commercial multiplex PCR test (SeptiFast) in the etiological diagnosis of community-onset bloodstream infections. *Eur. J. Clin. Microbiol. Infect. Dis.* **30**, 1127–1134 (2011).

7. Beekmann, S. E., Diekema, D. J., Chapin, K. C. & Doern, G. V. Effects of rapid detection of bloodstream infections on length of hospitalization and hospital charges. *J. Clin. Microbiol.* **41**, 3119–3125 (2003).

8. Puttaswamy, S., Lee, B. D. & Sengupta, S. Novel electrical method for early detection of viable bacteria in blood cultures. *J. Clin. Microbiol.* **49**, 2286–2289 (2011).

9. Venkatesh, M., Flores, A., Luna, R. A. & Versalovic, J. Molecular microbiological methods in the diagnosis of neonatal sepsis. *Expert Rev. Anti Infect. Ther.* **8**, 1037–1048 (2010).

10. Handschur, M., Karlic, H., Hertel, C., Pfeilstöcker, M. & Haslberger, A. G. Preanalytic removal of human DNA eliminates false signals in general 16S rDNA PCR monitoring of bacterial pathogens in blood. *Comp. Immunol. Microbiol. Infect. Dis.* **32**, 207–219 (2009).

11. Niemz, A., Ferguson, T. M. & Boyle, D. S. Point-of-care nucleic acid testing for infectious diseases. *Trends Biotechnol.* **29**, 240–250 (2011).

12. Mori, Y. & Notomi, T. Loop-mediated isothermal amplification (LAMP): a rapid, accurate, and cost-effective diagnostic method for infectious diseases. *J. Infect. Chemother.* **15**, 62–69 (2009).

13. Notomi, T. *et al.* Loop-mediated isothermal amplification of DNA. *Nucleic Acids Res.* **28**, e63–e63 (2000).

14. Hsieh, K., Patterson, A. S., Ferguson, B. S., Plaxco, K. W. & Soh, H. T. Rapid, sensitive, and quantitative detection of pathogenic DNA at the point of care through microfluidic

electrochemical quantitative loop-mediated isothermal amplification. *Angew. Chem. Int. Ed.* **51**, 4896–4900 (2012).

15. Safavieh, M., Ahmed, M. U., Tolba, M. & Zourob, M. Microfluidic electrochemical assay for rapid detection and quantification of Escherichia coli. *Biosens. Bioelectron.* **31**, 523–528 (2012).

16. Stedtfeld, R. D. *et al.* Gene-Z: a device for point of care genetic testing using a smartphone. *Lab Chip* **12**, 1454–1462 (2012).

17. Liu, C. *et al.* An isothermal amplification reactor with an integrated isolation membrane for point-of-care detection of infectious diseases. *Analyst* **136**, 2069–2076 (2011).

18. Priye, A. *et al.* A smartphone-based diagnostic platform for rapid detection of Zika, Chikungunya, and Dengue viruses. *Sci. Rep.* **7**, 44778 (2017).

19. Oh, S. J. *et al.* Fully automated and colorimetric foodborne pathogen detection on an integrated centrifugal microfluidic device. *Lab Chip* **16**, 1917–1926 (2016).

20. Sayad, A. *et al.* A microdevice for rapid, monoplex and colorimetric detection of foodborne pathogens using a centrifugal microfluidic platform. *Biosens. Bioelectron.* **100**, 96–104 (2018).

21. Wang, C.-H., Lien, K.-Y., Wu, J.-J. & Lee, G.-B. A magnetic bead-based assay for the rapid detection of methicillin-resistant Staphylococcus aureus by using a microfluidic system with integrated loop-mediated isothermal amplification. *Lab Chip* **11**, 1521–1531 (2011).

22. Polley, S. D. *et al.* Mitochondrial DNA targets increase sensitivity of malaria detection using loop-mediated isothermal amplification. *J. Clin. Microbiol.* **48**, 2866–2871 (2010).

23. Pandit, K. R., Rueger, P. E., Calabrese, R. V., Raghavan, S. R. & White, I. M. Assessment of surfactants for efficient droplet PCR in mineral oil using the pendant drop technique. *Colloids Surf. B* **126**, 489–495 (2015).

24. Schuler, F. *et al.* Centrifugal step emulsification applied for absolute quantification of nucleic acids by digital droplet RPA. *Lab Chip* **15**, 2759–2766 (2015).

25. Kim, J. & Song, S. On-chip high density droplet-on-template (DOT) array. *J. Micromech. Microeng.* **25**, 017001 (2015).

26. Gansen, A., Herrick, A. M., Dimov, I. K., Lee, L. P. & Chiu, D. T. Digital LAMP in a sample self-digitization (SD) chip. *Lab Chip* **12**, 2247–2254 (2012).

27. Zhu, Q. *et al.* Self-priming compartmentalization digital LAMP for point-of-care. *Lab Chip* **12**, 4755–4763 (2012).

28. Rane, T. D., Chen, L., Zec, H. C. & Wang, T.-H. Microfluidic continuous flow digital loop-mediated isothermal amplification (LAMP). *Lab Chip* **15**, 776–782 (2015).

29. Harshman, D. K., Rao, B. M., McLain, J. E., Watts, G. S. & Yoon, J.-Y. Innovative qPCR using interfacial effects to enable low threshold cycle detection and inhibition relief. *Sci Adv.* **1**, e1400061 (2015).

30. Nicolini, A. M. *et al.* Mie scatter and interfacial tension based real-time quantification of colloidal emulsion nucleic acid amplification. *Adv. Biosyst.* **1**, 1700098 (2017).

31. Beverung, C. J., Radke, C. J. & Blanch, H. W. Protein adsorption at the oil/water interface: characterization of adsorption kinetics by dynamic interfacial tension measurements. *Biophy. Chem.* **81**, 59–80 (1999).

32. Tanford, C. The hydrophobic effect and the organization of living matter. *Science* **200**, 1012–1018 (1978).

33. Goetz, R. & Lipowsky, R. Computer simulations of bilayer membranes: Self-assembly and interfacial tension. *J. Chem. Phys.* **108**, 7397–7409 (1998).

34. Graham, D. E. & Phillips, M. C. Proteins at liquid interfaces: I. Kinetics of adsorption and surface denaturation. *J. Colloid Interface Sci.* **70**, 403–414 (1979).

35. Schröder, V., Behrend, O. & Schubert, H. Effect of dynamic interfacial tension on the emulsification process using microporous, ceramic Membranes. *J. Colloid Interface Sci.* **202**, 334–340 (1998).

36. Misawa, Y. *et al.* Application of loop-mediated isothermal amplification technique to rapid and direct detection of methicillin-resistant Staphylococcus aureus (MRSA) in blood cultures. *J. Infect. Chemother.* **13**, 134–140 (2007).

37. Zhao, X. *et al.* Development and application of a loop-mediated isothermal amplification method on rapid detection Escherichia coli O157 strains from food samples. *Mol. Biol. Rep.* **37**, 2183–2188 (2010).

38. Yoon, J.-Y. *Introduction to biosensors: From electric circuits to immunosensors*. (Springer, 2016).

39. Harshman, D. K. *et al.* Enhanced nucleic acid amplification with blood in situ by wire-guided droplet manipulation (WDM). *Biosens. Bioelectron.* **53**, 167–174 (2014).

40. Yuen, P. K. *et al.* Microchip module for blood sample preparation and nucleic acid amplification reactions. *Genome Res.* **11**, 405–412 (2001).

41. Cho, Y.-K. *et al.* One-step pathogen specific DNA extraction from whole blood on a centrifugal microfluidic device. *Lab Chip* **2**, 565–573 (2007).

42. Erlich, H., Gelfand, D. & Sninsky, J. Recent advances in the polymerase chain reaction. *Science* **252**, 1643–1651 (1991).

43. Arnheim, N. & Erlich, H. Polymerase chain reaction strategy. *Annu. Rev. Biochem.* **61**, 131–156 (1992).

44. Cho, S., Park, T. S., Nahapetian, T. G. & Yoon, J.-Y. Smartphone-based, sensitive µPAD detection of urinary tract infection and gonorrhea. *Biosens. Bioelectron.* **74**, 601-611 (2015).

45. U.S. Food and Drug Administration (FDA). 510(k) substantial equivalence determination decision summary - assay and instrument combination template. 510(k) number K122718. Available at: https://www.accessdata.fda.gov/cdrh_docs/reviews/k122718.pdf. (Accessed: 1st June 2019)

46. Sweeney, R. E., Budiman, E. & Yoon, J.-Y. Mie scatter spectra-based device for instant, contact-free, and specific diagnosis of bacterial skin infection. *Sci. Rep.* **7**, 4801 (2017).

47. Nkodo, A. E. *et al.* Diffusion coefficient of DNA molecules during free solution electrophoresis. *Electrophoresis* **22**, 2424–2432 (2001).

48. Tinland, B., Pluen, A., Sturm, J. & Weill, G. Persistence length of single-stranded DNA. *Macromolecules* **30**, 5763–5765 (1997).

49. Saenger, W. *Principles of nucleic acid structure*. (Springer Science & Business Media, 2013).

50. Lodish, H. *et al.* Structure of nucleic acids. *Molecular Cell Biology. 4th edition* (W. H. Freeman & Co., 2000).

51. Bhattacharya, S. & Mandal, S. S. Interaction of surfactants with DNA. Role of hydrophobicity and surface charge on intercalation and DNA melting. *Biochim. Biophys. Acta Biomembr.* **1323**, 29–44 (1997).

52. Southall, N. T., Dill, K. A. & Haymet, A. D. J. A view of the hydrophobic effect. *J. Phys. Chem. B* **106**, 521–533 (2002).

53. ThermoFisher Scientific. DNA and RNA Molecular Weights and Conversions - US. Available at: https://www.thermofisher.com/us/en/home/references/ambion-tech-support/rna-tools-and-calculators/dna-and-rna-molecular-weights-and-conversions.html. (Accessed: 11th October 2018)

54. Erickson, H. P. Size and shape of protein molecules at the nanometer level determined by sedimentation, gel filtration, and electron microscopy. *Biol. Proced. Online* **11**, 32 (2009).

55. Kubota, R. & Jenkins, D. M. Real-time duplex applications of loop-mediated amplification (LAMP) by assimilating probes. *Int. J. Mol. Sci.* **16**, 4786–4799 (2015).

56. Lukacs, G. L. *et al.* Size-dependent DNA mobility in cytoplasm and nucleus. *J. Biol. Chem.* **275**, 1625–1629 (2000).

57. Dee, K. C., Puleo, D. A. & Bizios, R. *An introduction to tissue-biomaterial interactions*. (Wiley-Liss, 2002).

Supplementary

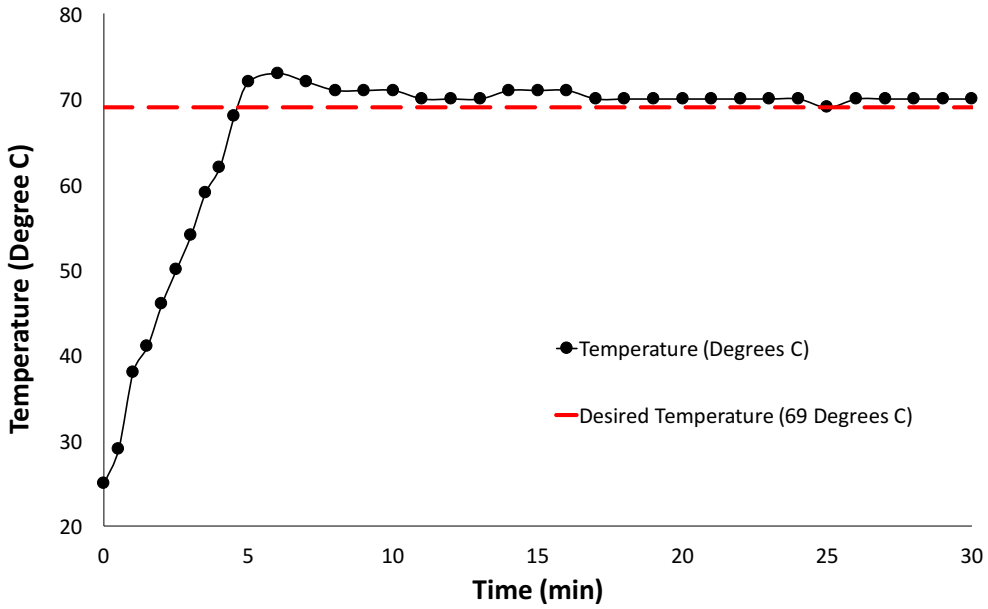

Supplementary Figure A-S1. PID Temperature controller temperature characterization with tuned parameters to ensure constant 69°C throughout 30 min LAMP reaction (P = 0.1%, I = 12 sec, and D = 28 sec).

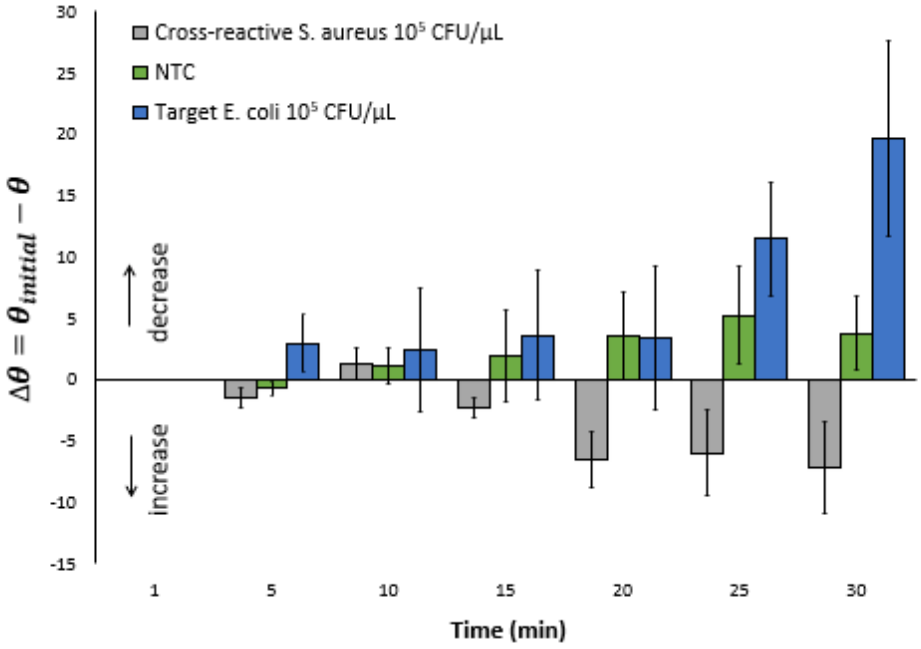

Supplementary Figure A-S2. Change in contact angle ($\Delta\theta = \theta_{initial} - \theta$) of droplet LAMP targeting *E. coli* O157:H7 10^5 CFU/µL, cross-reactive sample of *S. aureus* 10^5 CFU/µL, and NTC.

APPENDIX B

SMARTPHONE BASED ON-CHIP FLUORESCENCE IMAGING AND CAPILLARY FLOW VELOCITY MEASUREMENTS FOR DETECTING ROR1$^+$ CANCER CELLS FROM BUFFY COAT BLOOD SAMPLES ON DUAL-LAYER PAPER MICROFLUIDIC CHIP

Tiffany-Heather Ulep[1], Ryan Zenhausern[1], Alana Gonzales[1], David S. Knoff[1], Paula Lengerke Diaz[2], Juanuario E. Castro[2], and Jeong-Yeol Yoon[1]*

[1]Department of Biomedical Engineering, The University of Arizona, Tucson, Arizona 85721, United States

[2]Hematology Oncology Division, Mayo Clinic, Phoenix, Arizona 85054, United States

*Corresponding author. E-mail: jyyoon@email.arizona.edu

Received: 27 November 2019; Received in revised form 10 January 2020; Accepted 20 January 2020; doi: 10.1016/j.bios.2020.112042

Published in Biosensors and Bioelectronics 153 (2020) 112042

Abstract

Gold standard diagnosis of hematological cancers require complete white blood cell count, followed by flow cytometry with multiple CD markers, and cytology. It requires substantial time and specialized training. A dual-layer paper microfluidic chip was developed as a quicker, low-cost, and field-deployable alternative to detect ROR1+ (receptor tyrosine-like orphan receptor one) cancer cells from the undiluted and untreated buffy coat blood samples. The first capture layer consisted of a GF/D glass fiber substrate, preloaded with cancer specific anti-ROR1 conjugated fluorescent particles to its center for cancer cell capture and direct smartphone fluorescence imaging. The second flow layer was comprised of a grade 1 cellulose chromatography paper with wax-printed four channels for wicking and capillary flow-based detection. The flow velocity was used as measure of antigen concentration in the buffy coat sample. In this manner, intact cells and their antigens were separated and independently analyzed by both imaging and flow velocity analyses. A custom-made smartphone-based fluorescence microscope and automated image processing and particle counter software were developed to enumerate particles on paper, with the limit of detection of 1 cell/μL. Flow velocity analysis showed even greater sensitivity, with the limit of detection of 0.1 cells/μL in the first 6 s of assay. Comparison with capillary flow model revealed that great alignment with experimental data and greater correlation to viscosity than interfacial tension. Our proposed device is able to capture and on-chip image ROR1+ cancer cells within a complex sample matrix (buffy coat) while simultaneously quantifying cell concentration in a point-of-care manner.

Introduction

Hematological cancers, cancers derived from the blood, are conventionally diagnosed in a manner that is very time consuming, requires expensive equipment, and demands for professionally trained personnel [1]. Such processes can be especially tiresome and invasive for patients suffering from chronic cancers that require months-worth of blood analysis. For example, chronic lymphocytic leukemia (CLL) diagnosis requires the presence of $\geq 5 \times 10^9$ B lymphocytes/L ($= 10^6$ cells/μL) in the peripheral blood, sustained for at least 3 months. The clonality of these B lymphocytes are then confirmed by demonstration of immunoglobulin light chain restriction via flow cytometry. Following, leukemia cells are also morphologically confirmed via a microscope blood smear to appear as small, mature lymphocytes with a narrow border of cytoplasm and a dense nucleus lacking discernable nucleoli with partially aggregated chromatin [2]. CLL is the most common form of leukemia in adults, accounting for 25% to 30% of all leukemia derivatives in the United States [3]. Globally, based off of data collected from 1990 to 2015, 2 out of 100,000 people (age-standardized) were reported to have CLL [4]. While a variety of treatment options are now available, CLL has a low response rate, and assessing the prognosis of patients remains difficult [5]. This project addresses the need to develop an inexpensive, rapid, and point-of-care (POC) method to identify, quantify, and detect hematological cancers, including CLL.

In recent years, various microfluidic POC assays have been developed for detection of hematologic cancer and CLL. Previously investigated microfluidic techniques include gene-specific amplification via on-chip quantitative reverse transcription polymerase chain reaction (qRT-PCR) [6,7], aptamer probe hybridization via electrochemical impedance spectroscopy [8], on-chip fluorescence microscopy of immunostained whole cells [9], cell sorting by magnetic trapping array and lectin affinity [10], and measurement of cell stiffness [11]. Although each

technique has its advantage such as specificity, multiplexing capabilities, label-free, and single-cell sorting, there are also disadvantages. First, all microfluidic platforms mentioned utilize a custom silicone-based chip, whose fabrication process can be complex and expensive, requiring special equipment and cleanroom access. Secondly, the use of nucleic acid identification techniques such as PCR or apta-sensing requires pre-assay sample preparation (i.e. extraction via cell lysis, filtration, etc.) and expensive reagents with shortened storage life, making it undesirable for field and POC applications. Lastly, cell sorting techniques with on-chip immunofluorescence imaging requires lengthy procedures of cell fixation, immunostaining with multiple fluorophores, and access to benchtop fluorescence microscopy.

Use of paper microfluidic platforms with fluorescence sensing has been demonstrated for multiple chemical and biological applications. Advantages of paper microfluidics include: an inherent pump-free mechanism via capillary and wicking action, ease and low-cost of fabrication, disposability, and increased storage-life of reagents preloaded prior to performing assay. Fluorescent nanotechnologies such as quantum dots (QD), fluorescent micro/nanoparticles, and nanoclusters have consistently shown superior stability and high sensitivity in comparison to traditional fluorescent dyes [12-14]. Additionally, smartphone optical sensing was chosen due to its holistic capabilities of being portable, user-friendly interface, ability to connect and upload to a network, and on-board processing capability [15]. However, as paper is optically opaque and generates a large extent of back scattering noise (from its fibrous structure) as well as auto-fluorescence, such detection has always been considered challenging.

In this work, we developed a dual-layer paper microfluidic chip pre-loaded with antibody-conjugated, fluorescent microparticles. This platform consisted of the top capture layer, allowing efficient filtration of the buffy coat samples and capture of the cancer cells, and the bottom flow

layer generating capillary flow through paper pores necessary for efficient mixing and subsequent antibody-antigen binding. Particle binding to the cancer cells captured on the top layer was quantified via smartphone-based on-chip microscopic imaging [16]. Particles were still aggregated by cell fragments and antigens in the bottom flow layer, causing changes in the capillary flow, which was also quantified via smartphone-based real-time monitoring of flow velocity [17]. In this manner, intact cells and their antigens were separated and independently analyzed. Through this dual detection, cancer cell concentration was evaluated in the undiluted buffy coat samples from healthy donors, dosed with known concentration of cancer cells. Buffy coat samples can easily be obtained by phlebotomy, although they still contain substantial amount of red blood cells and complex to be directly assayed in a handheld platform with satisfactory sensitivity. Through utilizing a novel image processing algorithm for microparticle immunoagglutination on paper demonstrated in [16], it is possible to make an extremely sensitive detection. Our method also involves a second mechanism of detection via flow velocity analysis, which has recently been demonstrated as an emerging alternative detection on paper microfluidic platforms [18].

The biorecognition element chosen for this assay is an antibody that has a high affinity to the receptor, tyrosine-like orphan receptor one (ROR1) protein. ROR1 has been a biomarker with increasing interest as a diagnostic tool for cancer, specifically for CLL and B lymphoma cells. The ROR1 antigen has been demonstrated in numerous studies, as a highly and specifically expressed biomarker for CLL disease expression with respect to normal B cells, normal tissues, and normal blood cells from healthy donors [19,20]. Other leukemia's such as B cell acute lymphoblastic leukemia and Harry cell leukemia have also resulted in high expression of the ROR1 protein [21]. Unfortunately, ROR1 is not easily expressed *in vitro* leukemia cell culture [22,23]; a substitute model cell should preferably be tested for *in vitro* assays. In fact, ROR1 is a

highly versatile biomarker and is found in other malignant cancers including lung, ovarian, and prostate cancer [24,25]. Therefore, for this proof-of-concept technology, we have used ROR1+ MDA-MB-231 breast cancer cells as the simulated target cells for this platform.

Overall, our unique method, which utilizes *in situ* imaging and flow-based washing, allows for fast and easy ROR1+ cancer cell detection to monitor the progression of the disease at the point-of-care. This novel assay is also far less expensive and requires much less specialized training than any of the current methods. These advantages successfully address the current need for simple ROR1+ cancer diagnostic and prognostic applications.

Materials and Methods

Cell culture and suspension

Mammary gland/breast adenocarcinoma cell cultures (MDA-MB-231; HTB-26, ATCC; Manassas, VA, USA) were grown in HyClone Leibovitz L-15 media with 2.05 mM L-glutamine (SH30525.01; GE Healthcare; Maidstone, Kent, UK) supplemented with 10% (v/v) fetal bovine serum (FBS; 30-2021; ATCC; Manassas, VA, USA), 0.1% (v/v) of 50 mg/mL gentamycin sulfate solution (IB02030; IBI Scientific; Dubuque, IA, USA), and 0.2% (v/v) of 250 µg/mL Amphotericin B (GE Healthcare; Maidstone, Kent, UK). Cells were cultured at 37°C (HERAcell 150i; Cambridge Scientific; Watertown, MA, USA) in 0% CO_2 until 80% confluent. After reaching 80% confluency, MDA-MB-231 cells were passaged following standard procedures [26]. Cells were resuspended, counted via a hemocytometer, diluted in media to 10^5 cells/mL, and stained for 15 min with NucBlue Live ReadyProbes Reagent (R37605; ThermoFisher Scientific; USA). Serial dilutions were made by pipette mixing (not by vortexing) to prevent cell

fragmentation. Excess dye was removed by centrifugation at 1.3 *g* for 5 min and resuspended in pre-warmed 1X DPBS, back to 10^2 cells/μL concentration.

Benchtop fluorescence imaging

An inverted benchtop fluorescence microscope (Eclipse TS100; Nikon Corp.; Tokyo, Japan) was used, equipped with fluorescence filters UV-2E/C and G-2A (A.G. Heinze, Lake Forest, CA, USA) and an imaging software (NIS Elements; Nikon Corp.). Greyscale images were also taken from each filter cube. Images were then superimposed with pseudo-colors: blue for NucBlue-stained cells and red for antibody-particles via ImageJ software (US National Institutes of Health; Bethesda, MD, USA).

Antibody conjugation to fluorescent microparticles

Rabbit polyclonal antibody to receptor-tyrosine-kinase-like orphan receptor 1 (anti-ROR1; OABF00363; Aviva Systems Biology; San Diego, CA, USA) was used for ROR1 expression on cancer cells. 1 M ethanolamine solution (398136; Sigma-Aldrich; St. Louis, MO, USA) was used to generate negative control signals with ROR1-positive cell cultures. Anti-ROR1 and ethanolamine were covalently conjugated to highly carboxylated, red, 1-μm diameter, fluorescent polystyrene particles (CAF-001UM; Magsphere Inc.; Pasadena, CA, USA) with reported 538 nm excitation and 584 nm emission wavelengths. Conjugation to particles were done by the following method: 1) particles were washed three times, first with 0.05% Triton-X 100 washing buffer, followed by deionized water with centrifugation of 8,100 *g* for 8 min in between each washing step; 2) washed particles were incubated with activation buffer [1 mg/mL 1-ethyl-3-(3-dimethylaminopropyl)carbodiimide (EDAC) in pH 6], 5 mM 2-(N-morpholino) ethanesulfonic acid (MES), and 1 M NaOH for 30 min on a rocker at room temperature; 3) 10

μL of 1 mg/mL ethanolamine or anti-ROR1 antibody solutions were added to activation buffer and particle mixture and placed on a rocker for 2 h at room temperature; 4) 1 M ethanolamine buffer was added to quench reaction and placed on a rocker for 30 min at room temperature; 4) antibody-particle or ethanolamine-particle suspensions were centrifuged and washed similar to step 1, but with added 5 min sonication in between resuspension and centrifugation. Particles were stored in deionized water in 3-8°C. This EDAC-based covalent conjugation of antibodies to carboxylated polystyrene particles has been well-documented to yield a uniform distribution of antibodies on the particle surface [27], since the carboxyl-containing co-monomers repel from each other and from hydrophobic main-monomer (styrene). In addition, a total of four batches of antibody-conjugated particles were used throughout this work to address the batch-to-batch variations.

Capture layer substrate selection – optimum cell retention and particle relief

The paper microfluidic chip is comprised of two layers: the first capture layer and the second flow layer. Pre- and post-washing steps were evaluated for two types of the capture layer's ability to retain cells after washing and relieve unbound particles. NucBlue-stained cell suspension or anti-ROR1/ethanolamine conjugated fluorescent particle suspension was applied to 6 mm diameter mechanically-punched paper rounds of GF/D borosilicate microfiber filter (1823-047; Whatman GE Healthcare; Maidstone, Kent, UK) or G041 glass fiber conjugate pad sheets (Milipore Sigma, Billericia, MA, USA). After a 5 min waiting period, paper rounds were flipped and imaged using a fluorescence microscope with the addition of a drop of mineral oil to omit undesired scatter off glass fibers. The collected images were evaluated for pre-wash steps. Post-wash assay images were taken with the continuation of 100 μL of 0.05% Triton-X 100 (T8787, 398136; Sigma-Aldrich; St. Louis, MO, USA) washing buffer solution to paper rounds

with a 1 in × 1 in (25.4 mm × 25.4 mm) grade 1 chromatography paper (Whatman Grade 1 Chr, GE Healthcare, Maidstone, Klent, UK) underneath. After a 5 min waiting period, the paper rounds were flipped and imaged with the addition of mineral oil.

Well plate assay procedure

6×10^4 MDA-MB-231 cells/mL were seeded into 96-well plates and incubated overnight. Cells were prepared for a specificity assay by washing with 1X DPBS twice, fixing with 4% paraformaldehyde for 15 min at room temperature, and washing again with 1X DPBS twice. Red fluorescent anti-ROR1 particles were then added and incubated for 30 min at room temperature. To remove unbound particles, a 0.05% Triton X-100 washing buffer was used to wash cells twice. 1X DPBS was then added to wells to prevent drying during imaging. As a control, wells with no cells were incubated in media overnight, followed by washing, fixing, and incubating with particles under the same conditions of the wells with cells. Four 400X fluorescent images were taken for each well, where each image represented one field-of-view (FOV). All particles were counted for each FOV and tallied for frequency in occurrence. Particles counts greater than 16 particles per FOV were omitted due to insufficient washing of unbound particles.

Paper chip design and fabrication

The microfluidic chip was comprised of two layers. The first layer (capture layer) was 6-mm diameter, mechanically punched rounds made out of GF/D or G041 glass fiber substrates, for preloading antibody-conjugated particles and initial capturing of whole cancer cells (Figure 1A). The second layer (flow layer) was designed using SolidWorks 2015 software (Dassault Systèmes, Vélizy-Villacoublay, France) and wax-printed (ColorQube 8580, Xerox, Norwalk, CT, USA) on grade 1 chromatography paper for wicking and capillary flow measurements along

four channels. The width (2 mm) and length (5 mm) of the four channels on the second flow layer was selected from multiple iterations for a 10 μL sample to be distributed amongst the four channels evenly and to flow along the channel for measurable distances for the smartphone to take a video without magnification or zoom (Figure 1B). After the pattern was printed, chips were cut and melted at about 120°C for 5 min to allow for wax to flow into the paper fibers creating hydrophobic barriers throughout the depth of the paper.

Paper chip assay procedure

10 μL of anti-ROR1 conjugated particles were preloaded to the center of the first capture layer of the paper microfluidic chip, followed by drying at room temperature, prior to its binding to the second flow layer. Cell suspensions of 10^2 cells/μL were serially diluted down to 0.1 cells/μL in 1X buffy coat (SER-BC-SDS, ZenBio, Research Triangle, NC, USA). 10 μL of dosed samples were applied to the center of the capture layer with a 1 mL syringe attached with an 18-gauge blunt needle tip (outer diameter = 1.27 mm) (Figure 1A). Flow along the four channels of the second flow layer of the paper chip was monitored via capturing 30 fps videos using a smartphone (Samsung Galaxy S8; Samsung, Suwon, South Korea), without separating the capture layer (Figure 1B). Once all channels have been saturated the video was ended and 3 steps of 30 μL washing buffer was added to the capture layer every 1 min. The capture layer was then separated and placed on a microscope stage for particle count analysis (Figure 1C).

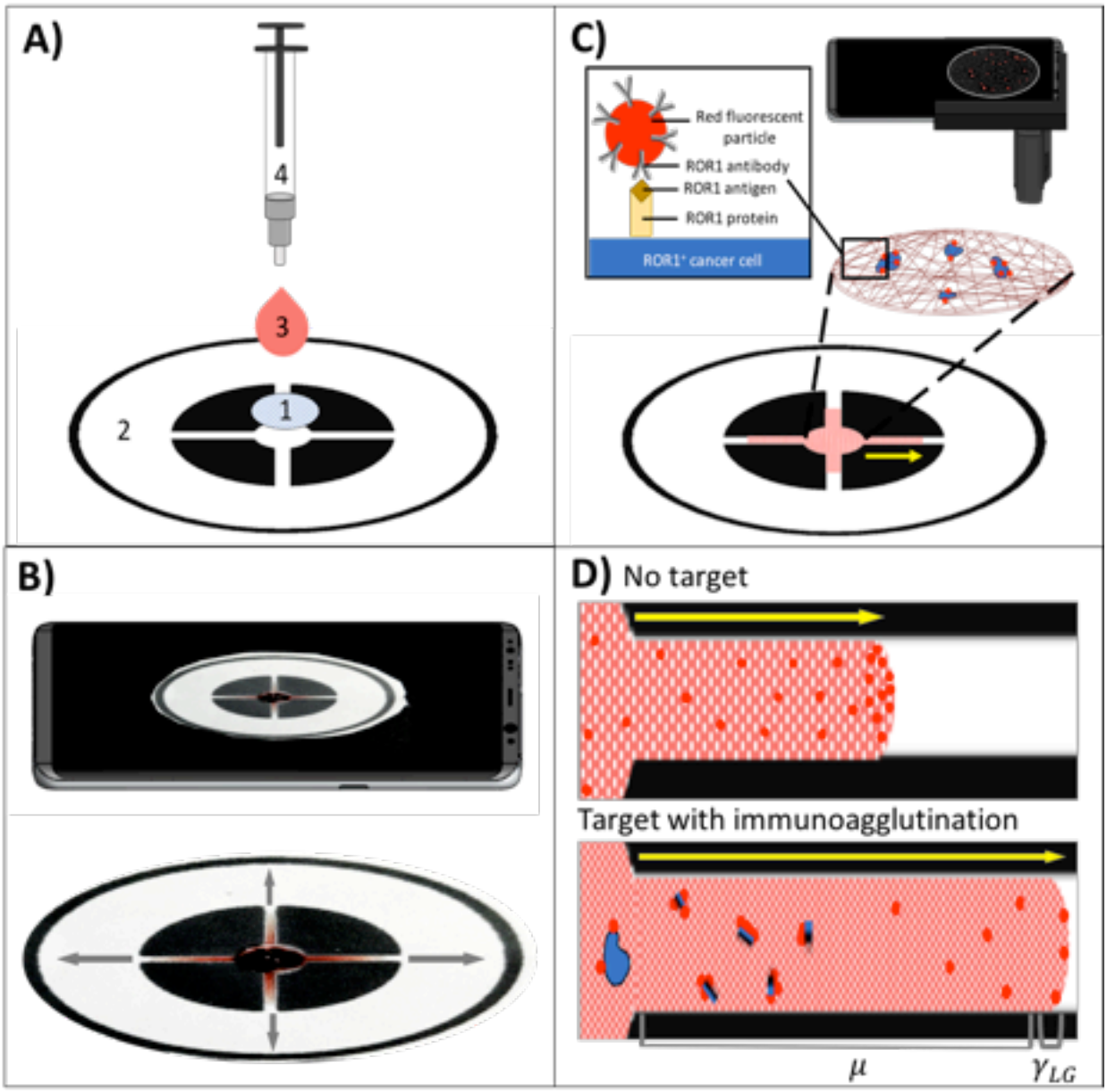

Figure B-1 (A) Dual-layer paper chip assay procedure with 1) a capture layer (glass fiber), pre-loaded with red fluorescent, anti-ROR1 conjugated microparticles, 2) a flow layer (wax-printed chromatography paper), 3) a buffy coat sample with dosed cancer cells, and 4) a blunt-end needle tip syringe for uniform droplet application. (B) A smartphone captures a video for monitoring the flow velocity from the flow layer. (C) A smartphone-based fluorescence microscope images the capture layer for quantifying ROR1+ cancer cell. (D) Schematic of flow based detection with no target (more particles at the flow front, increasing interfacial tension γ_{LG})

and with target (more particles not at the flow front due to immunoagglutination, increasing viscosity μ).

Design and assembly of smartphone-based fluorescence microscope device

Cells captured on the capture layer were imaged with a custom-made smartphone fluorescence microscope. A commercially available smartphone microscope (AOMEKIE Cellphone Microscope Magnifier; 60X-100X zoom with a UV LED) was modified as follows: Firstly, the existing LED was replaced with a 525 nm blue LED (MTE5052M3A-UBG, Marktech Optoelectronics, Thief River Falls, MN, USA) for fluorescence excitation of antibody-conjugated microparticles. Secondly, a 3D-printed attachment (an enclosure and a moveable stage) was constructed and added to the microscope to provide a dark enclosure and a moveable stage, made out of black acrylonitrile-butadiene-styrene (ABS) polymer using a 3D printer (Zortrax M200, Zortax Inc., Olsztyn, Poland). This attachment was designed using SolidWorks. Thirdly, the attachment was also designed to incorporate a 589 ± 2 nm optical bandpass filter (65-707, Edmund Optics, Barrington, NJ, USA) to capture fluorescence emission from the same particles.

Image processing algorithm – particle count

Both smartphone and benchtop microscope images were pre-processed and analyzed via MATLAB 2019a (MathWorks, Natick, Massachusetts, MA, USA). The pre-processing algorithm includes the use of a bandpass noise filter in the Fourier Space to enhance higher frequency signals and filter out low frequency signals caused by autofluorescence or undesirable light scatter. An optimal binary threshold of 0.6 was then applied, highlighting only the antibody-conjugated fluorescent particles on paper. A circular object function was then utilized to count and augment the measured diameters onto the pre-processed image. ImageJ 1.51m9 (National

Institutes of Health, Bethesda, MD, USA) was also used to analyze benchtop microscope images for initial substrate optimization and specificity test.

Image processing algorithm – flow analysis

30 fps videos were parsed into 1 s time interval images. Images were processed and analyzed via MATLAB. Auto-contrast stretching [24] and chromatic adaptation function [25] were used for white balance as well as for the enhancement to better detect buffy coat color. Binary thresholds and fill-in functions were also used prior to measure lateral capillary flow distance from the edge of the first capture layer. A moving average was then applied to raw measurements. Capillary flow velocity was then determined as the slope of the average flow distance at 3 different time intervals: Δt_1, Δt_2, Δt_3, and Δt_4, which correspond to 2 to 6 s, 7 to 12 s, 13 to 22 s, and 23 to 32 s.

Viscosity measurements

The viscosity of each mixture containing particles and target cells in growth media (L15) was measured using oscillatory shear rheology on a Discovery Hybrid Rheometer 2 (TA Instruments, New Castle, DE, USA) with a 40 mm diameter and 0.5° cone geometry. Sample mixtures were pipetted and spread evenly on a 40 mm stage before lowering the gap height to 30 μm. A Peltier temperature-controlled stage maintained samples at 37°C during rheology measurements. A shear stress sweep was performed from 0.001 to 100 Pa at a constant 10 rad/s angular frequency. The viscosity of particles and cancer cell mixtures from 0 to 100 cells/μL was determined by the slope of the shear stress (τ) vs. shear strain rate ($\dot{\gamma}$) plot [26,27].

Interfacial tension measurements

Interfacial tension (mN/m) was measured with an FTÅ200 contact angle/surface tension analyzer (First Ten Ångstroms, Portsmouth, VA, USA) using the pendant droplet method. Five 10 μL of anti-ROR1 particles with either 100, 10, 1, 0.1, or 0 (NTC) of MDA-MB-231 cells/μL were prepared. Particle-cell mixture were then extruded from an 18-gauge blunt needle (outer diameter = 1.27 mm) and measured.

Results and Discussion

Selection of the capture layer substrate for optimum cell and particle retention

Two different types of capture layer were investigated to determine best ability to retain cells and relieve particles after the washing step. Figure 2A shows the average cells or cluster per field-of-view (FOV) for MDA-MB-231 breast cancer cells on G041 and GF/D glass fiber substrates. Average cells/cluster per FOV were 2.2 for pre-wash and remained the same for post-wash on G041. In comparison, average cells/cluster per FOV were 4.0 for pre-wash and 2.7 for post-wash with GF/D. More cells/clusters were observed with GF/D than G041 and washing was more effective with GF/D. Figure 2B illustrates capture layer's ability to retain or relieve particles post-wash. More particles were captured with GF/D than G041, and more particles were retained after washing with GF/D than G041.

In addition, we found that the GF/D produced less undesired background scatter over G041. G041 fibers acted as miniature optical fibers that transmitted and propagated the excitation light along the fiber itself causing difficulty in distinguishing the fluorescence from the NucBlue-stained cells or the fluorescent particles. While we did find that such background light scatter could be reduced when mineral oil was added. By adding mineral oil to the glass fiber substrate for fluorescence imaging we reduced the difference in refractive index between the glass fibers

(n = 1.5) and the surrounding media (n = 1.47 for mineral oil vs. n = 1.00 for air). Unfortunately, it was not a significant enough reduction method in noise in comparison to the GF/D paper substrate. Taken together, GF/D was chosen as the better substrate for the capture layer.

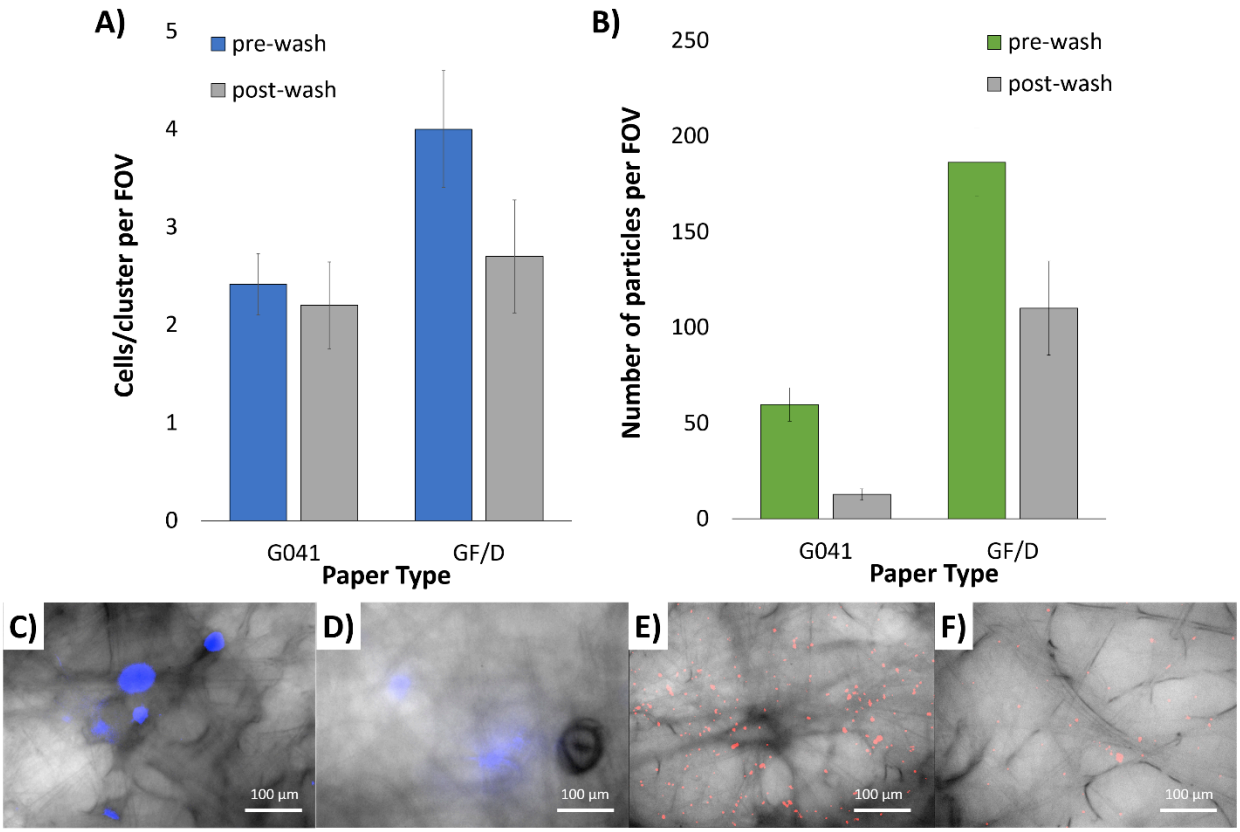

Figure B-2. Selection of capture layer substrate for optimum cell retention comparing pre- and post-wash of (A) MDA-MB-231 cells and (B) BSA-conjugated particles, on G0401 and GF/D glass fiber substrates. Averages of 5 assays. Error bars represent standard errors. 400X microscopic overlaid images of (C) pre- and (D) post-wash NucBlue-stained MDA-MB-231 cells, as well as (E) pre- and (F) post-wash red fluorescent BSA-conjugated particles, both on GF/D glass fiber substrates.

Verification of specific binding of anti-ROR1 particles to cells via well-plate assays

MDA-MB-231 ROR1+ cells were seeded onto tissue culture well plates (TCP) and fixed with formaldehyde to run specificity tests of antibody-conjugated particles. Anti-ROR1 particles were added to wells with and without cells seeded, incubated, and washed. Supplementary Figure S1A depicts the frequency tally of randomly chosen FOVs in which the total number of particles were counted. As shown, anti-ROR1 particles had a higher frequency with higher number of particles in FOVs where MDA-MB-231 cells were present. The highest frequency count had 4 FOVs with 8 total particles, followed by 3 FOVs with 12 total particles. In comparison, areas with no cells had low frequency FOV counts of 1, however ranging from 0 to 12 total particles in FOV. Supplementary Figure S1B and S1C are FOVs in which anti-ROR1 is specifically binding to MDA-MB-231 cells. It is also observed that anti-ROR1 particles are also clustered in areas near, but with no MDA-MB-231. This suggests that although whole cells are not present, antigens may be responsible for particle binding and clustering, presumably due to the use of a surfactant-based washing buffer as well as the inherent mobility of cells during growth.

On-chip particle counting using a benchtop fluorescence microscope

A dual-layer paper microfluidic chip was designed and fabricated as shown in Figure 1A. The first capture layer is a mechanically punched, 6-mm diameter GF/D glass fiber where the cells are loaded and captured. GF/D was selected as the optimal paper substrate in capture and retention of cells and particles, as previously discussed. The second flow layer of cellulose chromatography paper allowed for wicking of applied sample and washing buffer. Four channels were designed and wax-printed to create hydrophobic barriers.

Fluorescence imaging was initially conducted for the first capture layer using a benchtop fluorescence microscope (Figure 3A). Particle area in FOV was evaluated in relation to varying cell concentration in a buffy coat matrix utilizing a custom MATLAB particle analyzer code (Figure 3B). Image pre-processing algorithm with Fourier bandpass noise filtering and binary thresholding was used prior to measuring particles in FOV (Figure 3C). The Fourier bandpass filtration mitigates low frequency and high frequency signals leaving an image in which an optimal frequency corresponding to the fluorescence light of the anti-ROR1 particles. This leaves an image of varying light intensities, in which a binary threshold is applied to result in fluorescence from the particles in a clear format to determine the total pixel area of captured particles. ROR1+ cells were serially diluted to 0.1 to 100 cells per/μL in buffy coat. 400X images were taken, processed, and measured for area of particles in FOV. The general trend was as cell concentration increased, particle area in FOV increased. With 100 cells/μL an average particle area of 2264 pixels in FOV was statistically different in comparison to no target control (NTC; no cancer cells) with the p value of $1x10^{-6}$. Following, 10 cells/μL was also statistically different with an average particle area of 1164 pixels in FOV with the p value of 0.007. Following, cell concentrations of 1 and 0.1 cells/μL with average particle areas of 132 and 206 pixels were statistically different from NTC with the p values of 0.023 and 0.001 (Figure 3D).

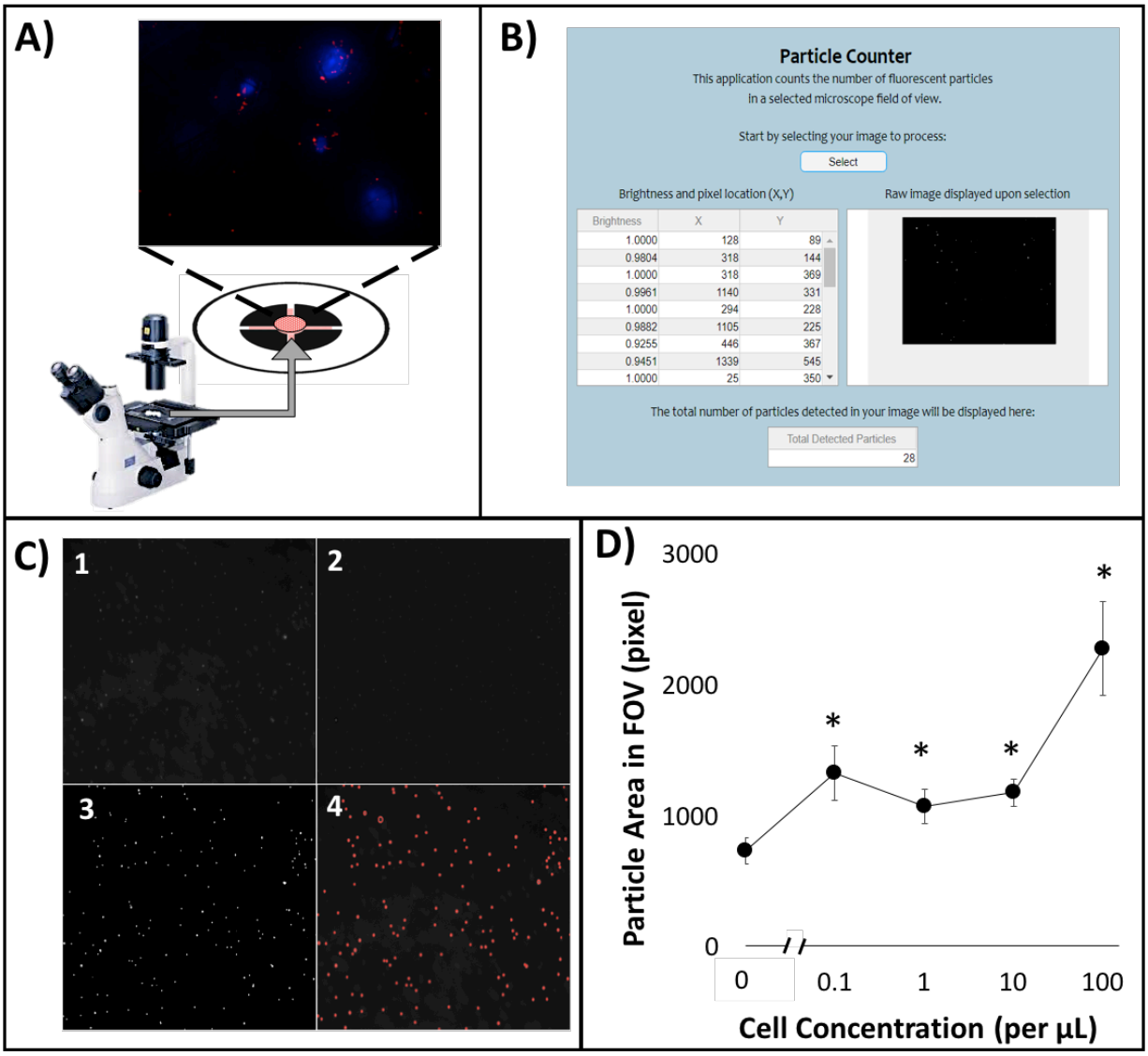

Figure B-3. (A) On-chip particle counting analysis from the first capture layer of the dual-layer paper microfluidic chip using a benchtop fluorescence microscope. (B) MATLAB graphical user interface (GUI) for counting particle areas. (C) Raw and processed images: (1) raw 400X image, (2) Fourier bandpass filtered image with adjusted brightness and contrast, (3) image after grayscale normalization and global threshold binarization, and (4) final image with augmented particle detection. (D) Particle area in FOV in relation to dosed ROR1+ cell concentration from 0.1 to 100 cells/µL.

On-chip particle counting using a smartphone-based fluorescence microscope

The correlation between particles area in FOV and concentration of dosed ROR1+ cancer cells in buffy coat was demonstrated utilizing a smartphone-based fluorescence microscope, for its application in a more user-friendly and field-deployable manner. As shown in Figure 4A, a smartphone microscope was attached to the camera of a smartphone via a phone case and used to capture images of fluorescent anti-ROR1 particles on the second flow layer of the dual-layer paper microfluidic platform. To filter true signals from noise, especially from the GF/D glass fiber substrate, further physical light filtering and image digital processing were utilized. The smartphone attachment was comprised of three components: 1) 589 ± 2 nm optical bandpass filter that allows only the fluorescence emission from anti-ROR1 particles to the smartphone camera, 2) a commercially available smartphone microscope, replaced with a 525 nm LED, specific to the excitation wavelength to the anti-ROR1 particles, and 3) 3D printed enclosure and user-movable stage that housed the paper microfluidic chip with captured cells and particles. The optical bandpass filter mitigates weaker, non-specific fluorescence as well as reducing the amount of light. A Fourier bandpass filtering and binary thresholding algorithm (used for the benchtop fluorescence images) was also used to quantifying particles in FOV (Figure 4B). The MATLAB particle analyzer code and its GUI used for benchtop fluorescence microscopy (Figure 3B) were also used for smartphone-based fluorescence microscopy, using MATLAB Mobile (Supplementary Figure S2A). The operation procedure for final user is also illustrated in Supplementary Figure S2B.

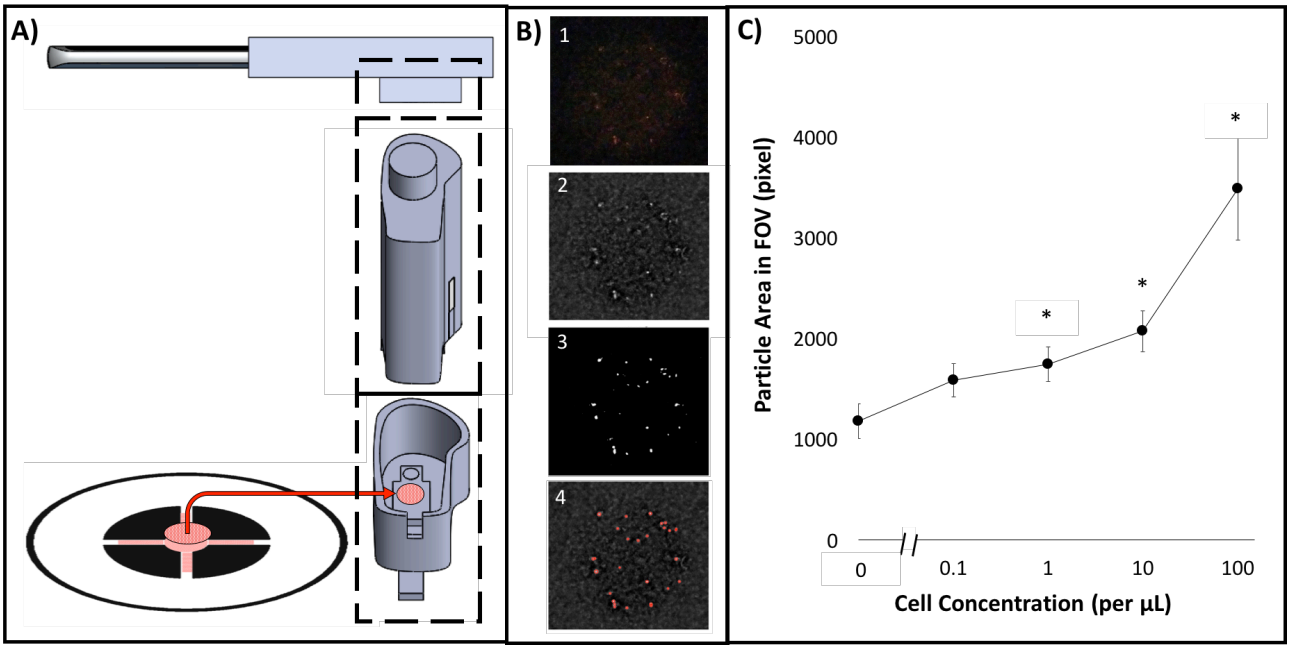

Figure B-4. (A) On-chip particle counting analysis from the first capture layer of the dual-layer paper microfluidic chip using a smartphone-based fluorescence microscope. The smartphone-based fluorescence microscope is comprised of (1) a smartphone case (180 mm x 80 mm), (2) a 25-mm diameter, 589 ± 2 nm optical bandpass filter, (3) a commercial smartphone microscope attachment, replaced with a 525 nm LED, and (4) a 3D printed enclosure and a moveable stage with manual user lever. (B) Raw and processed smartphone images: (1) raw cropped 300X image, (2) Fourier bandpass noise filtered image, (3) image after grayscale normalization and global threshold binarization with threshold of 0.4, and (4) final image with augmented particle detection. (D) Particle areas in FOV in relation to dosed ROR1+ cell concentration from 0.1 to 100 cells/µL.

ROR1+ cells were serially diluted in buffy coat to obtain cell concentrations of 0.1, 1, 10, and 100 cells/µL. 200X images were taken via smartphone-based microscope, processed, and measured for particle area in FOV. A similar trend to the benchtop fluorescence microscope was observed. With increasing cell concentration, particle area in FOV present increased. At 100

cells/μL, an average particle area of 3487 pixels were measured in FOV and was statistically different in comparison to no cells (NTC). Similarly, 10 and 1 cells/μL concentration dosed in buffy coat were statistically different from NTC with average particle areas in FOV of 2071 and 1744 pixels. However, 0.1 cells/μL was not statistically different from NTC having an average particle area in FOV of 1179 pixels (Figure 4D).

Flow velocity analysis using a smartphone camera

The second flow layer of the dual-layer microfluidic chip was designed to have four channels to wick the sample solution from the center and to quantify antigens and cell fragments not captured in the first capture layer. A smartphone captured 30 fps videos during the assay, which were parsed into 1 s interval images, color enhanced, and measured for flow distance (Figure 5A). Antibody-conjugated particles are aggregated upon binding to targets, in this case, mostly antigens released from cells or possibly cell fragments, but not the whole cells (ranging from 5 to 10 μm) as they are mostly captured in the first capture layer and are too big to flow through the second flow layer (20 μm). Non-aggregated particles easily adsorb to the liquid-air interface (i.e. moving front) within paper fibers due to their relative hydrophobicity, and subsequently lowers the interfacial tension. Aggregated particles, however, diffuse to the liquid-air interface substantially slower, and the resulting flow velocities (flow distances) should be substantially different between non-aggregated and aggregated particles, i.e. between target non-presence and presence [14] (see Figure 1C for illustrated flow detection phenomenon). The presence and nature of blood components also affects the flow velocity (distance) [32].

The flow velocity in which applied sample flows from the loading zone was investigated, originating from spontaneous wicking effects of paper in correlation to cancer cell concentration

present in buffy coat. Flow velocity was measured at four time-intervals: Δt_1, Δt_2, Δt_3, and Δt_4, which correlated to 2 to 6 s, 7 to 1 2s, 13 to 22 s, and 23 to 32 s, respectively (Figure 5B). Δt_1 showed the greatest sensitivity and significant differences in flow velocities for all cell concentrations in comparison to NTC (no cancer cells) samples. Average flow velocities ranged from 2.75 pixels/s at 1 cell/μL and 3.88 pixels/s at 10 cells/μL. Δt_2 and Δt_3 showed significant differences in average flow velocities for all cell concentrations in comparison to NTC samples except for 1 cell/μL at Δt_2. Average flow velocities ranged from 2.05 pixel/s and 3.57 pixels/s. Lastly, Δt_4 displayed the least dynamic range and least significant difference in average flow velocity to NTC samples. Overall Δt_3 time interval flow velocities in correspondence to dosed cancer cells in buffy coat showcased the best overall dynamic range, where 100 cells/μL (high concentration) delayed signal, was able to be detected. Therefore, Δt_3 time interval flow velocities were used as the empirical comparison to a capillary fluid dynamic model.

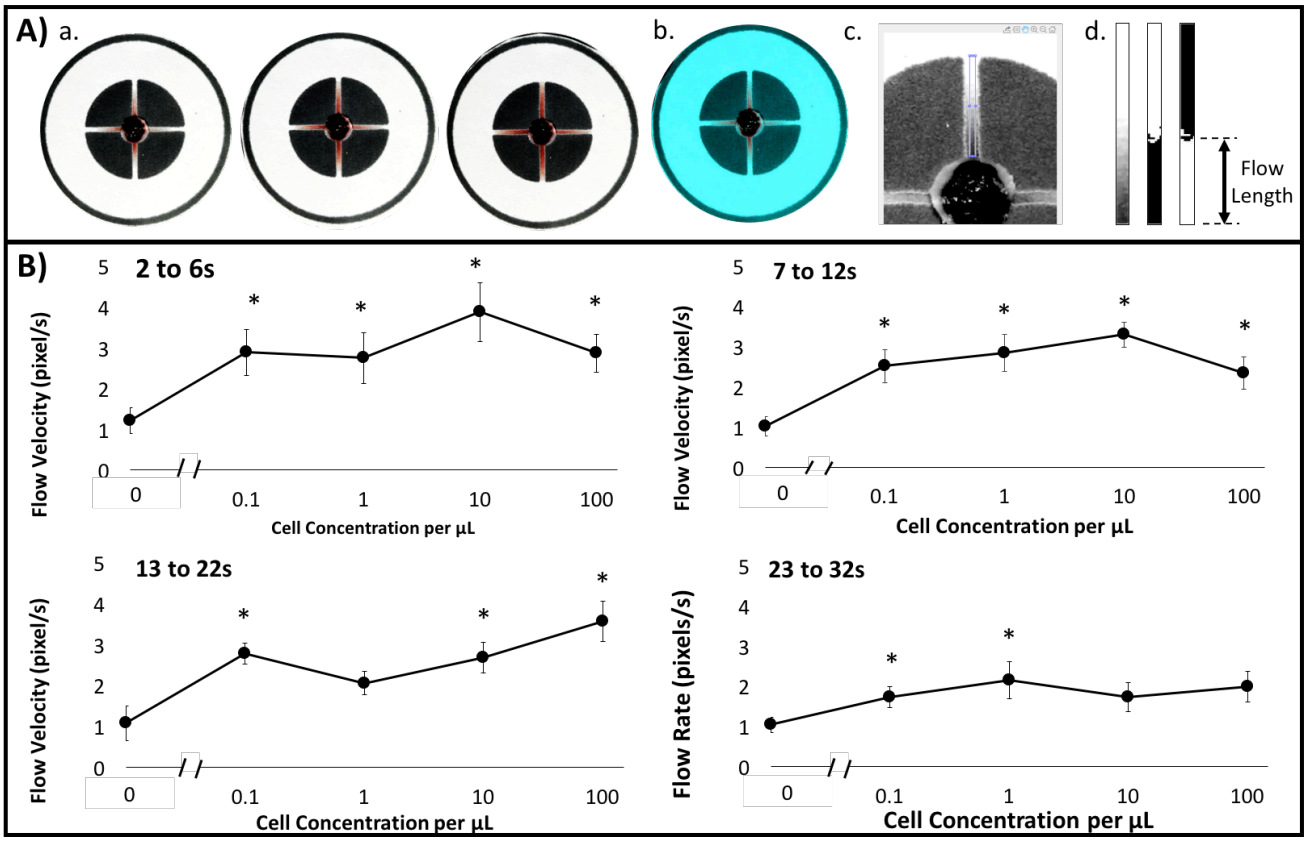

Figure B-5. Image processing algorithm for evaluating capillary flow velocites from smartphone-acquired videos: (1) Parsed 30 fps video to 1 s image shots; (2) Color balanced image to [150, 100, 100] RGB pixel intensities; (3) Extracted green channel image with user-designated channel crop tool; (4) Cropped, binary, and inverted images of channel of interest, from left to right. (B) Capillary flow velocities in relation to dosed buffy coat with cell concentration from 0 to 10^2 cells/µL at four different time intervals: Δt_1, Δt_2, Δt_3, and Δt_4, which correlated to 2 to 6 s, 7 to 12 s, 13 to 22 s, and 23 to 32 s, respectively.

As seen in Figure 5B the four different panels are the average flow velocities at different time intervals after the assay start time, which is after the dosed-cancer cell buffy coat sample is applied to the first layer. At Δt_1 and Δt_2 time intervals signals at the highest concentration, 100 cells per µL, are dropping in comparison to the lower concentrations of 0 to 10 cells per µL,

where it is an overall proportional relationship. This can be explained since at higher concentrations there are more cells being captured in the first layer, therefore delaying the flow antigen detection mechanism at the second layer. As we increase the time in which we observe the flow velocity, Δt_3 at 13 to 22s, 100 cells per μL shows a higher flow velocity than in preceding lower concentrations. Therefore Δt_3 showed the most dynamic range and was used to compare to the modified Lucas-Washburn model. Lastly, Δt_4 shows non-significant increase in flow velocity in relation to cell concentration because the signal has been saturated at longer periods of time.

Comparison with Lucas-Washburn capillary flow model

A common and widely used model for capillary flow through paper microfluidics is the Lucas-Washburn (L-W) model relating flow distance (l) over time (t) [29].

$$l^2 / t = (R\, \gamma_{LG} \cos \theta) / (2\mu) \quad (1)$$

As demonstrated in [13], the changes in R (pore size) and θ (contact angle) were negligible compared to those in viscosity (μ) and interfacial tension (γ_{LG}) upon changing the target concentration and particle aggregation. Therefore, we assumed R and θ to be constant and measured μ and γ_{LG} of 0 to 10^2 cells/μL cell suspensions with anti-ROR1 particles as input parameters into the model. Relative viscosity (μ) was determined from shear stress (τ) versus shear rate ($\dot{\gamma}$) curves (Supplementary Figure S2) via cone-plate rheology. It should be noted that 0.1 cells/ μL was mitigated from data set since number of cancer cells in sample volume is too low for accurate rheology measurements due to competitive adsorption to surface [26]. It showed an inverse relationship with increased cell concentration, with up to a 31% decrease in viscosity

at 100 cells/μL (Figure 6A). Relative interfacial tension (γ_{LG}) measurements via pendant droplet analysis showed no significant trends with increased cell concentration. IFT differed from no cell samples by an increased 5% at the maximum concentration of 100 cells/μL (Figure 6B). Therefore, the most influential driving force for our system with regards to capillary flow-based detection is viscosity.

Inputting measured viscosity and IFT values to the equation 1 and normalized to that of 0 cell/μL provided the relative flow rate (l^2/t), where the constant R and θ are cancelled out. It resulted in an increasing flow as cell concentration increases with up to 34% at 100 cells/μL in comparison to no cell samples. Relaying back to the empirical data collected for flow velocities with varying cancer cell concentrations in comparison to the L-W modified model, similar trends were achieved (comapre Figure 5B: Δt_3 = 13 to 22s and Figure 6C). This suggests that particle immunoagglutination due to free antigen presence decreases relative viscosity before the moving front contributing to less unbound particles at the interface, thus resulting in increased flow. In comparison, absence of particle immunoagglutination due to no target presence, allows more free particles to quickly move to the moving front increasing the relative flow along the channel (Figure 1C).

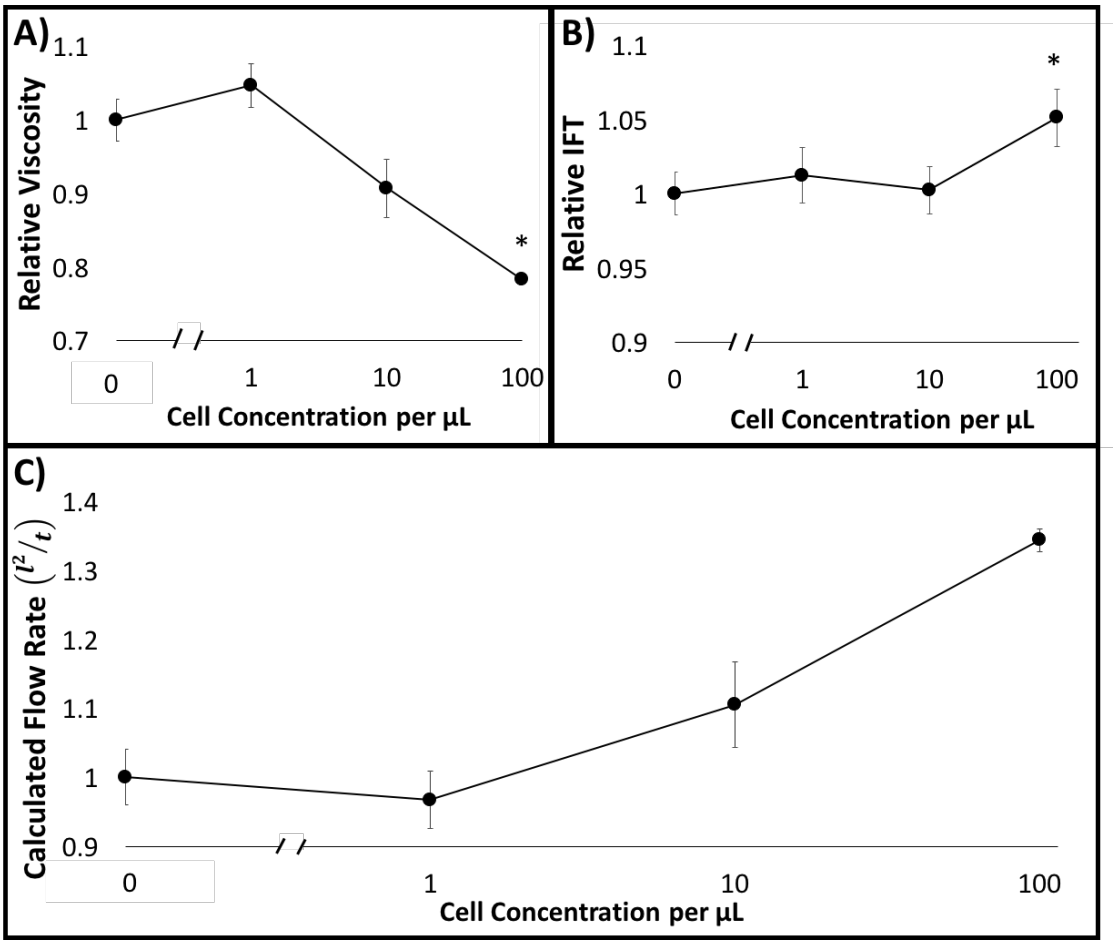

Figure B-6. (A) Relative viscosity (μ) measurements via cone-plate rheology for 0 to 10^2 cells/μL cell suspensions with anti-ROR1 particles. (B) Relative interfacial tension (γ_{LG}) measurements via pendant drop analysis for the same. (C) Relative flow (l^2/t) normalized to zero cell concentration, calculated with Lucas-Washburn capillary flow model using the parameters obtained from A and B.

This viscosity contribution to the flow velocity-based assay may be affected by another factor: the viscosity variance of buffy coat blood samples among patients. In a case study [34], blood rheology parameters were investigated for red blood cells, white blood cells, and total cholesterol levels. Changes in blood viscosity were primarily due to red blood cell related factors, but not the white blood cell or cholesterol related factors. Even the variance in red blood

cells was marginal when the shear rate is lower than 40 s^{-1}. Therefore, patient variations can potentially be neglected when the buffy coat samples are tested.

Challenges in assay reproducibility

The sample matrix itself was pooled buffy coat purchased from commercial vendors. Since pooled blood was used, it is representative of the breadth of variations introduced from individual patient samples such as hematocrit concentration (red blood cell concentration), total cholesterol, and viscosity. Buffy coat aliquots were initially produced and stored in deep freezer, then thawed in a water bath prior to performing assay. This procedure was followed to lower variation of sample matrix composition and integrity between assays done on different days.

Other variations that may have been taken into consideration, are the variations introduced from the $ROR1^+$ cancer cells, MDA-MB-231 breast cancer cells. Initially, commercially purchased cell lines were grown to confluency, then stored in a liquid nitrogen environment. This process was continued until enough passages were performed to produce enough cells for experimentation. Batches that were less than passage 10 were grown, detached, and immediately used for assays for $ROR1^+$ cancer cell concentration dosing into buffy coat sample matrix. Fresh cells were used to model a more representative clinical sample as well as reduce variabilities that could be introduced if using frozen aliquot cells from the same batch were used due to degradation during storage. Also, particle synthesis batch to batch variation was taken into account via the use of a standard curve. In total four anti-ROR1 conjugation to polystyrene particles were synthesized and used for experiments throughout this paper.

Furthermore, challenges in reproducibility with the CLL dual-layer assay lie within the variation of the fabrication of the paper microfluidic assay. Environmental factors such as humidity can be a factor to take into account when evaluating the fabrication of paper

microfluidic assays. All assays were stored and performed at room temperature under the same conditions. However, in future experiments humidity and weather conditions in which the assay is being performed should be noted to determine if meaningful trends are attributed to environmental factors.

Other factors revolving around the paper microfluidic fabrication's variability in reproducibility is the placement of fibers in relation to the first and second layer. Orientation of fibers in relation to the first and second layer were randomly placed at the start of each assay during the pre-loading of antibody conjugated particles to first layer. However, it should be noted that pore size can be varied solely based on the orientation. For example, if paper fibers were parallel versus perpendicular can greatly affect the capturing layer's retention ability. In future work, paper fiber orientation between the first and second layer should be tracked to determine if meaningful correlations exist. Overall, we believe that these variables do not majorly contribute to errors, since statistical trends were still able to be obtained.

Conclusion

In summary, we have developed a dual-layer paper microfluidic chip quantifying both whole cells captured on-chip through imaging the antibody conjugated fluorescent particles and antigen/cell fragment through monitoring capillary flow velocities. This proposed method was demonstrated for detecting ROR1+ cancer cells in a complex matrix of buffy coat samples that would be similar and relevant for clinical use. The similarity between these two assays also suggests that they can be used in a complementary manner in quantifying ROR1+ cancer cells. It is a quick and low-cost alternative to detect hematological cancer including chronic lymphocytic leukemia (CLL) in comparison to traditional, lengthy, and expensive cell counting methodologies and label-specific assays. MATLAB codes and GUIs were developed for on-chip

image analysis as well as flow measurement. Direct imaging of particles found in the capture layer demonstrated the device's ability to quantify cell concentration down to 1 cell/μL utilizing a smartphone based fluorescent microscope. Flow velocity measurements from parsed and color-enhanced smartphone videos showed statistical differences from no target samples as early as 6 s for the cell concentration down to 0.1 cells/μL. Flow measurements were validated and fitted to a Lucas-Washburn (L-W) model that was fed empirically collected relative viscosity and interfacial tension measurements. The L-W model fitting suggested that the flow detection method for our specific system, was driven by viscosity as most influential parameter contributing to increased flow with increased cell concentration. The overall procedure requires one pipetting for loading a sample, separation of a dual-layer paper microfluidic chip, and acquisition of a video and microscope images, with the assay time less than 10 minutes. This device and method can easily be translated and modified for clinical applications as well as other targets of interests such as other ROR1+ cancer cells (with high cell load), mammalian, bacterial, or plant cell types.

Acknowledgments

The authors would like to thank Katelyn Sosnowski for help and expertise in MATLAB flow analysis software Dr. Minkyu Kim for rheology instrumentation and lab access. R.Z. and A.G. acknowledges W.L. Gore & Associates, Inc. and The University of Arizona Maximizing Access to Research Careers Program for their undergraduate research fellowships. This work was supported by the Cardiovascular Biomedical Engineering Training Grant from U.S. National Institute of Health (Grant Number T32HL007955).

References

[1] Hallek, M., Cheson, B.D., Catovsky, D., Caligaris-Cappio, F., Dighiero, G., Döhner, H., Hillmen, P., Keating, M.J., Montserrat, E., Rai, K.R., Kipps, T.J. 2008. Guidelines for the diagnosis and treatment of chronic lymphocytic leukemia: A report from the International Workshop on Chronic Lymphocytic Leukemia updating the National Cancer Institute - Working Group 1996 guidelines. Blood 111, 5446–5456.

[2] Rozman, C., Montserrat, E. 1995. Chronic lymphocytic leukemia. New Engl. J. Med. 333, 1052-1057.

[3] Rai, K.R., Stilgenbauer, S., Aster, J. 2019. Clinical features and diagnosis of chronic lymphocytic leukemia/small lymphocytic lymphoma - UpToDate. <https://www.uptodate.com/contents/clinical-features-and-diagnosis-of-chronic-lymphocytic-leukemia-small-lymphocytic-lymphoma> (accessed 07-Sep-2019).

[4] Global Burden of Disease Cancer Collaboration. 2017. Global, regional, and national cancer incidence, mortality, years of life lost, years lived with disability, and disability-adjusted life-years for 32 cancer groups, 1990 to 2015: A systematic analysis for the global burden of disease study. JAMA Oncol. 3, 524–548.

[5] Rai, K.R., Sawitsky, A., Cronkite, E.P., Chanana, A.D., Levy, R.N., Pasternack, B.S. 1975. Clinical staging of chronic lymphocytic leukemia. Blood 46, 219-234.

[6] Abruzzo, L.V., Lee, K.Y., Fuller, A., Silverman, A., Keating, M.J., Medeiros, L.J., Coombes, K.R. 2005. Validation of oligonucleotide microarray data using microfluidic low-density arrays: A new statistical method to normalize real-time RT-PCR data. BioTechniques 38, 785-792.

[7] Abruzzo, L.V., Barron, L.L., Anderson, K., Newman, R.J., Wierda, W.G., O'Brien, S., Ferrajoli, A., Luthra, M., Talwalkar. S., Luthra, R., Jones, D., Keating, M.J., Coombes, K.R. 2007. Identification and validation of biomarkers of IgVH mutation status in chronic lymphocytic leukemia using microfluidics quantitative real-time polymerase chain reaction technology. J. Mol. Diagn. 9, 546-555.

[8] Ensafi, A.A., Amini, M., Rezaei, B., Talebi, M. 2016. A novel diagnostic biosensor for distinguishing immunoglobulin mutated and unmutated types of chronic lymphocytic leukemia. Biosens. Bioelectron. 77, 409-415.

[9] Jackson, J.M., Taylor, J.B., Witek, M.A., Hunsucker, S.A., Waugh, J.P., Fedoriw, Y., Shea, T.C., Soper, S.A., Armistead, P.M. 2016. Microfluidics for the detection of minimal residual disease in acute myeloid leukemia patients using circulating leukemic cells selected from blood. Analyst 141, 640-651.

[10] Vickers, D.A.L., Hincapie, M., Hancock, W.S., Murthy, S.K. 2011. Lectin-mediated microfluidic capture and release of leukemic lymphocytes from whole blood. Biomed. Microdev. 13, 565-571.

[11] Zheng, Y., Wen, J., Nguyen, J., Cachia, M.A., Wang, C., Sun, Y. 2015. Decreased deformability of lymphocytes in chronic lymphocytic leukemia. Sci. Rep. 5, 7613.

[12] Qu, X., Li, M., Zhang, H., Lin, C., Wang, F., Xiao, M., Zhou, Y., Shi, J., Aldalbahi A., Pei, H., Chen, H., Li, L. 2017. Real-time continuous identification of greenhouse plant pathogens based on recyclable microfluidic bioassay system. ACS Appl. Mater. Interfaces 9, 31568-31575.

[13] Qu, X., Xiao, M., Li, F., Lai, W., Li, L., Zhou, Y., Lin, C., Li, Q., Ge, Z., Wen, Y., Pei, H., Liu, G. 2018. Framework nucleic acid-mediated pull-down microRNA detection with hybridization chain reaction amplification. ACS Appl. Bio Mater. 1, 859-864.

[14] Qi, L., Xiao, M., Wang, X., Wang, C., Wang, L., Song, S., Qu, X., Li, L., Shi, J., Pei, H. 2017. DNA-encoded Raman-active anisotropic nanoparticles for microRNA detection. Anal. Chem. 89, 9850-9856.

[15] Ulep, T.-H., Yoon, J.-Y. 2018. Challenges in paper-based fluorogenic optical sensing with smartphones. Nano Converg. 5, 14.

[16] Chung, S., Breshears, L.E., Perea, S., Morrison, C.M., Betancourt, W.Q., Reynolds, K.A., Yoon, J.-Y. 2019. Smartphone-based paper microfluidic particulometry of norovirus from environmental water samples at the single copy level. ACS Omega, 4, 11180-11188.

[17] Klug, K.E., Reynolds, K.A., Yoon, J.-Y. 2018. A capillary flow dynamics-based sensing modality for direct environmental pathogen monitoring. Chem. Eur. J. 24, 6025-6029.

[18] Chung, S., Jennings, C.M., Yoon, J.-Y. 2019. Distance vs. capillary flow dynamics-based detection methods on a microfluidic paper-based analytical device (μPAD). Chem. Eur. J. 25, 13070-13077.

[19] Uhrmacher, S., Schmidt, C., Erdfelder, F., Poll-Wolbeck, S.J., Gehrke, I., Hallek, M., Kreuzer, K.-A. 2011. Use of the receptor tyrosine kinase-like orphan receptor 1 (ROR1) as a diagnostic tool in chronic lymphocytic leukemia (CLL). Leukemia Res. 35, 1360-1366.

[20] Aghebati-Maleki, L., Shabani, M., Baradaran, B., Motallebnezhad, M., Majidi, J., Yousefi, M. 2017. Receptor tyrosine kinase-like orphan receptor 1 (ROR-1): An emerging target for

diagnosis and therapy of chronic lymphocytic leukemia. Biomed. Pharmacother. 88, 814–822.

[21] Daneshmanesh, A.H., Porwit, A., Hojjat-Farsangi, M., Jeddi-Tehrani, M., Tamm, K.P., Grandér, D., Lehmann, S., Norin, S., Shokri, F., Rabbani, H., Mellstedt, H., Österborg, A. 2013. Orphan receptor tyrosine kinases ROR1 and ROR2 in hematological malignancies. Leukemia Lymphoma 54, 843-850.

[22] Yu, J., Chen, L., Hasan, M.K., Ghia, E.M., Zhang L., Wu, R., Rassenti, L.Z., Widhopf, G.F., Shen, Z., Briggs, S.P., Kipps, T.J. 2017. Wnt5a induces ROR1 to associate with 14-3-3ζ for enhanced chemotaxis and proliferation of chronic lymphocytic leukemia cells. Leukemia 31, 2608-2614.

[23] Herlein, E., Beckwith, K.A., Lozanski, G., Chen, T.L., Towns, W.H., Johnson, A.J., Lehman, A., Ruppert, A.S., Bolon, B., Andritsos, L., Lozanski, A., Rassenti, L., Zhao, W., Jarvinen, T.M., Senter, L., Croce, C.M., Symer, D.E., Chapelle, A. Heerema, N.A., Byrd, J.C. 2013. Characterization of a new chronic lymphocytic leukemia cell line for mechanistic in vitro and in vivo studies relevant to disease. PLoS ONE 8, e76607.

[24] Zhang, S., Chen, L., Wang-Rodriguez, J., Zhang, L., Cui, B., Frankel, W., Wu, R., Kipps, T.J. 2012. The onco-embryonic antigen ROR1 is expressed by a variety of human cancers. Am. J. Pathol. 181, 1903-1910.

[25] Yamaguchi, T., Yanagisawa, K., Sugiyama, R., Hosono, Y., Shimada, Y., Arima, C., Kato, S., Tomida, S., Suzuki, M., Osada, H., Takahashi, T. 2012. NKX2-1/TITF1/TTF-1-induced ROR1 is required to sustain EGFR survival signaling in lung adenocarcinoma. Cancer Cell 21, 348-361.

[26] Abcam, 2015. Cell Culture Guidelines. Abcam, Cambridge. <https://www.abcam.com/ps/pdf/protocols/cell_culture.pdf> (accessed 07-Sep-2019).

[27] Molday, R.S., Dreyer, W.J., Rembaum, A., Yen, S.P. 1975. New immunolatex spheres: visual markers of antigens on lymphocytes for scanning electron microscopy. J. Cell. Biol. 64, 75-88.

[28] Roy, D., 2009. AUTO CONTRAST - Automatic Adjustment of Contrast of Images, version 1.1.0.0. MathWorks, Natick. <https://www.mathworks.com/matlabcentral/fileexchange/10566-auto-contrast> (accessed 07-Sep-2019).

[29] MathWorks, 2019. chromadapt - Adjust Color Balance of RGB Image with Chromatic Adaptation. <https://www.mathworks.com/help/images/ref/chromadapt.html> (accessed 07-Sep-2019).

[30] Merrill, E.W. 1969. Rheology of blood. Physiol. Rev. 49, 863-888.

[31] Kim, S., Cho, Y.I., Jeon, A.H., Hogenauer, B., Kensey, K.R., 2000. A new method for blood viscosity measurement. J. Non-Newtonian Fluid Mech. 94, 47-56.

[32] Sweeney, R.E., Nguyen, V., Alouidor, B., Budiman, E., Wong, R.K., Yoon, J.-Y. 2019. Flow rate and Raspberry Pi-based paper microfluidic blood coagulation assay device. IEEE Sens. J. 19, 4743-4751.

[33] Gasperino, D., Baughman, T., Hsieh, H.V., Bell, D., Weigl, B.H. 2018. Improving lateral flow assay performance using computational modeling. Annu. Rev. Anal. Chem. 11, 219-244.

[34] Persson, S.U., Gustavsson, C.G., Larsson, H., Persson, S. 1991. Studies on blood rheology in patients with primary pulmonary hypertension. Angiology 42, 836-842.

Supplementary

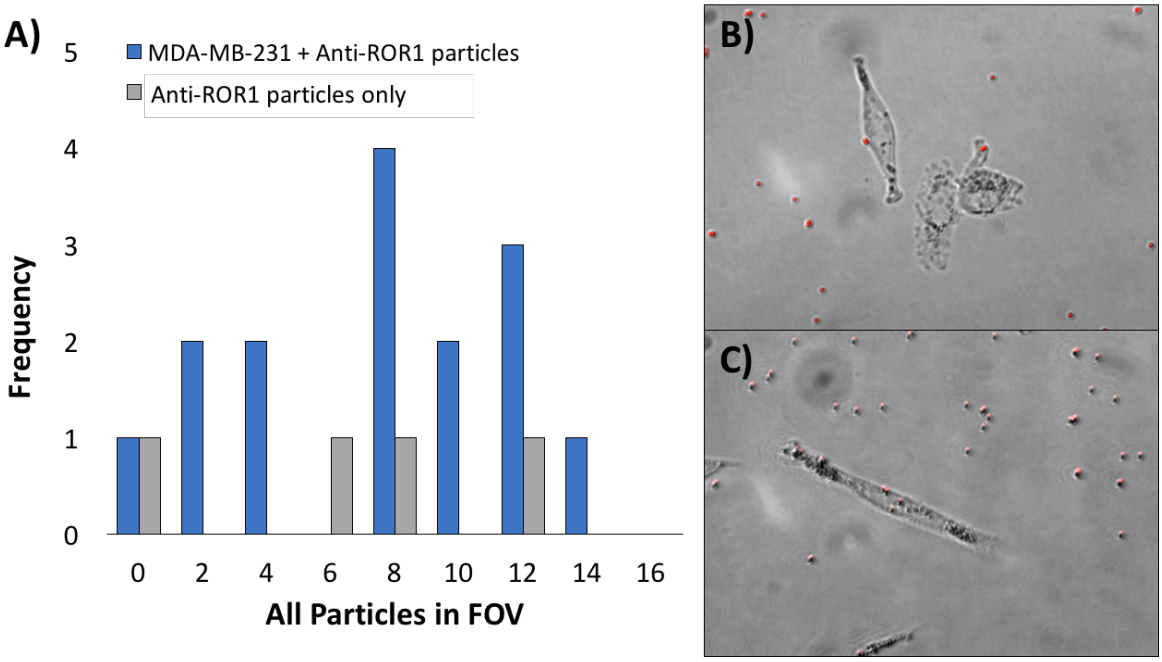

Supplementary Figure B-S1. A) Frequency tally of total particles in FOV with and without the presence of MDA-MB-231. B and C) Light and fluorescent microscope augmented images (400X) of fixed MDA-MB-231 cells with Anti-ROR1 red fluorescent particles attached to both whole cells and antigens.

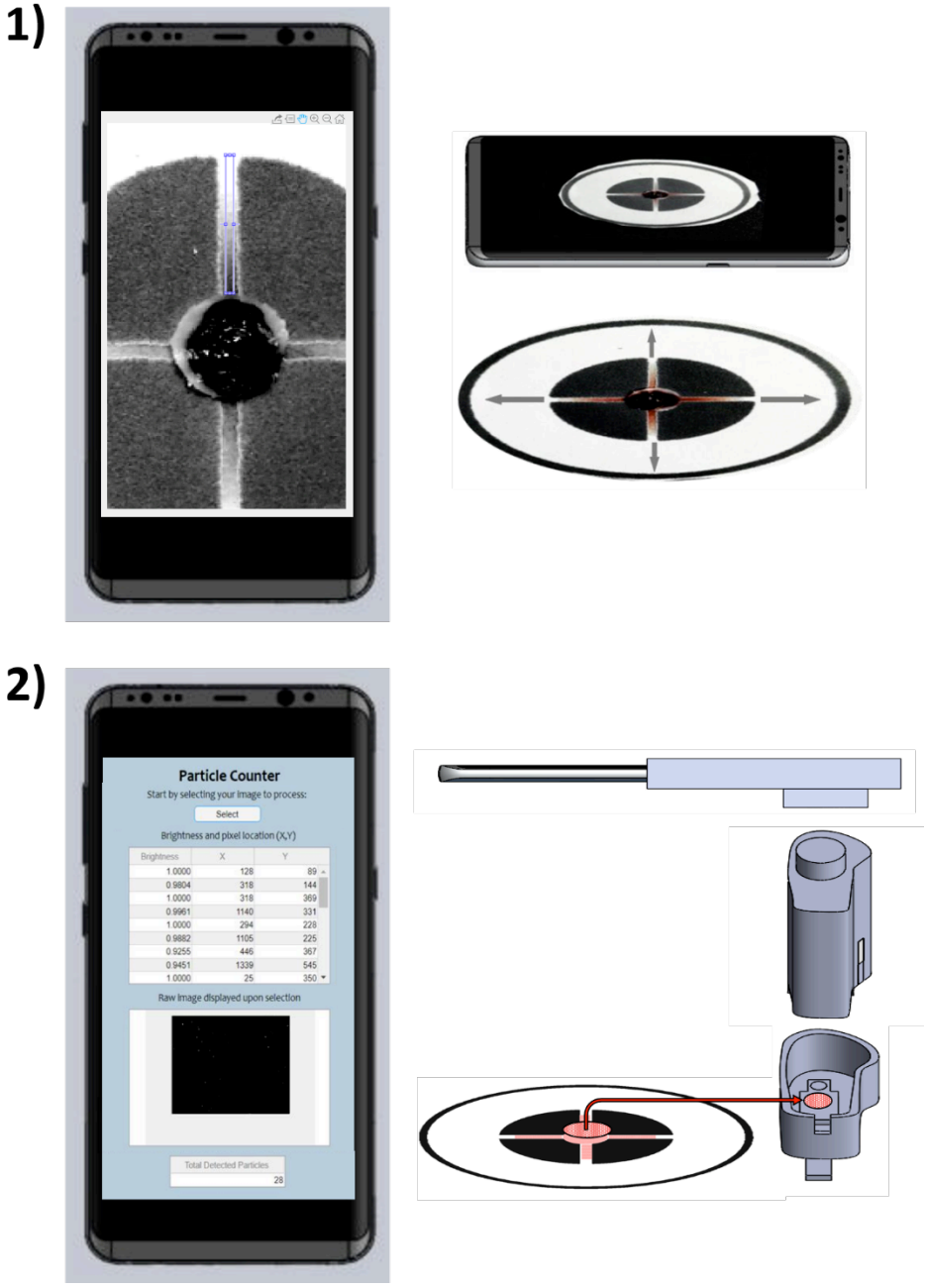

Supplementary Figure B-S2. Smartphone MATLAB Mobile apps for measuring the capillary flow velocities (1) and particle counts (2). Users will pipette the buffy coat blood sample to the top capture layer, and captures a video from its top using a smartphone without the microscope attachment. The MATLAB app will analyze the flow velocities from four different channels of the bottom flow layer at the optimized time window (13 to 22 s). After that, the top capture layer

will be separated and placed within the microscope stage. Another MATLAB app will analyze the fluorescence microscopic images and provide the particle counts as its output.

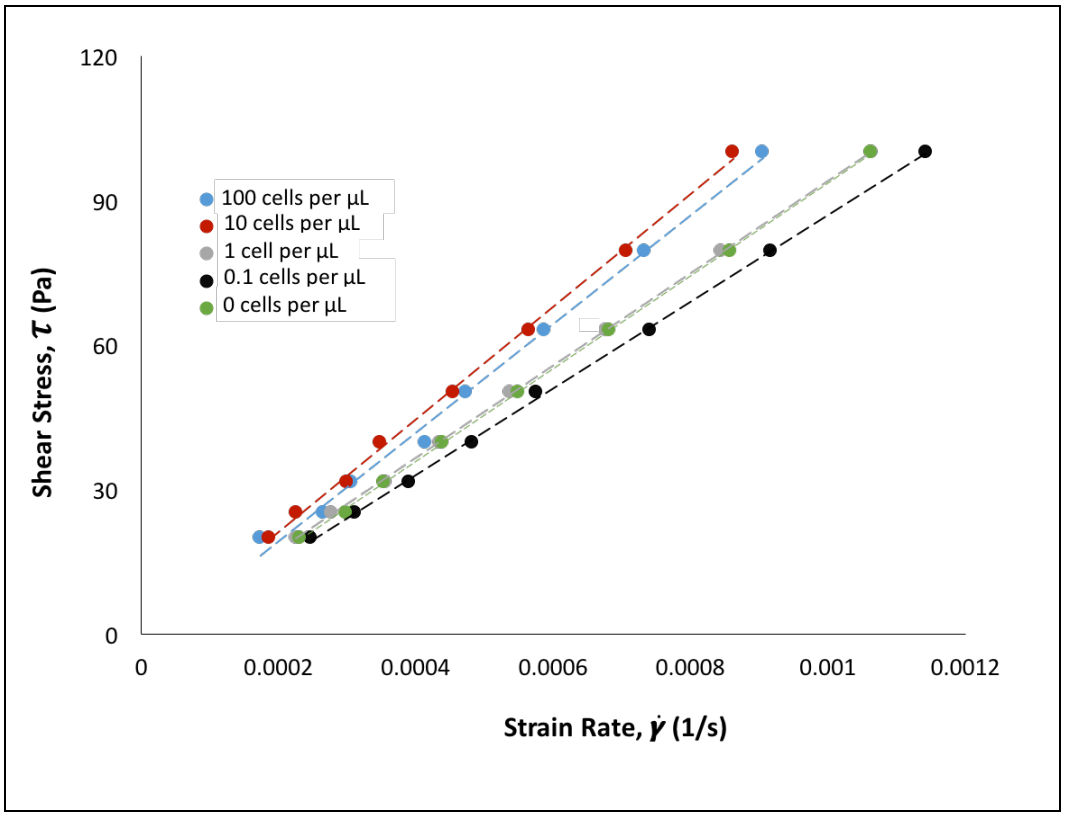

Supplementary Figure B-S3. Cone-plate rheology shear stress (τ) and strain rate ($\dot{\gamma}$) measurements of buffy coat dosed with 0 to 100 cells per µL

APPENDIX C

EMULSION NUCLEIC ACID AMPLIFICATION FOR BACTERIAL IDENTIFICATION VIA ANGLE-DEPENDENT LIGHT SCATTER ANALYSIS

Tiffany-Heather Ulep[1]*, Alexander S. Day[1]*, Elizabeth Budiman[1], Laurel Dieckhaus[1], Babak Safavinia[1], and Jeong-Yeol Yoon[1]**

[1]Department of Biomedical Engineering, The University of Arizona, Tucson, Arizona 85721, United States

*Co-first author, **Corresponding author E-mail: jyyoon@email.arizona.edu

Abstract

An emulsion loop-mediated isothermal amplification (LAMP) platform was investigated to determine the relation between angle-dependent light scatter intensity (based off Mie scatter theory) and nucleic acid amplification progression and concentration dependencies. The phenomenon attributing to changes in light scatter intensities is due to the interfacial changes occurring in the emulsion droplets, where increasing amplicon adsorption causes a decrease in interfacial tension (IFT), resulting in smaller diameter emulsions. Light microscope images confirmed there is a 43.6% size difference in emulsion diameters for mixtures with and without DNA fragment present. Mie scatter simulations further confirmed that light scatter intensity is diameter dependent. Smaller diameter emulsions will have lower intensity values than larger diameter emulsions. Using spectrophotometers and fiber optic cables placed at 30° and 60° light scatter intensity was monitored. Light scatter intensity profiles collected for 3 min at 30° are able to statistically differentiate 10^3 and 10^6 copies per μL initial concentrations in comparison to NTC (0 copies per μL). Similarly, 3 min light scatter intensities collected at 60° were able to statistically differentiate 10^6 per μL initial concentrations in comparison to NTC. Furthermore, control experiments were conducted to validate nucleic acid detection versus protein adsorption and found 30° light scatter intensity can be used to quantify protein adsorption (bacteria concentration), while 60° light scatter intensity can be used to quantify nucleic acid presence. Overall, we have demonstrated the use of angle-dependent light scatter intensity as a means of real-time monitoring of an emulsion LAMP platform and fabricated a smartphone-based monitoring system that showed similar trends as spectrophotometer light scatter data, thus validating the technology for a user-friendly field deployable platform.

Introduction

Nucleic acid amplification is a gold standard tool for the identification of target genes-of-interest. Polymerase chain reaction (PCR) is the most used nucleic acid amplification technique which utilizes cyclic temperatures to denature, anneal, and extend in order to create linear copies of the target gene-of-interest in an exponential amount[1]. However, PCR along with other traditional nucleic acid amplification techniques can be limited due to the requirement of pre-processing samples to extract and purify its DNA/RNA.

In an effort to monitor in real-time the amplification of PCR reactions, quantitative PCR (qPCR) is also a widely used technology. Fluorescent intercalating dyes that have high a high affinity to nucleic acids by embedding between base pairs are utilized and monitored to get exponential curves, such as ethidium bromide and SYBR® Green[2]. Although, such intercalating dyes can result in non-specific signals because it is non-specific to specific gene-of-interest, but all double stranded DNA (dsDNA). To address this problem, fluorescently tagged hybridization probes that are complementary oligonucleotide sequences to the target gene-of-interest can be utilized[3–5]. Such probes result in fluorescent signals that are specific to the amplification of the target gene sequence rather than non-specific amplification (i.e. primer dimerization). A limitation to fluorescent probes are they are custom-made and expensive.

Emulsion platforms can be utilized to address the problem of background signals due to non-specific amplification. Water-in-oil emulsion protocols are advantageous in nucleic acid amplification techniques due to the ability to compartmentalize target-gene-of-interest into individual containment units. This allows for an intrinsic separation mechanism of components that may inhibit amplification or induce non-specific amplification[6]. Emulsions can be especially advantageous due to the intrinsic presence of surfactants and agitation during their formation that could be utilized as an alternative method of “extracting” DNA/RNA.

Isothermal nucleic acid amplification techniques have gained interest in previous years due to the attractiveness of utilizing a single temperature. A constant temperature for nucleic acid amplification mitigates the need for specialized equipment such as thermocyclers to finely and rapidly adjust temperatures in an intricate manner like in PCR reactions. This aspect has been especially appealing for field-deployable, point-of-care platforms, where simplicity is necessary. However, it is notoriously known that isothermal nucleic acid amplification techniques are susceptible to nonspecific amplification, rendering in less sensitive than PCR methods[7].

Alternative methods of measuring nucleic acid amplification can be conducted by measuring the interfacial tension changes of the aqueous nucleic acid amplification reaction. Harshman et al., utilized a moving droplet-on-a-thermocouple PCR instrumentation to amplify targets-of-interest and monitor its progression in real-time by measuring the droplet size. The phenomenon attributing such change in droplet size was due to a decrease in the water-oil interface, rendering the droplet unstable as amplicon amount increased within[8]. Similarly, a droplet loop-mediated isothermal amplification (LAMP) nucleic acid method was utilized for monitoring amplification progression via interfacial-effect detection. The platform was comprised of a static, aqueous LAMP droplet immersed in mineral oil, in which the change in contact angle was monitored over time and related to interfacial tension[9]. In both platforms, time-to-results were reduced immensely in comparison to conventional nucleic acid amplification techniques and showed significant amplification in complex sample matrices due to inhibition relief at the water-oil interface.

In this paper, we focus specifically on LAMP in a water-oil emulsion platform to address non-specific signals. We also utilize interfacial effect-based monitoring to achieve rapid time-to-results. The mechanism in which we will monitor in real-time the effects of amplification is based on the interfacial changes of micron size emulsions due to amplicon adsorption, followed

by emulsion destabilization[10]. Based on Mie scatter theories, which relate angle-dependent light scatter intensity in relation to particle size, we can monitor LAMP reactions progression. Specifically, *rfbe* gene in *E. coli* were amplified via emulsion LAMP at varying concentrations of 10^6, 10^3, 1, and 0 CFU per μL. Firstly, the proposed detection mechanism was validated with spectrophotometers and fiber optic cables. Secondly, a smartphone camera with blinking LED set up was used and resulted in similar light scatter intensity measurements and correlation to LAMP reaction progression as the spectrophotometer set up. Light scatter intensity showed to decrease in relation to amount of initial target concentration within 3 min of emulsion LAMP reaction for both detection set ups. Furthermore, control experiments were conducted to validate nucleic acid detection versus protein adsorption and found 30° light scatter intensity can be used to quantify protein adsorption (bacteria concentration), while 60° light scatter intensity can be used to quantify nucleic acid presence. Overall, we have demonstrated the use of angle-dependent light scatter intensity as a means of real-time monitoring of isothermal nucleic acid amplification in a simple and user-friendly platform.

Materials and Methods

LAMP reaction: *Escherichia coli* O157:H7 (part #0801622; ZeptoMetrix) target stock bacterial solution was diluted to different concentrations of 10^6, 10^3, 1, 0.1, and 0 CFU μL^{-1} in nuclease free water. LAMP primers were used from literature[11] and purchased from Sigma-Aldrich (St. Louis, MO, USA). 10X target-specific primer sets were formulated to contain 16 μM each of FIP and BIP primers, 8 μM each of Loop-F and Loop-B primers, and 2 μM of F3 and B3 primers. LAMP reactions were prepared on iced and utilized the WarmStart® LAMP Kit DNA & RNA (E1700; New England Biolabs Inc, Ipswich, MA, USA). Final mixtures were comprised of *Bst* 2.0 WarmStart DNA Polymerase and WarmStart RTx Reverse Transcriptase in manufacturer's

optimized LAMP buffer solution. The LAMP final mixture contained 5:1:0.4:1:2.6 ratio of Warm Start LAMP 2X master mix, 10X primer mix, target bacteria dilution (or nuclease-free water for no target control, NTC), 20 mg/mL bovine serum albumin (B8667; Sigma), and nuclease-free water. Conventionally amplified samples were conducted in a thermocycler (MJ Research, Waltham, MA, USA) programmed for 65°C for 30 min, followed by refrigeration at 4°C.

Interfacial tension (IFT) measurements: Interfacial tension (mN m^{-1}) measurements were made with an FTÅ200 contact analyzer (First Ten Ångstroms, Portsmouth, VA, USA) using the pendant droplet method. Conventionally amplified LAMP reactions with assay times of 0, 5, 10, and 15 min were extruded from an 18-gauge blunt needle (outer diameter = 1.27 mm) and measured after the pendant droplet had been hanging for 30 s.

Light scatter detection: An incident light of 650 nm (LS-450 LED; Ocean Optics) illuminated emulsion samples via fiber optical cable, while 3 fiber optical cables connected to a spectrophotometer (USB4000, Ocean Optics) placed at 30°, 60°, and 90° collected light intensity. Light scatter intensity measurements were collected every 3s or 1.5s. A 3D printed attachment[10] was used to secure optical instrumentation and vial with emulsion reaction throughout assay.

Conventionally amplified emulsion light scatter detection and diameter measurement: 10 μL conventionally amplified LAMP reactions with assay times of 0, 5, 10, and 20 min were placed into pre-heated 65°C oil phase with a 650 nm incident light illuminating on sample. At the 60° angle, bulk light scatter was collected via fiber optic cable and spectrophotometer. 10 μL

of the emulsion was also collected at 1 min, when sufficient emulsion formation was succeeded. Microscope images were then post-processed and measured in ImageJ software (US National Institutes of Health; Bethesda, MD, USA).

Mie scatter simulations: Mie scattering simulations were performed using MiePlot v4.6 (Phlip Laven, www.philiplaven.com/mieplot.htm). The simulation assumed a refractive index of sample medium (mineral oil) = 1.47, refractive index of emulsions (water) = 1.33, a 650 nm incident light, and particle sizes varying from 9.42 μm to 0.42 μm. Light intensity at 30°, 60°, and 90° angles were investigated.

Emulsion LAMP assay: Water-in-oil colloidal emulsions were prepared in a similar fashion as a published method[10]. A single emulsion reaction consisted of the addition of a 10 μL aqueous LAMP droplet from a blunt end needle tip suspended and dropped uniformly into 2 mL of preheated 65°C oil phase. Emulsions were formed and agitated by a micro stir bar set to 1500 rotations per minute for 30 min. Post-reaction, emulsions were collected and byproducts were extracted via 3 iterations of water saturated diethyl ether[12].

End-point amplification analysis of emulsions: *Spectroscopy:* After emulsions assay was performed then broken, the amplicon precipitate dissolved in an aqueous solution was analyzed. Presence of nucleic acid was determined by measurement of absorption at 260 nm. *Gel electrophoresis:* LAMP products were analyzed using gel electrophoresis. 3% w/v agarose gel (A0169; Sigma) in 1X Tris-acetate-EDTA (TAE) buffer (35100131; Quality Biological Inc, Gaithersburg, MD, USA) was prepared and placed at 120 V for 50 min with an electrophoresis power supply (Fischer Scientific; FB200). TrackIt™ 100 bp DNA ladder was used as a standard

for fragment sizing. Gels were stained with ethidium bromide (E1510; Sigma) and imaged under UV light. Gel images were analyzed using ImageJ software (U.S. National Institutes of Health).

Results and Discussion

Interfacial Tension: Conventionally amplified LAMP reactions with assay times of 0, 5, 10, and 20 min were used to measure interfacial tension (IFT) with various DNA amounts. 10 μL samples were measured for IFT via pendant droplet analysis. As seen in Figure 1A, the overall trend is that with increasing amount of DNA fragment mixture there is a decreasing trend in IFT. IFT measurements were 39.39 mN/m for 0 min LAMP assay time, 39.16 mN/m for 5 min, 37.28 mN/m for 10 min, and 36.92 mN/m for 20 min. Essentially, decreasing IFT measurements with respect to amount of DNA is quantifying the stability of the droplet. As more DNA is present, the overall droplet's surface tension is destabilizing due to the amplicon adsorption at the outer surface area of the hanging pendant droplet. This overarching phenomenon will be used as the means in which we justify the detection method in our emulsion platform.

Mie light scatter simulation in relation to varying emulsion diameter: Within our emulsion are micron size aqueous droplets (confirmed from light microscope images suspended in a mineral oil and surfactant mixture). As seen in the previous section, the presence of DNA causes the destabilization of a droplet. Emulsions are a dynamic system with continuous agitation from a micro stir bar. Therefore, we expect that with increasing amount of DNA fragment mixture, the diameter size distribution of emulsions will decrease. The method in which real-time change in diameter size is monitored is by collecting the bulk light scatter at various angles or angularly resolved light scattering with respect to an incident light. Based off the Mie Theory, angularly resolved light scatter off a particle gives information to the overall size characteristics of the

particle sample[13]. The intensity of light scattered off a particle distribution in relation to various diameters (9.42 µm to 0.42 µm) at 30°, 60°, and 90° were simulated to model the decreasing diameter size due to increasing presence of DNA amplicons that would be produced in an emulsion LAMP reaction. As seen in Figure 1B, light intensity decreases as diameter size of emulsions decrease for all 3 angles. The simulation also showed that 30° light scatter had higher intensity values, followed by 60°, then 90°.

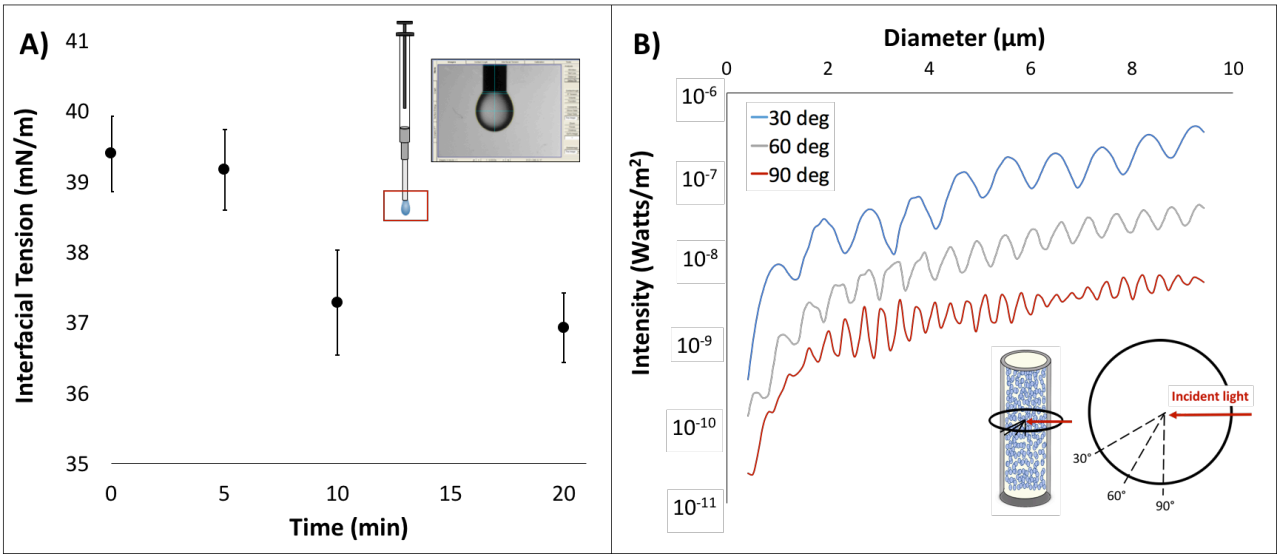

Figure C-1 A) Interfacial tension (IFT) measurements in relation to amount of amplicons present at 0, 5, 10, and 20 min of conventional amplification of LAMP reactions via pendant droplet analysis. B) Mie scatter simulation of light scatter intensity of a homogeneous particle distribution in relation to diameter size at 30°, 60°, and 90° with respect to a 650 nm incident light.

Varying LAMP amplicon amount in emulsion platform: As a model sample matrix to simulate LAMP amplicon production conventionally amplified LAMP reactions with assay time

of 0, 5, 10 , and 20 min were used to determine diameter size and light scatter intensity in relation to concentration of DNA present in the emulsion platform. Figure 2A shows the diameter distribution between an emulsion sample with various amounts of DNA fragment mixture in the emulsion platform after 1 min of agitation. The average diameter size for emulsion was 55.57 pixels at 0 min of assay time, 51.43 pixels at 5 min, 18.11 pixels at 10 min, and 21.32 pixels at 20 min. This resulted in a maximum difference of 67.4% and was statistically different between 0 min assay time in comparison to 10 and 20 min conventional amplification assay time. Therefore, due to the presence of DNA, emulsion diameter size is decreased due to decreased interfacial tension at the oil water interface rendering unstable emulsions, resulting in smaller diameters.

As demonstrated previously, light scatter, supported by the Mie theory, will change in intensity due to size dependencies. In Figure 2B, light scatter intensity at 60° for conventionally amplified LAMP reactions with assay times of 0, 5, 10, and 20 min was collected in relation to time in emulsion platform. Light scatter intensity at 60° of applied nuclease-free water was also collected in the emulsion platform over time, showing lowest initial intensity in comparison to LAMP reactions (Supplementary Figure 1). Within the first 30 s, light scatter intensity at 30 s in relation to concentration of DNA amount (based on conventional LAMP assay time) shows a linear relationship ($R^2 = 0.976$). The percentage change between no DNA fragment mixture (nuclease-free water). This linear relationship is further refined at 1 min. Light scatter intensity collected at 1 min in relation to conventional LAMP assay time had an R^2 vale of 0.976 (Figure 2C). It can then be alluded, that the decrease in intensity is due to an increase amount of amplicon product due to a decrease distribution of emulsion diameter size.

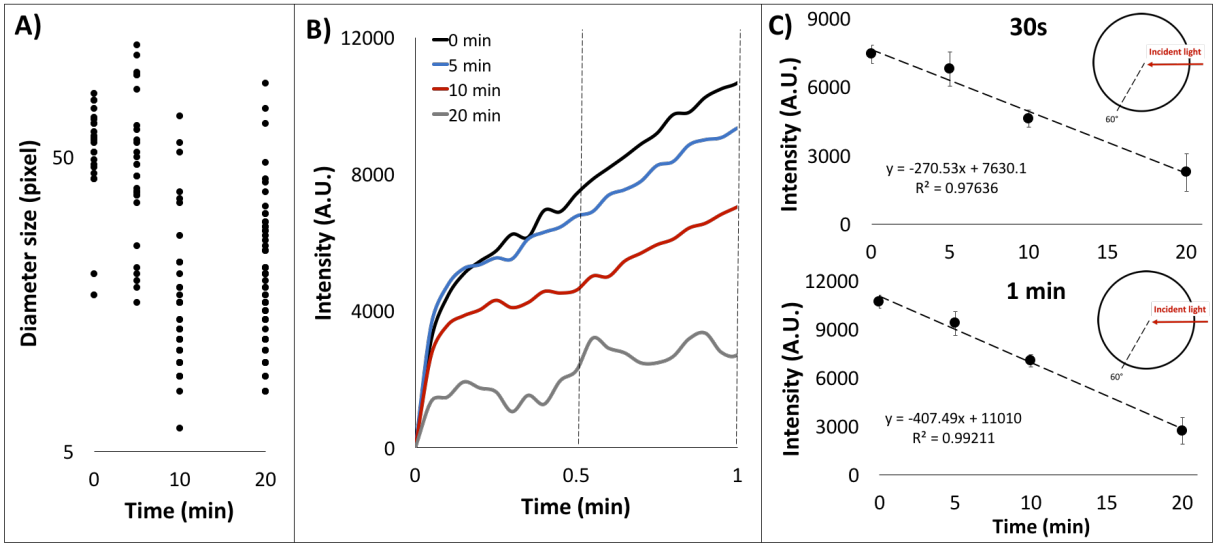

Figure C-2. A) Measured diameter from light microscope images of water-oil emulsions containing 10 uL conventionally amplified LAMP reaction with assay time of 0, 5, 10, and 20 min. B) Emulsion light scatter intensity at 60° with respect to 650 nm incident light over time of conventionally amplified LAMP reaction with assay time of 0, 5, 10, and 20 min. C) 60° Light scatter intensity in relation to conventional LAMP assay time at top: 30s and bottom: 1 min.

Angle-dependent light scatter collection via spectrophotometer: Light scatter intensity from fiber optic cables placed at 30°, 60°, and 90° angles with respect to a 650 nm incident light was collected from a spectrophotometer of emulsion samples with LAMP reactions containing initial bacteria concentrations of 10^6, 10^3, 1, and 0 copies per µL. For all 3 angles the underlying trend was that light scatter intensity decreased with increasing concentration. This trend is synonymous to trends found with light scatter of emulsions containing varying concentration of DNA fragment mixture. Light scatter intensities collected at the 30° angle showed the greatest difference in change in comparison to NTC (0 copies per µL) for 10^6 and 10^3 copies per µL. The greatest percent change in light scatter intensity appeared to be 69.7% within 3 minutes on the

emulsion platform between 0 and 10^3 copies per µL. 60° light scatter intensities at different initial bacteria concentration did not show significant differences other than 10^6 copies per µL. Light scatter intensity at 3 min shows a 20.63% intensity fluctuation amongst 0 to 10^3 copies per µL concentrations, followed by a significantly different 79.32% intensity change in comparison to NTC for 10^6 copies per µL.

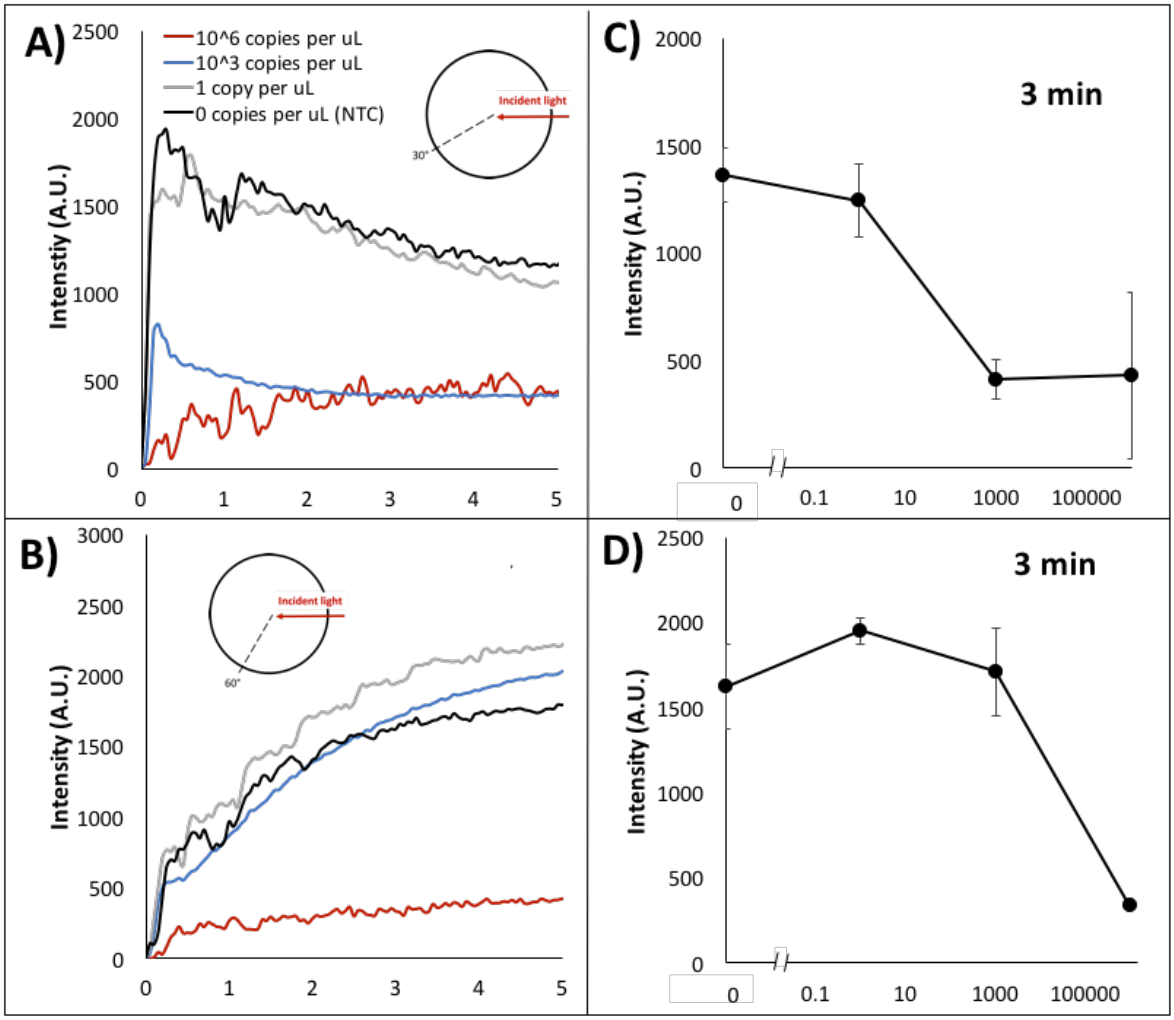

Figure C-3. Emulsion LAMP Light scatter intensity via spectrophotometer over time at A) 30° and B) 60° angle with respect to 650 nm incident wavelength with varying initial bacteria

concentration of 10^6, 10^3, 1, and 0 copies per μL. Light scatter intensity at 3 min for C) 30° and E) 60° angle for bacteria concentrations of 10^6, 10^3, 1, and 0 copies per μL.

Emulsion light scatter intensity in relation to bacteria concentration with no LAMP reagents: Control experiments were conducted on the emulsion platform with the addition of 10 μL aqueous solutions containing diluted bacteria concentrations of 10^6, 10^3, 1, and 0 copies per μL with bovine serum albumin (BSA) as a stabilizer. Bacteria solutions with no LAMP reagents were used to investigate light scatter changes due to initial adsorption of bacteria cells/fragments adsorption rather than nucleic acid amplification. Light scatter intensities were collected at 60° over time for four different bacteria concentrations (Figure 4A). Light scatter intensities at 3 min are shown in relation to concentration of bacteria solution added to the emulsion platform. Overall there is no significant trends, resulting in only a maximum difference in comparison to 0 CFU per μL of 37.29%. Since there is no significant concentration dependent light scatter intensity trends these control experiments results in the assumption that light scatter collected at 60° angle can be used to determine nucleic acid dependencies rather than initial bacteria adsorption.

Utilizing the same emulsion samples, 30° light scatter intensities were also collected over time (Figure C) and plotted in relation to bacteria concentration at 3 min. Unlike the 60° light scatter intensities at 3 min, there was a concentration dependency. The maximum percent change difference in light scatter intensities was observed between 1 CFU per μL and 1000 CFU per μL at 55.53% at 3 min (Figure D). Therefore, we can conclude that the decrease change in intensity

observed in previous emulsion LAMP reactions at 30° was due to bacteria adsorption and not amplicon presence. In comparison, since light scatter change in intensity collected at 60° did not significantly change in relation to bacteria concentration, 60° angle should be used to monitor nucleic acid amplification.

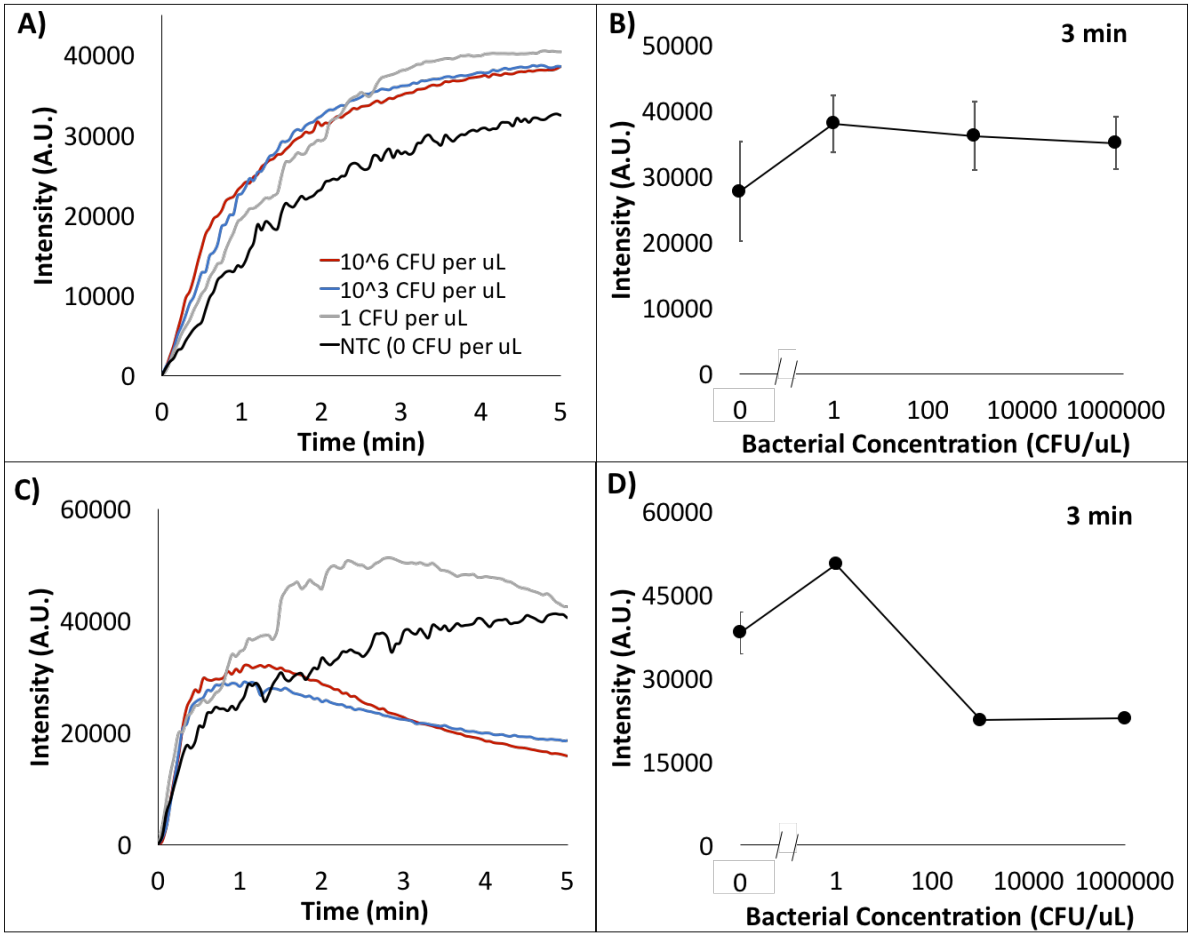

Figure C-4. A) Emulsion, no amplification light scatter intensity with relation to time collected at 60° angle with respect to a 650 nm wavelength incident light with diluted bacteria and BSA droplets varying concentrations of 10^6, 10^3, 1, and 0 copies per µL. B) Light scatter intensity at 3 min collected from 60° angle at 3 min.

Angle-dependent light scatter collection via smartphone camera: A 3D printed hot plate attachment was designed and fabricated to hold the emulsion reaction chamber and house 2 blinking red LEDs placed at 30° and 60° angles with respect to a smartphone camera. 10 μL LAMP reactions with varying initial bacteria concentrations of 10^6, 10^3, 1, and 0 copies per μL were placed into the emulsion platform in a similar fashion as the spectrophotometer procedure. Images were taken every 3s synced to the differently angled LEDs over the course of 15 min to characterize smartphone optical detection as replacement for a spectrophotometer and fiber optical cable experimental set up for a more user-friendly platform. Red Channel intensity in the captured images were extracted and sorted from time-lapsed image sequence for both angles (Figure 5A and 5B). Intensity from these curves were taken in relation to concentration of initial target concentration at 3 min and 6 min. Similar trends were found for both angles, as initial target concentration increased, intensity decreased. 30° light scatter intensity at 3 and 6 min showed a 96.29% and 131.4% change in intensity between NTC and 10^6 copies per μL (Figure 5C and 5D). 60° light scatter intensity at 3 and 6 min showed a 93.80% and 102.3% change in intensity between NTC and 10^6 copies per μL (Figure 5E and 5F).

Interestingly, the percent changes in intensities in comparison to NTC across bacteria concentration collected via smartphone camera were larger in comparison to intensities collected via spectrophotometer. This could be due the ability to resolve outlier reactions based off of image observations. For example, a reaction was omitted from the data set when a large bubble was accidentally introduced into the emulsion. Such omission could not be conducted on a spectrophotometer set up because there are no images to confirm such event. However, disadvantages to utilizing a smartphone to capture light scatter intensities via time-lapse is it is not conducted in a real-time fashion. Images must be taken from the smartphone, uploaded, and

processed via an automated Python script. Next steps to address this concern is rather than a smartphone as the optical transducer, a microcontroller camera connected to a smartphone user interface could be designed as a standalone device.

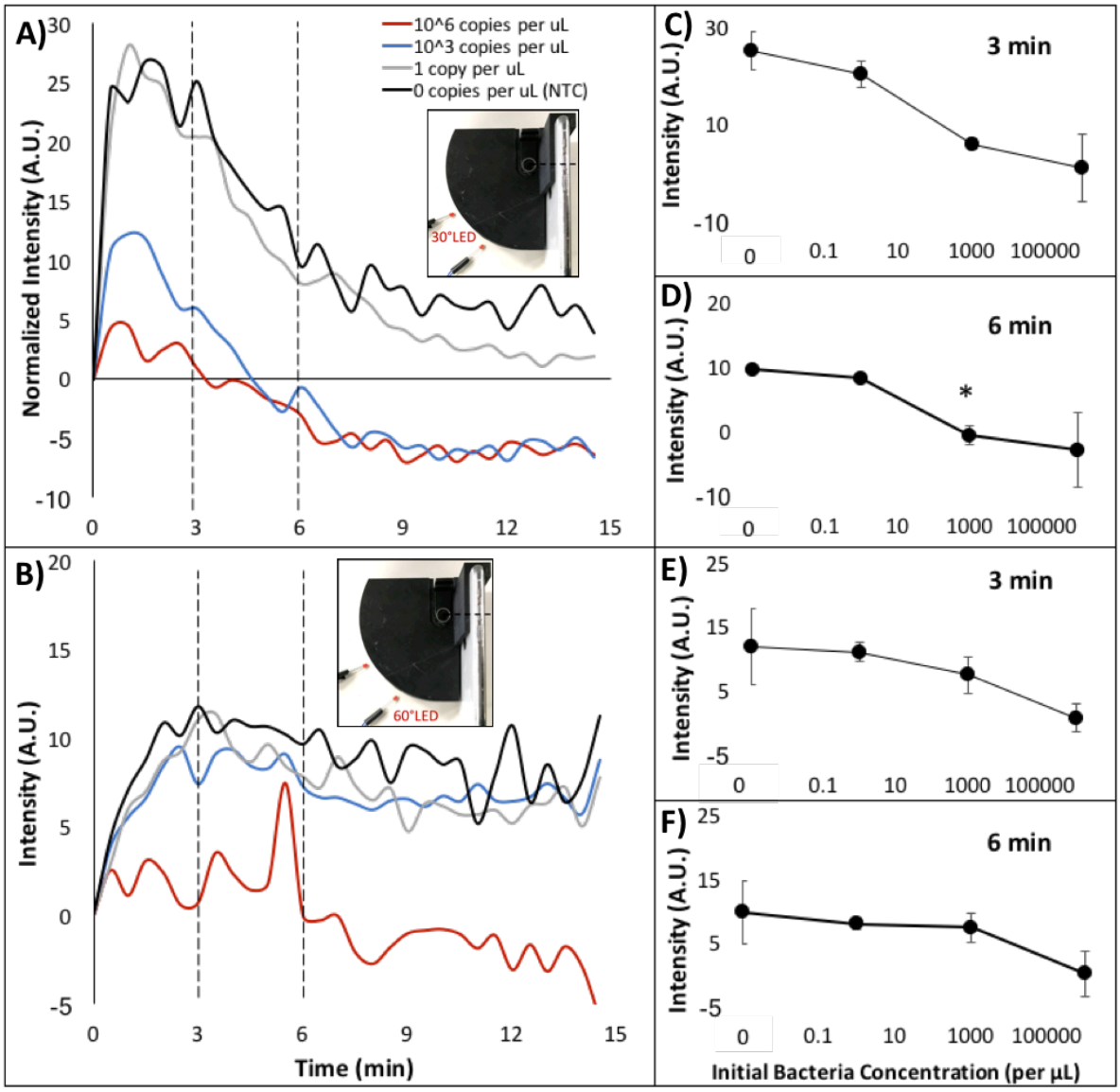

Figure C-5. Emulsion LAMP Light scatter intensity via smartphone camera over time at A) 30° and B) 60° angle with respect to 650 nm incident wavelength with varying initial bacteria concentration of 10^6, 10^3, 1, and 0 copies per µL. 30° light scatter red channel intensity at C) 3

min and D) 6 min. 60° light scatter red channel intensity at E) 3 min and F) 6 min with bacteria concentrations of 10^6, 10^3, 1, and 0 copies per μL.

Conclusion

An emulsion platform was investigated to determine angle-dependent light scatter's potential to monitor in real-time the amplification of nucleic acids in an isothermal state via LAMP reaction. The phenomenon to attribute to light scatter intensity changes due to amplicon presence was verified via pendant droplet analysis for the measurement of interfacial tension (IFT). IFT measurements showed that with added LAMP amplicon model samples (DNA fragment mixtures ranging from 100 to 2,000 bp) there is a decrease in IFT. Amplicon presence destabilizes aqueous droplets due to the increased molecules at the interface. Therefore, we can allude that in an emulsion platform, solutions with a larger amplicon presence will have a decreased droplet diameter distribution. This was confirmed via light microscope images where emulsions diameters with no amplicons (NTC or 0 μg DNA fragment mixture) were 43.6% smaller than emulsion diameters with amplicons (1 μg DNA fragment mixture).

Emulsions with the addition of various amounts of model amplicon solutions showed that angle-dependent light intensity at 60° decreases linearly in relation to increased amount of amplicons. Mie scatter simulations further confirmed that light scatter intensity is diameter dependent. Smaller diameter emulsions will have higher intensity values than larger diameter emulsions. LAMP emulsions with varying initial bacteria concentrations were performed while light scatter intensity at 30° and 60° were monitored in real time. Intensity light scatter values at 3 min showed similar trends to the light scatter experiments with DNA fragment mixture solutions. At 3 min, 30° light scatter intensity can statistically differentiate 10^3 and 10^6 copies per

μL initial concentrations in comparison to NTC (0 copies per μL). 6 min light scatter intensities collected at 60° can statistically differentiate 10^6 per μL initial concentrations in comparison to NTC (0 copies per μL).

As a control study to determine if light scatter changes were truly due to amplicon adsorption, solutions of varying bacteria concentrations with no LAMP reagents were placed into an emulsion and monitored for light scatter. 30°, 3 min light scatter data showed a maximum decrease in light scatter of 55.53% alluding to the detection of bacteria adsorption, not amplicon presence. In comparison 3 min, 60° light scatter intensities showed not distinguishable bacteria concentration dependencies, therefore the decrease in light scatter intensity at 60° was due to amplicon presence.

Furthermore, a 3D printed hot plate attachment with an emulsion reaction chamber, 2 blinking LEDs placed at 30° and 60°, and smartphone holder was designed and utilized to simplify the emulsion platform from spectrophotometers and fiber optical cables to a more user-friendly platform. Similar light scatter intensities were achieved for both angles and in comparison to spectrophotometer collected data, thus demonstrating translatability of emulsion LAMP detection technologies toward field-deployability in resource-limited or clinical settings.

Current challenges to address in platform is to increase the reproducibility so diagnostic outcomes due to light scatter changes are more robust under different conditions. This must be addressed since application setting/environment is intended for field-use. This was minimally introduced in this study since conditions varied such as use of bacteria samples that were stored over time for utilization as target samples, oil phase mixtures were prepared on the day of experiments by multiple different users, and application of droplet into the emulsion platform was done manually by different users. Results showed statistically significant trends regardless

of variations introduced in experimental set up, showing promising robustness. However, ways to increase reproducibility of the platform, by mitigating sample application variation, is the integration of an automated sample loading methodology such as a microfluidic pump or automated pipette to aspirate droplet into the emulsion in a controlled manner.

The platform is advantageous due to its inherent extraction of initial DNA in target sample from agitation (micro stir bar), surfactants in oil phase, and use of heat for denaturation of bacterial membrane. Therefore, the platform mechanism decreases the pre-processing and lysing required to amplify nucleic acid from patient samples. Future work would be to demonstrate the platform in a more complex sample matrix such as blood or urine patient samples collected for bacterial infection identification, as well as other target pathogenic bacteria.

Acknowledgements

The authors would like to thank Jokubas Ausra and Tyler Hertenstein for their experimental assistance. This work was supported by the Cardiovascular Biomedical Engineering Training Grant from U.S. National Institute of Health (Grant Number T32HL007955).

References

[1] PCR Basics, (n.d.). https://www.thermofisher.com/us/en/home/life-science/cloning/cloning-learning-center/invitrogen-school-of-molecular-biology/pcr-education/pcr-reagents-enzymes/pcr-basics.html (accessed November 12, 2019).

[2] SYBR® Green Based Quantitative PCR, Sigma-Aldrich. (n.d.). https://www.sigmaaldrich.com/life-science/molecular-biology/pcr/quantitative-pcr/sybr-green-based-qpcr.html (accessed November 11, 2019).

[3] V.A.J. Kempf, K. Trebesius, I.B. Autenrieth, Fluorescent In Situ Hybridization Allows Rapid Identification of Microorganisms in Blood Cultures, J. CLIN. MICROBIOL. 38 (2000) 9.

[4] K.J. Livak, S.J.A. Flood, J. Marmaro, W. Giusti, K. Deetz, System Useful for Detecting PCR Product, (n.d.) 7.

[5] R. Kubota, D.M. Jenkins, Real-time duplex applications of loop-mediated amplification (LAMP) by assimilating probes, Int. J. Mol. Sci. 16 (2015) 4786–4799. https://doi.org/10.3390/ijms16034786.

[6] M. Nakano, J. Komatsu, S. Matsuura, K. Takashima, S. Katsura, A. Mizuno, Single-molecule PCR using water-in-oil emulsion, Journal of Biotechnology. 102 (2003) 117–124. https://doi.org/10.1016/S0168-1656(03)00023-3.

[7] W. Deguo, H. Guicheng, W. Fugui, L. Yonggang, R. Daxi, Drawback of loop-mediated isothermal amplification, (n.d.) 4.

[8] D.K. Harshman, B.M. Rao, J.E. McLain, G.S. Watts, J.-Y. Yoon, Innovative qPCR using interfacial effects to enable low threshold cycle detection and inhibition relief, Sci Adv. 1 (2015) e1400061. https://doi.org/10.1126/sciadv.1400061.

[9] T.-H. Ulep, A.S. Day, K. Sosnowski, A. Shumaker, J.-Y. Yoon, Interfacial Effect-Based Quantification of Droplet Isothermal Nucleic Acid Amplification for Bacterial Infection, Sci Rep. 9 (2019) 9629. https://doi.org/10.1038/s41598-019-46028-8.

[10] A.M. Nicolini, T.D. Toth, S.Y. Kim, M.A. Mandel, D.W. Galbraith, J.-Y. Yoon, Mie scatter and interfacial tension based real-time quantification of colloidal emulsion nucleic acid amplification, Adv. Biosyst. 1 (2017) 1700098. https://doi.org/10.1002/adbi.201700098.

[11] X. Zhao, Y. Li, L. Wang, L. You, Z. Xu, L. Li, X. He, Y. Liu, J. Wang, L. Yang, Development and application of a loop-mediated isothermal amplification method on rapid detection Escherichia coli O157 strains from food samples, Mol. Biol. Rep. 37 (2010) 2183–2188. https://doi.org/10.1007/s11033-009-9700-6.

[12] R. Williams, S.G. Peisajovich, O.J. Miller, S. Magdassi, D.S. Tawfik, A.D. Griffiths, Amplification of complex gene libraries by emulsion PCR, Nature Methods. (2006). https://doi.org/10.1038/nmeth896.

[13] Q. Fu, W. Sun, Mie theory for light scattering by a spherical particle in an absorbing medium, Appl. Opt., AO. 40 (2001) 1354–1361. https://doi.org/10.1364/AO.40.001354.